Search for a High-Mass Higgs Boson with the ATLAS Detector at the LHC

Thomas Maier

Dissertation der Fakultät für Physik
der Ludwig-Maximilians-Universität München

vorgelegt von
Thomas Maier
aus Berlin

München, 7. Dezember 2016

Erstgutachter: Prof. Dr. Dorothee Schaile
Zweitgutachter: Prof. Dr. Wolfgang Dünnweber
Tag der mündlichen Prüfung: 26. Januar 2017

Zusammenfassung

Die vorliegende Arbeit präsentiert die Suche nach einem schweren Higgs Boson im Zerfallskanal $H \to W^+W^- \to \ell^+\nu\ell^-\bar{\nu}$. Dabei ist der Endzustand mit einem Elektron und einem Myon und deren assoziierten Neutrinos berücksichtigt. Diese Signatur zeichnet sich durch eine hohe experimentelle Sensitivität im Vergleich zum Zerfall nach zwei Elektronen oder zwei Myonen aus, da der hohe Untergrund durch die Produktion eines Z Bosons stark unterdrückt ist. Für die Produktion des Higgs Bosons werden die Gluon-Gluon Fusion und Vektorboson Fusion in Betracht gezogen. Die präsentierte Analyse benutzt Daten des LHC Experiments ATLAS, die mit Proton-Proton Kollisionen bei einer Schwerpunktsenergie von 13 TeV aufgenommen wurden. Dabei entspricht die Datenmenge einer integrierten Luminosität von $13,2\ \text{fb}^{-1}$. Um nach einem vom Untergrund der Standardmodell-Prozesse signifikant verschiedenen Signal zu suchen, wird die Verteilung der transversalen Masse benutzt. Diese wird aus dem Elektron-Myon Paar und dem fehlenden transversalen Impuls aufgrund der Neutrinos rekonstruiert. Die Analyse definiert drei Signalregionen, die die charakteristischen kinematischen Eigenschaften der beiden Produktionskanäle ausnutzen, um das Signal vom Standardmodell Untergrund zu trennen. Die dominanten Untergründe durch Zerfälle von Top Quarks und nicht-resonanten W Boson Paaren werden in einem Likelihood Fit durch Kontrollregionen normiert. Es werden zwei Signalinterpretationen untersucht, wobei eine Masse des schweren Higgs Bosons bis zu 3000 GeV angenommen wird. Dabei nimmt die sogenannte „Narrow Width Approximation“ eine vernachlässigbare Linienbreite des Bosons an, wohingegen die „Large Width Assumption“ verschiedene Breiten bis zu 15% der Masse des schweren Higgs Bosons betrachtet.

Im Rahmen der präsentierten Suche nach einem schweren Higgs Boson kann kein signifikanter Überschuss über dem Standardmodell Untergrund in den analysierten Daten beobachtet werden. Die Analyse setzt obere Ausschlussgrenzen auf den Produktionswirkungsquerschnitt eines ungeladenen, schweren skalaren Bosons, multipliziert mit dem Verzweigungsverhältnis zu zwei W Bosonen, mit einem Konfidenzniveau von 95%. Ein schweres Boson in der Interpretation der Narrow Width Approximation im Gluon-Gluon Fusionskanal wird mit einem Wirkungsquerschnitt bis maximal 1,37 und $0,051$ pb für eine Masse von 400 und 2800 GeV ausgeschlossen. Die Ausschlussgrenzen auf den Wirkungsquerschnitt eines schweren Bosons mit vernachlässigbarer Breite im Vektorboson Fusionskanal können bei den selben Massen auf 0,49 und $0,030$ pb gesetzt werden. Für ein schweres Boson im Gluon-Gluon Fusionskanal mit einer Linienbreite von 15% seiner Masse kann ein Wirkungsquerschnitt bis maximal 1,4 und $0,071$ pb bei einer Masse von 400 und 2800 GeV

ausgeschlossen werden.

Abstract

This thesis presents the search for a high-mass Higgs boson in the $H \to W^+W^- \to \ell^+\nu\ell^-\bar{\nu}$ decay channel. The final state with one electron and one muon and their associated neutrinos is considered. This signature is experimentally more sensitive than the one with two electrons or two muons, due to the strong suppression of background contributions from the production of a Z boson. For the production modes of the Higgs boson, the gluon-gluon fusion and vectorboson fusion channels are taken into account. Proton-proton collision data recorded by the LHC experiment ATLAS at a centre-of-mass energy of 13 TeV, corresponding to an integrated luminosity of 13.2 fb^{-1}, are analysed. The spectrum of the transverse mass, reconstructed from the electron-muon pair and missing transverse momentum from the neutrinos, is probed for a signal excess above the background from Standard Model processes. Three signal regions are defined to target the characteristic kinematic properties of the two production channels, in order to discriminate the signal from the Standard Model background. Data control regions are used to constrain the normalisation of the dominant background contributions coming from top quark processes and the non-resonant decay of W boson pairs in a likelihood fit. Two signal interpretations are studied for a heavy boson mass up to 3000 GeV. The narrow width approximation assumes a negligible line width of the hypothesised boson, while the large width assumption considers widths up to 15% of the heavy boson mass.

No significant excess above the Standard Model background is observed in the analysed data. In the absence of a signal excess, upper exclusion limits are placed at 95% confidence level on the production cross section of a charge neutral heavy scalar boson, multiplied with the branching ratio to two W bosons. For the interpretation of the narrow width approximation in the gluon-gluon fusion production mode, a cross section down to 1.37 and 0.051 pb is excluded for a mass of 400 and 2800 GeV, respectively. Upper limits on the cross section of a heavy boson with negligible width in the vectorboson fusion channel can be placed at 0.49 and 0.030 pb at the same mass points. For a heavy boson in the gluon-gluon fusion channel with a line width of 15% of its mass, a cross section down to 1.4 and 0.071 pb is excluded for a mass of 400 and 2800 GeV, respectively.

Contents

1 Preface **1**

2 Introduction **3**
2.1 The Standard Model of Particle Physics 3
2.1.1 Elementary Particles 3
2.1.2 Fundamental Interactions 4
2.2 The Higgs Mechanism 8
2.3 Particle Physics Processes 10
2.3.1 Higgs Boson Production and Decay 10
2.3.2 Background from Top Quark Processes 11
2.3.3 Background from Vectorboson Pairs 12
2.3.4 Background from Z+jets and W+jets Processes 13

3 Experimental Setup **15**
3.1 The Large Hadron Collider 15
3.2 The ATLAS Detector 16
3.2.1 Coordinate System 17
3.2.2 Inner Detector 18
3.2.3 Calorimeter System 20
3.2.4 Muon Detector 20
3.2.5 Trigger System 21
3.3 Particle Reconstruction 22
3.3.1 Tracks and Vertices 22
3.3.2 Electrons 23
3.3.3 Muons 23
3.3.4 Jets 24
3.3.5 B-tagging 24
3.3.6 Missing Transverse Energy 24
3.4 Simulated Data Generation 25

4 Search for a High-Mass Higgs Boson in the $e\mu\nu\nu$ Decay Channel **29**
4.1 Data and Monte Carlo Simulation Samples 29
4.2 Analysis Selection 34

4.2.1 Object Selection . . . 34
4.2.2 Event Selection . . . 38
4.3 Background Modelling . . . 48
4.3.1 Top Quark Background . . . 49
4.3.2 W Boson Pair Background . . . 51
4.3.3 W+jets Background . . . 53
4.4 Signal Modelling . . . 55
4.4.1 Signal Interpretations . . . 55
4.4.2 Impact of Jet Multiplicity on the ggF Signal Categorisation . . . 62
4.5 Systematic Uncertainties . . . 66
4.5.1 Experimental Uncertainties . . . 66
4.5.2 Theory Uncertainties on the Background . . . 75
4.5.3 Theory Uncertainties on the Signal . . . 78
4.5.4 Summary . . . 79
4.6 Statistical Evaluation . . . 81
4.7 Results . . . 83
4.7.1 Limits on NWA Signal Interpretation . . . 83
4.7.2 Limits on LWA Signal Interpretation . . . 85
4.7.3 Discussion . . . 87

5 Conclusions and Outlook 91

A Input for the Likelihood Fit 95

B Monte Carlo Samples 97

Chapter 1

Preface

The discovery of a new scalar boson in 2012 by the ATLAS and CMS experiments at the LHC marked the culmination of the efforts to confirm the existence of the last missing building block of the Standard Model. The properties of this new boson have been studied extensively over the last years [1–4] and found to be consistent with the predicted Standard Model Higgs boson.

Despite the very successful description of particle physics phenomena by the Standard Model, many unanswered questions necessitate additional, complementary models and theories. This includes the nature of neutrino masses, the cause of imbalance of baryonic matter and antimatter in the visible universe, and the origin of dark matter, to give a few examples. Many theories beyond the reach of the Standard Model involve the extension of the Higgs sector [5–7], leading to one or more additional bosons.

With the full ATLAS data of proton-proton collisions at a centre-of-mass energy of 8 TeV, the existence of an additional Higgs boson was probed up to a mass of 1500 GeV in the decay to two W bosons [8], extending the analysis on the Standard Model Higgs boson in this channel. A similar search was performed by the CMS experiment, exploring the mass range between 145 and 1000 GeV [9].

With the start of LHC operations at a proton-proton centre-of-mass energy of 13 TeV, an enhanced focus was put on searches for a high-mass bosonic resonance, since a large increase in production cross section with respect to the previous 8 TeV collision energy is expected from theories involving extensions of the Standard Model Higgs sector. The analysis presented in this thesis focuses on a general, model independent search for a signal signature compatible with the topology of the $H \to W^+W^- \to \ell^+\nu\ell^-\bar{\nu}$ decay, with a charge neutral heavy scalar boson produced in the gluon-gluon fusion or vectorboson fusion channel.

The thesis is structured as follows: a brief introduction to the Standard Model of particle physics is given in Chapter 2, including a description of processes considered as background and signal contributions. Chapter 3 describes the experimental setup, with an introduction of the LHC and the ATLAS detector, as well as the description of the methodology of particle reconstruction and simulated data generation. The main part of the thesis is the presentation of the analysis in Chapter 4. Section 4.1 gives a brief introduction of

the simulated data samples used in the analysis to describe the observed data recorded by ATLAS. The selection criteria of reconstructed objects and requirements employed on the properties of the decay topology, as seen in observed and simulated data, are summarised in Section 4.2. Sections 4.3 and 4.4 describe the modelling of background and signal processes. The impact of experimental and theoretical uncertainties on the analysis is discussed in Section 4.5. Section 4.6 gives a brief description of the statistical methodology used to evaluate the preliminary results presented in Section 4.7. Finally, a summary and outlook of the analysis is given in Chapter 5.

Chapter 2

Introduction

In this chapter, a brief description of the Standard Model of particle physics is given (Section 2.1), introducing the elementary particles and the fundamental interactions between them. The Higgs mechanism, which describes a way to dynamically generate masses of the weak gauge bosons, is introduced in Section 2.2. Finally, the particle physics processes relevant for the analysis in Chapter 4 are discussed in Section 2.3.

2.1 The Standard Model of Particle Physics

The current understanding of particle physics is formed by the Standard Model (SM), of which today's iteration was mainly developed since the 1970s [10, 11]. During the early 20th century, particle physics was predominantly driven by observation of new particles and phenomena, which necessitated the development of theories and models to explain and order the experimental observations. With the evolution of these models, the prediction of new particles and their eventual confirmation in experimental measurements became the common modus operandi in the science of particle physics, over the course of the last century. The successful history of predictions by the SM culminated in the discovery of the Higgs boson in 2012, by the ATLAS and CMS experiments [12, 13].

2.1.1 Elementary Particles

The SM defines a categorisation of elementary particles, which constitutes the basis to describe experimental observations in particle physics [10, 11, 15]. A general classification is done according to the spin of the particles as well as the interactions that affect them. Fermions have half-integer spin values, while bosons are particles with integer spin. The indivisible[1] fermionic constituents are grouped in three generations of leptons and strongly interacting quarks. Leptons are comprising the electron, the muon, and the tau, with an electric charge of -1, and their respective lepton neutrinos, with charge 0. In a similar way, quarks are categorised to the up and down quark, the charm and strange quark, and

[1] according to present knowledge

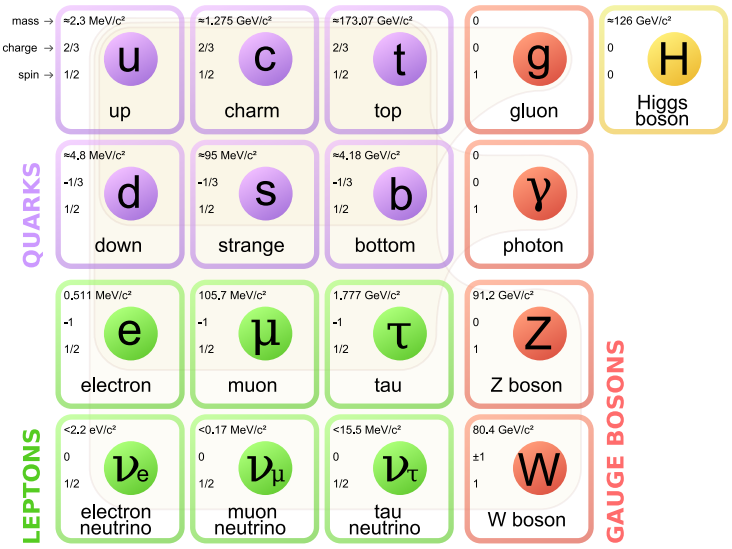

Figure 2.1: Elementary particles of the Standard Model [14].

the top and bottom quark, with a charge of $+\frac{2}{3}$ and $-\frac{1}{3}$, respectively. Each lepton and quark also has an anti-particle as its counterpart, which holds the same properties but has a reversed charge and reversed charge-like quantum numbers.
The bosonic mediator particles of the strong and electroweak interactions are referred to as gauge bosons. The description of electroweak interactions gives rise to four spin-1 vectorbosons, namely the Z boson, the W^+ and W^- boson, and the photon. Strong interactions are mediated by eight gluons. The Higgs mechanism introduces an additional scalar (spin-0) charge neutral Higgs boson. This leads to an overall number of 12 leptons, 36 quarks[2], 12 gauge bosons, and one Higgs boson. Figure 2.1 shows an overview of the elementary particles in the SM.
In addition to the indivisible, elementary particles, bound states of quarks form composite, strongly interacting hadrons. Hadrons either consist of a quark anti-quark pair (meson), or a composition of three quarks or three anti-quarks (baryon).

2.1.2 Fundamental Interactions

According to present knowledge, four fundamental forces conduct the interaction of particles and matter in nature [10]. The *electromagnetic* force acts on the electric charge of particles. The *weak* force was first introduced as explanation for the occurrence of the nuclear beta decay. The present description was formulated in the 1960s by Glashow, Weinberg, and Salam, which treats electromagnetic and weak interactions as manifestations of the same *electroweak* force. The formulation of the *strong* force first emerged as an explanation for the strong bindings of protons and neutrons in atomic nuclei. Finally, the *gravitational* force acts on the mass of matter and particles. Although the present

[2]taking into account the three configurations of colour charge

understanding of gravitational interactions is well described on large scales by Newton's classical theory of gravity and Einstein's general theory of relativity, a comprehensive and completely satisfactory description in the context of a quantum theory is still left open.

In particle physics, the common description of physical processes is done in the language of relativistic field theories using the Lagrangian formalism [10]. Instead of discrete objects in three dimensional space, particles are represented by fields, parametrised with the four space-time coordinates ($\phi_i(x, y, z, t)$ or $\phi_i(x_\mu)$ with $\mu = 1, 2, 3, 4$). The classical Lagrangian $L(x, y, z, \dot{x}, \dot{y}, \dot{z})$ is replaced with a Lagrangian density $\mathcal{L}(\phi_i, \partial_\mu \phi_i)$ and the Euler-Lagrange equation takes the form[3]

$$\partial_\mu \left(\frac{\partial \mathcal{L}}{\partial(\partial_\mu \phi_i)} \right) = \frac{\partial \mathcal{L}}{\partial \phi_i} \tag{2.1}$$

with

$$\partial_\mu \phi_i \equiv \frac{\partial \phi_i}{\partial x^\mu}. \tag{2.2}$$

As an example, the Klein-Gordon Lagrangian for a scalar (spin-0) field is[4]

$$\mathcal{L} = \frac{1}{2}(\partial_\mu \phi)(\partial^\mu \phi) - \frac{1}{2} m^2 \phi^2 \tag{2.3}$$

with the respective equation of motion (Klein-Gordon equation)

$$\partial_\mu \partial^\mu \phi + m^2 \phi = 0, \tag{2.4}$$

according to Eq. 2.1.
The transition from a classical to a quantum field theory involves the particular interpretation of the different parts of the Lagrangian [10]. The fields themselves are quantised and particles are taken as the quanta of their associated fields. Feynman rules define how the Lagrangian terms contribute to the determination of particle interaction properties, like the decay width Γ or cross section σ, in the context of a perturbative calculus. Feynman diagrams are used as a visual depiction of particle interactions, where particle lines (propagators) join to interaction vertices. Figure 2.2 shows diagrams[5]for basic processes of fermion interaction through coupling to the mediator gauge bosons of the electromagnetic (photon), weak ($W^\pm$, Z), and strong force (gluons).
For the description of particle interaction in a Lagrangian formalism, the Lagrangian can be divided in terms for the free particle fields (see Eq. 2.3 for a spin-0 field) and the interaction between them. The latter is realised by the requirement of invariance of the Lagrangian under local gauge transformation associated to the respective symmetry groups, which gives rise to the coupling terms between the fermionic and bosonic fields.

[3]Greek letter indices denote a Lorentz four-vector.

[4]The natural unit convention is used, where $\hbar = c = 1$.

[5]The time propagation axis points to the right. Fermions are indicated with arrows in direction and anti-fermions with arrows in opposite direction of the time axis.

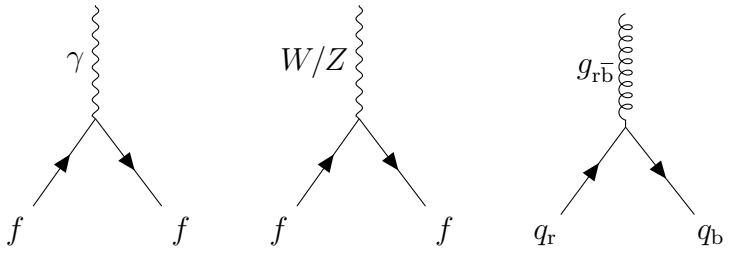

(a) EM (b) Weak (c) Strong

Figure 2.2: Feynman diagrams for the electromagnetic (a), weak (b), and strong (c) interaction of fermions, mediated by the respective gauge bosons. For the gluon (g) and the quarks (q), the colour charge is indicated.

The underlying symmetry of the SM interactions is mathematically represented by $U(n)$ and $SU(n)$ symmetry groups [10, 15], taking the form $SU(3)_C \times SU(2)_L \times U(1)_Y$.

***SU*(3)$_C$**
The gauge group $SU(3)_C$ represents the colour symmetry of strong interactions in quantum chromodynamics (QCD) [10,15]. Quarks hold one of three colour charges, "red" (r), "blue" (b), and "green" (g). Gluons act as the mediators of the strong force, coupling to quarks and carrying the difference in colour, as depicted in Figure 2.2c. Consequently, gluons have colour charge as well, one colour and one anti-colour. In the context of an $SU(3)$ symmetry, the combinations of colour anti-colour pairs constitute a colour octet, giving rise to eight gluons, and one colour singlet. In nature, coloured particles are not observed to exist outside of the bound states of hadrons, which is known as the rule of colour confinement. Furthermore, no indication of the existence of a colourless particle associated with the colour singlet is observed so far, suggesting that this state is not realised in nature. Gluons also couple to other gluons, due to them being colour charged, which confines the reach of the strong force to very small distances despite the massless nature of gluons (in contrast to the infinite range of photons).
The QCD Lagrangian for a fermionic colour triplet (denoted by the Dirac spinor ψ), coupling to the massless gluon gauge fields $\boldsymbol{G}_\mu$, is[6]

$$\mathcal{L} = i\overline{\psi}\gamma^\mu \mathcal{D}_\mu \psi - m\overline{\psi}\psi - \frac{1}{4}\boldsymbol{G}_{\mu\nu}\boldsymbol{G}^{\mu\nu}. \tag{2.5}$$

The latter term represents the dynamical component for the gluons, with the respective field-strength tensors $\boldsymbol{G}^{\mu\nu}$. The covariant derivative $\mathcal{D}_\mu$ reflects the condensed representation of the dynamical term for the fermionic fields and their interaction with the gluons, as induced by the local gauge invariance requirement. It is defined as

$$\mathcal{D}_\mu \equiv \partial_\mu + \frac{1}{2} i g_s \boldsymbol{\lambda} \cdot \boldsymbol{G}_\mu, \tag{2.6}$$

[6]The boldface notation is used for vector quantities which are not Lorentz four-vectors.

where g_s is the strong coupling constant and $\boldsymbol{\lambda}$ denotes the vector of the eight Gell-Mann matrices.

$SU(2)_L \times U(1)_Y$

Electroweak interactions are represented by the $SU(2)_L \times U(1)_Y$ gauge symmetry, which describes interactions as depicted in Figure 2.2a and 2.2b [10, 15–17]. In the context of electroweak theory, the $W^{\pm}$ and Z bosons and the photon are mixed states of three weak interaction gauge bosons $\boldsymbol{W}^{\mu}$ and one boson B^{μ}, which couples to the hypercharge Y. The hypercharge is defined as

$$Y = 2Q - 2I^3, \tag{2.7}$$

with the electric charge Q and the third component of the weak isospin I^3. The L in $SU(2)_L$ indicates that the weak interaction acts only on left-handed fermions and right-handed anti-fermions. The left- or right-handed nature of a fermion is described by the chiral states of its representation as a Dirac spinor in quantum field theory. It manifests itself by the observed helicity h of particles, defined as

$$h = \frac{\boldsymbol{s} \cdot \boldsymbol{p}}{|\boldsymbol{s}| \cdot |\boldsymbol{p}|}, \tag{2.8}$$

with the particle spin $\boldsymbol{s}$ and its momentum $\boldsymbol{p}$. The weak isospin defines three generations of flavour states of leptons and quarks, where left-handed fermions form weak isodoublets χ_L with $I_L^3 = \pm\frac{1}{2}$ and right-handed fermions weak isosinglets ψ_R with $I_R^3 = 0$:

$$\begin{aligned} \chi_L &= \begin{pmatrix} \nu_\ell \\ \ell \end{pmatrix}_L, \ \psi_R = \ell_R, \nu_{\ell,R}; \quad \text{for } \ell = e, \mu, \tau \\ \chi_L &= \begin{pmatrix} q_u \\ q_d' \end{pmatrix}_L, \ \psi_R = q_{u,R}, q_{d,R}; \quad \text{for } q_u = u, c, t;\ q_d = d, s, b \end{aligned} . \tag{2.9}$$

The prime on the quark doublet q_d component indicates that the weak eigenstates are mixtures of the mass eigenstates, where the relation is formulated by the Cabibbo-Kobayashi-Maskawa matrix:

$$\begin{pmatrix} d' \\ s' \\ b' \end{pmatrix}_{weak} = \begin{pmatrix} V_{ud} & V_{us} & V_{ub} \\ V_{cd} & V_{cs} & V_{cb} \\ V_{td} & V_{ts} & V_{tb} \end{pmatrix} \begin{pmatrix} d \\ s \\ b \end{pmatrix}_{mass} = V_{CKM} \begin{pmatrix} d \\ s \\ b \end{pmatrix}_{mass} . \tag{2.10}$$

As a consequence, weak interactions in charged currents (involving a W^+ or W^- boson) are not flavour conserving.

The Lagrangian for electroweakly interacting fermionic fields, coupling to the $\boldsymbol{W}^{\mu}$ and B^{μ} gauge fields, is

$$\mathcal{L} = i\overline{\chi}_L \gamma^{\mu} \mathcal{D}_{\mu}^{L} \chi_L + i\overline{\psi}_R \gamma^{\mu} \mathcal{D}_{\mu}^{R} \psi_R - \frac{1}{4} \boldsymbol{W}_{\mu\nu} \boldsymbol{W}^{\mu\nu} - \frac{1}{4} B_{\mu\nu} B^{\mu\nu}. \tag{2.11}$$

The trailing two terms describe the dynamical components of the electroweak gauge bosons, with the field-strength tensors $\boldsymbol{W}^{\mu\nu}$ and $B^{\mu\nu}$. The covariant derivatives for electroweak interactions of left- and right-handed fermionic fields are defined as

$$\mathcal{D}_\mu^L \equiv \partial_\mu + \frac{i}{2}\left(g\boldsymbol{\tau}\cdot\boldsymbol{W}_\mu + g'YB_\mu\right) \tag{2.12}$$

$$\mathcal{D}_\mu^R \equiv \partial_\mu + \frac{i}{2}g'YB_\mu, \tag{2.13}$$

with the vector of the three Pauli matrices $\boldsymbol{\tau}$ and the electroweak coupling constants g and g', which are fixed by the elementary charge e and the weak mixing angle θ_w:

$$e = g\ \sin\theta_w = g'\ \cos\theta_w. \tag{2.14}$$

The problem of introducing local gauge invariance to the particle interaction description in a Lagrangian formalism is that it also imposes the requirement that the emerging gauge bosons have to be massless [18]. While this is true for photons and gluons, it is contrary to the experimental observations of massive W and Z bosons. Furthermore, the mass term for fermionic fields, as shown in Eq. 2.5 ($m\overline{\psi}\psi$), is not invariant under local $SU(2)_L\times U(1)_Y$ gauge transformation, since the left- and right-handed fermion components transform differently. Even if the gauge invariance requirement is ignored, introducing mass terms for spin-1 fields by hand gives rise to unrenormalisable divergences which render the theory meaningless [15]. Gerard 't Hooft, together with his doctoral advisor Martinus Veltman, showed that Yang-Mills theories involving massive fields generated by spontaneous symmetry breaking are renormalisable [19, 20]. In the next section, the Higgs mechanism is introduced as the example of such a theory to fully account for massive gauge bosons in the context of the electroweak theory.

2.2 The Higgs Mechanism

In order to give masses to the heavy gauge bosons and elementary fermions, a theoretical model was introduced in 1964, independently by Englert and Brout [21] and by Higgs [22], analogous to the Meissner-Ochsenfeld effect in superconductivity. The Brout-Englert-Higgs (BEH) mechanism, or just Higgs mechanism, uses the concept of spontaneous symmetry breaking in combination with local gauge invariance to dynamically generate the masses of weak gauge bosons, but also allows for fermions to acquire mass [10, 16, 17].
The Higgs mechanism [16, 18, 23] introduces a new complex scalar $SU(2)_L$ doublet field ϕ:

$$\phi \equiv \begin{pmatrix}\phi^+\\ \phi^0\end{pmatrix} = \frac{1}{\sqrt{2}}\begin{pmatrix}\phi_1+i\phi_2\\ \phi_3+i\phi_4\end{pmatrix}. \tag{2.15}$$

Additional Lagrangian terms $\mathcal{L}_{\text{scalar}}$ describe the propagation of the scalar fields and their interaction with the electroweak gauge boson fields:

$$\mathcal{L}_{\text{scalar}} = (\mathcal{D}^\mu\phi)^\dagger(\mathcal{D}_\mu\phi) - V(\phi^\dagger\phi). \tag{2.16}$$

The covariant derivative $\mathcal{D}_\mu$ (see Eq. 2.12) ensures invariance under local $SU(2)_L \times U(1)_Y$ gauge transformation and introduces interaction terms of the scalar fields with the $\boldsymbol{W}^\mu$ and B^μ gauge fields. The potential $V(\phi^\dagger\phi)$ has the form

$$V(\phi^\dagger\phi) = \mu^2(\phi^\dagger\phi) + |\lambda|(\phi^\dagger\phi)^2. \tag{2.17}$$

For the case that $\mu^2 < 0$, ϕ develops a vacuum expectation value (VEV) different from 0, for which $V(\phi^\dagger\phi)$ is minimised. The VEV can be written as

$$\phi_0 = \frac{1}{\sqrt{2}}\begin{pmatrix}0\\ v\end{pmatrix}; \quad v = \sqrt{-\frac{\mu^2}{\lambda}}. \tag{2.18}$$

Within the freedom of gauge transformation, ϕ can be formulated as an expansion around the VEV with a scalar field $H(x)$:

$$\phi(x) = \frac{1}{\sqrt{2}}\begin{pmatrix}0\\ v + H(x)\end{pmatrix}. \tag{2.19}$$

Using this representation of ϕ, the Lagrangian $\mathcal{L}_{\text{scalar}}$ (Eq. 2.16) evaluates to

$$\begin{aligned}\mathcal{L}_{\text{scalar}} = \quad & \frac{1}{2}(\partial_\mu H)(\partial^\mu H) - \lambda v^2 H^2 \\ & + \frac{1}{2}\left(\frac{g^2v^2}{4}(|W_\mu^+|^2 + |W_\mu^-|^2) + \frac{g^2v^2}{4\cos^2\theta_w}|Z_\mu|^2\right) \\ & + \frac{g^2v}{4}(|W_\mu^+|^2 + |W_\mu^-|^2)H + \frac{g^2}{8}(|W_\mu^+|^2 + |W_\mu^-|^2)H^2, \\ & + \frac{g^2v}{4\cos^2\theta_w}|Z_\mu|^2 H + \frac{g^2}{8\cos^2\theta_w}|Z_\mu|^2 H^2 \\ & - \lambda v H^3 - \frac{\lambda}{4}H^4 \\ & + const\end{aligned} \tag{2.20}$$

with

$$\begin{aligned}W_\mu^\pm &= \frac{1}{\sqrt{2}}(W_\mu^1 \mp iW_\mu^2) \\ Z_\mu &= \frac{gW_\mu^3 - g'B_\mu}{\sqrt{g^2+g'^2}}\end{aligned}. \tag{2.21}$$

The first line in Eq. 2.20 describes the free propagation of the Higgs field H with mass $m_H = \sqrt{2\lambda}v$. The second line shows the mass terms for the W and Z bosons, which are generated by spontaneous symmetry breaking, induced with the reformulation of ϕ as expansion around the VEV in combination with the requirement of local gauge invariance under $SU(2)_L \times U(1)_Y$ symmetry. The masses can be identified as

$$m_W = \frac{gv}{2}; \quad m_Z = \frac{gv}{2\cos\theta_w} = \frac{m_W}{\cos\theta_w}. \tag{2.22}$$

Lines three and four represent the gauge boson couplings to the Higgs field, in the form WWH, $WWHH$, ZZH, and $ZZHH$. Finally, line five describes the cubic and quartic self-interaction terms of H.
In a similar way, the masses of fermions are generated by additional Lagrangian terms describing the coupling of the isodoublet ϕ to the left- and right-handed fermionic fields. The resulting fermion masses take the form $m_f = \frac{\lambda_f v}{\sqrt{2}}$, where λ_f denotes a free parameter in the SM for each fermion [18, 23].

Additional Higgs Bosons from Extended Theories

The SM Higgs mechanism formulates the minimal requirement of a complex scalar electroweak doublet to generate the masses of the heavy weak gauge bosons. Theories beyond the SM (BSM), that extend the SM Higgs sector, predict one or more additional bosons, which inherit similar properties as the SM Higgs boson. Examples for the simple extension of the SM Higgs mechanism are the inclusion of an additional electroweak singlet (EWS) [5] or models describing two Higgs doublets (2HDM) [6]. The Higgs mechanism extended with an EWS predicts one additional scalar boson, while 2HDM models yield two charged, one pseudoscalar, and two charge neutral scalar bosons, one of which is generally considered to be the SM Higgs boson.
For the analysis presented in Chapter 4, two model independent signal interpretations are used, which consider a charge neutral, heavy scalar boson with a mass above the SM Higgs boson mass. The narrow width approximation (NWA) interpretation assumes a negligible line width of the heavy boson. The large width assumption (LWA) interpretation considers a width of up to 15% of the mass of the hypothesised particle.

2.3 Particle Physics Processes

In the following sections, processes of SM interactions that contaminate the analysis in Chapter 4 as background are introduced. Furthermore, the production and decay of the Higgs boson is discussed, which is considered as a SM background contribution as well as a signal process, in the context of BSM theories.

2.3.1 Higgs Boson Production and Decay

The production and decay of the Higgs boson is considered as contribution to the combined SM background as well as a signal process in form of the NWA and LWA signal interpretations. The Higgs decay to two fully leptonically decaying W bosons is studied in Chapter 4, which is one of the main analysis channels involved in the SM Higgs discovery in 2012 [12]. For a proton-proton collider, the main production channels for a charge neutral Higgs boson with spin-0, as predicted by the SM, are the gluon-gluon fusion (ggF) and vectorboson fusion (VBF). The Feynman diagrams for the ggF and VBF production processes and the Higgs decay to two W bosons are shown in Figure 2.3.

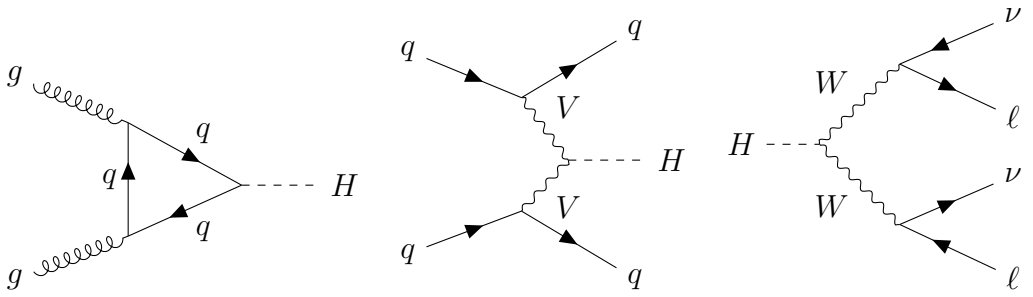

(a) ggF (b) VBF (c) $H \to WW \to \ell\nu\ell\nu$

Figure 2.3: Feynman diagrams for the ggF (a) and VBF (b) production channel and the $H \to WW \to \ell\nu\ell\nu$ decay (c).

The decay topology is defined by two oppositely charged leptons and their respective lepton neutrinos. The latter hardly interact with matter and are commonly detected as missing momentum components in collider physics. The direction of flight of the two leptons is correlated by the spin of the Higgs boson, so that their momenta predominantly point in the same direction, due to the helicity requirement enforced by the weak coupling to left-handed fermions. With increasing mass of a hypothesised high-mass Higgs boson, this correlation effect diminishes due to the increased boost of the two W bosons. Furthermore, the main identification characteristic of a high-mass Higgs boson decay comes from the momenta of the two leptons and their combined invariant mass, which tend to significantly higher values compared to the SM Higgs boson decay.
The topology of the VBF production channel is characterised by two additional quarks, which are detected as jets in particle detectors (see Section 3.3.4). The lack of a QCD colour exchange in the central part of the diagram in Figure 2.3b manifests in the direction of the jets being predominantly oriented along the proton beams in proton-proton collisions [24]. Consequently, the jets have a characteristic, large angular separation between them, which can be exploited for the discrimination from background processes. The VBF signal can also produce a signature with less than two jets, if the hadronic showers from the quarks fail requirements employed by particle jet reconstruction or fall outside of the acceptance of the detector.
The ggF production mode shows no additional hadronic activity in its topology for the lowest order diagram in Figure 2.3a. Additional jets are introduced only by higher order QCD emission of partons[7]in the production interactions. Figure 2.4 depicts examples of higher order ggF processes, which lead to one or more additional jets in the topology.

2.3.2 Background from Top Quark Processes

One of the major backgrounds for the $H \to W^+W^- \to \ell^+\nu\ell^-\bar{\nu}$ analysis is processes involving top quark decays. The dominant contribution to this background comes from

[7]Quarks and gluons, as constituents of hadrons, are also called partons.

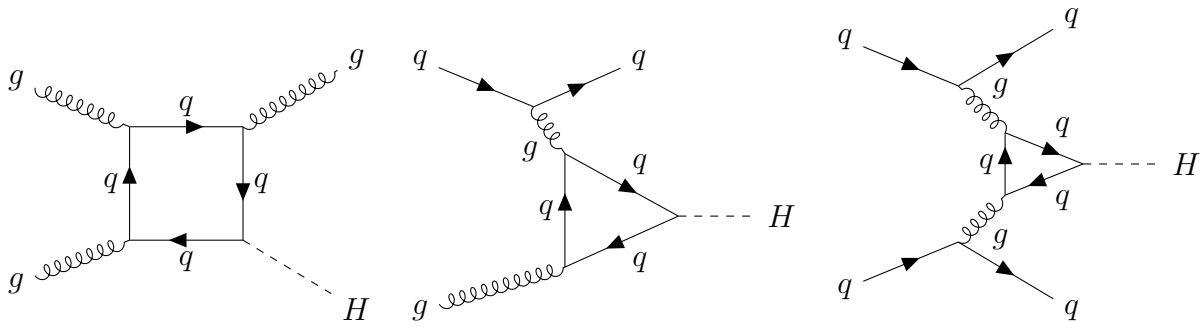

(a) $gg \to gH$ (b) $qg \to qH$ (c) $qq \to qqH$

Figure 2.4: Feynman diagrams for ggF processes with additional QCD parton emission.

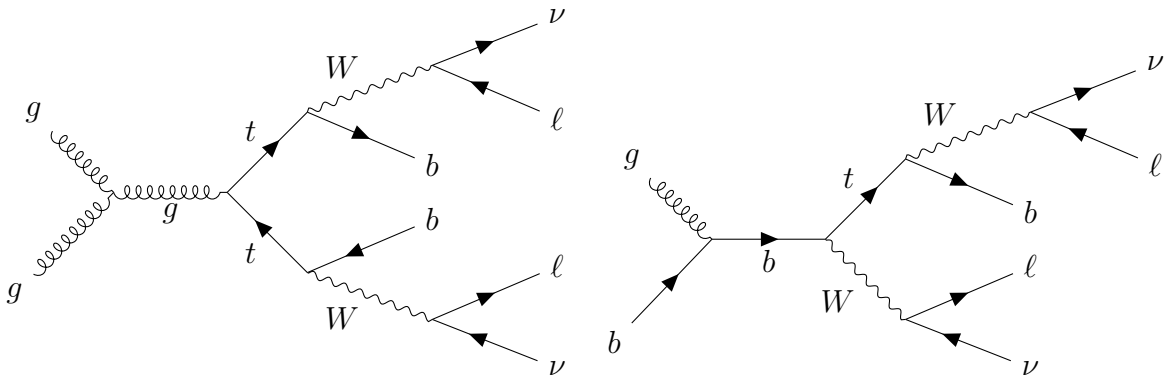

(a) $t\bar{t}$ (b) tW

Figure 2.5: Feynman diagrams for the $t\bar{t}$ (a) and tW (b) processes.

the production of a top quark pair ($t\bar{t}$), for which an example is depicted in Figure 2.5a. The presence of two b quarks provides a strong handle for the suppression of this background, utilising the distinct properties of b hadrons described in Section 3.3.5. The large cross section of this production mode and the decay of two W bosons results in the $t\bar{t}$ decay being one of the main background sources to consider, even after rejection due to b quark identification. In addition to $t\bar{t}$ decays, processes involving only one top quark provide a small but still significant contribution to the top quark background. Figure 2.5b shows an example for the production of a top quark in association with a W boson (tW), which is the most relevant single top process to consider for the signal signature. Similar to the $t\bar{t}$ decay, the tW process provides two W bosons and one b quark, but has a significantly lower cross section.

2.3.3 Background from Vectorboson Pairs

Processes involving the production of vectorboson pairs amount to a large fraction of the background composition for the signal topology. The major contribution comes from

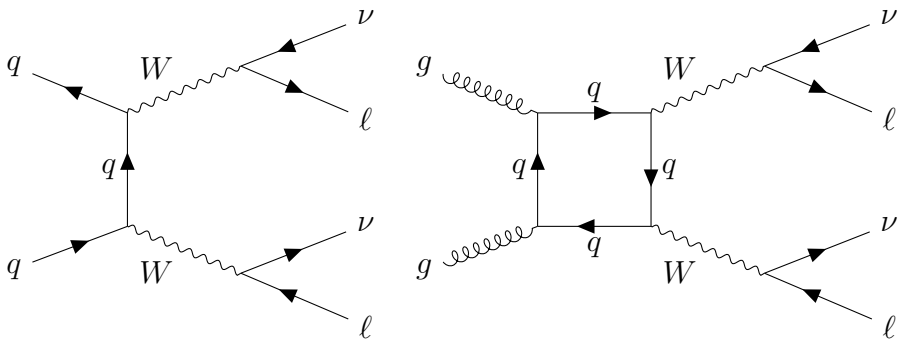

(a) $qq \to WW$ (b) $gg \to WW$

Figure 2.6: Feynman diagrams for the $qq \to WW$ (a) and $gg \to WW$ (b) processes.

processes involving two W bosons (WW), which decay into two leptons and their associated neutrinos. Figure 2.6 depicts example Feynman diagrams for the dominant production channel of WW with two initial quarks ($qq \to WW$) and the sub-dominant process induced by gluons ($gg \to WW$). The final state of leptonically decaying WW processes is identical to the signature of the $H \to W^+W^- \to \ell^+\nu\ell^-\bar{\nu}$ signal, which results in an irreducible contribution to the overall background composition.
In addition to the dominant WW production mode, decay topologies of other diboson processes allow for non-negligible background contributions. This includes WZ and ZZ decays with charged leptons as well as the production of a W or Z boson in association with a photon ($W\gamma$ and $Z\gamma$). For the $W\gamma$ processes, the case for which the photon is virtual ($W\gamma^*$) and decays further into leptons has to be considered as well.

2.3.4 Background from Z+jets and W+jets Processes

A small contribution to the background composition comes from processes containing a single, leptonically decaying W or Z boson. The decay topology of a Z boson contains an oppositely charged lepton pair, but lacks the expected missing momentum due to the neutrinos in the signal topology. Contributions from $Z \to ee$ and $Z \to \mu\mu$ processes are highly suppressed due to the requirement to only consider the signal final state with different lepton flavour. The dominant contribution of this background comes from the decay to two taus, which further decay to one electron and one muon. In addition to the lack of missing momentum, the reconstructed invariant mass of the two leptons shows a resonant behaviour below the Z boson mass. Z boson processes are taken into account without and with additional jets in the topology (Z + jets). The single W boson decay with associated jets (W + jets) yields background contributions if one jet is misidentified as a lepton. The contamination by Z + jets and W + jets processes is highly suppressed with requirements targeted at the quality and kinematic properties of the leptons, but the large production cross sections lead to non-negligible contributions to the background composition. Example Feynman diagrams are shown in Figure 2.7.

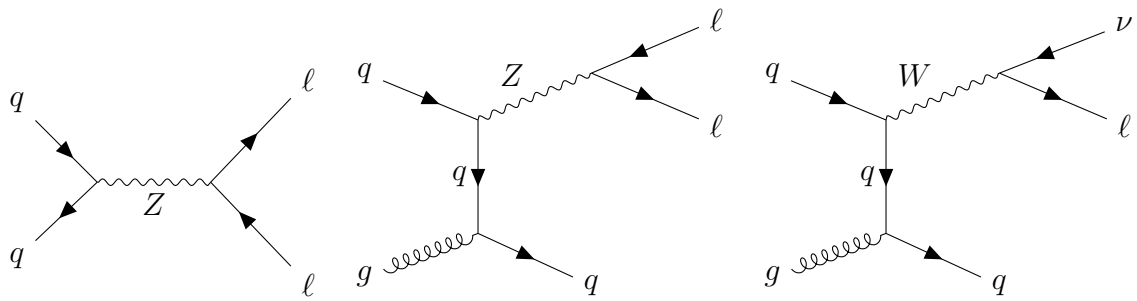

(a) $qq \to Z$ (b) $qg \to qZ$ (c) $qg \to qW$

Figure 2.7: Feynman diagrams for the single Z boson process (a) and the processes involving single Z (b) and W boson (c) decays with associated jets.

Chapter 3

Experimental Setup

In this chapter, the LHC (Section 3.1) and the ATLAS detector (Section 3.2), including its sub-detector and trigger systems, are introduced. Furthermore, the reconstruction of particles and physics quantities used by the analysis in Chapter 4 is briefly described in Section 3.3. The general methodology of the generation of simulated data used to describe data recorded by ATLAS is introduced in Section 3.4.

3.1 The Large Hadron Collider

The Large Hadron Collider (LHC) [25] is a particle accelerator at CERN, the European Organization for Nuclear Research. It consists of a ring of superconducting magnets for the deflection and focus of particles, with acceleration structures in eight straight sections around the ring to boost them on their trajectory in the 27 km tunnel of the LHC predecessor, the Large Electron-Positron Collider (LEP). The LHC is designed for the operation of proton-proton and heavy ion collisions. Hadron bunches are propagated through a chain of smaller accelerators, which boost the particles to energies at which they can be injected in the LHC acceleration ring.
Hadron beams are brought to collision at four locations around the accelerator, where the particle detectors of the four LHC experiments reside. The two main experiments, ATLAS and CMS, are present with general-purpose detectors, which target a wide range of particle physics, from SM property measurements to the search for particles predicted by BSM theories. The ALICE detector is designed to study the physics of strongly interacting matter at extreme energy densities and LHCb explores the origin of the matter-antimatter imbalance during the Big Bang by studying the properties of b hadron decays.
During the Run-I period of the LHC between 2010 and 2012, proton-proton collisions at a centre-of-mass energy $\sqrt{s} = 7$ TeV and $\sqrt{s} = 8$ TeV were recorded by the experiments. After a two year long shutdown period (LS1) from 2013 to 2015, the LHC started its Run-II operations with proton-proton collisions at $\sqrt{s} = 13$ TeV. Figure 3.1 shows a schematic overview of the LHC, including the four detector sites and the injection accelerator systems.

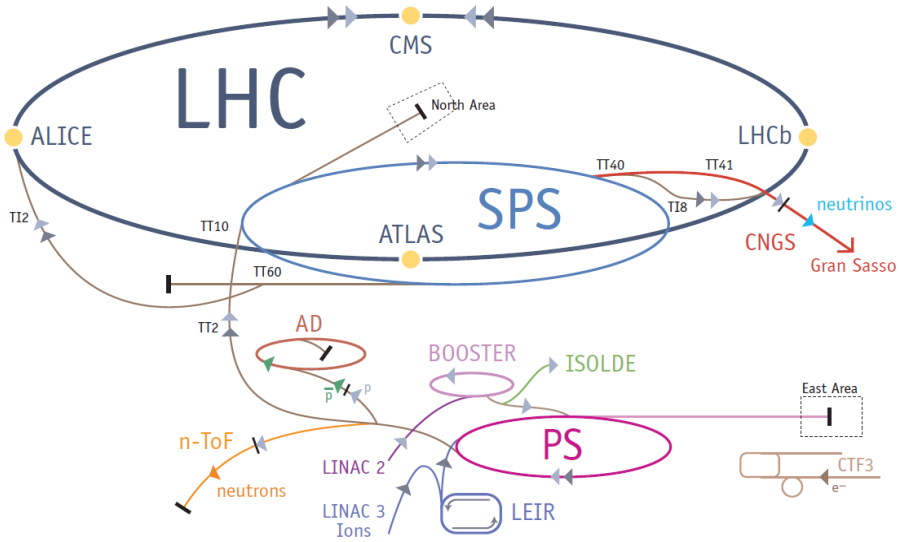

Figure 3.1: Overview of the LHC and smaller accelerator systems at CERN [26].

3.2 The ATLAS Detector

The ATLAS detector [27] is one of the four particle detectors located around the LHC accelerator ring. It is comprising four sub-detector systems, concentrically built around the proton beam axis. Two magnet systems are installed for the deflection of charged particles onto curved trajectories in the inner- and outermost detector systems. A full overview of the ATLAS detector is depicted in Figure 3.2.

The inner detector (ID) is installed around the interaction point of the proton beams and used for particle vertex reconstruction, charged particle momentum measurement, and identification of electrons. A 2 T magnetic field is generated by the solenoid magnet system surrounding the ID.

The calorimeter system forms the next layer around the solenoid magnet, consisting of two separate detectors. The electromagnetic (EM) calorimeter measures energy deposits of EM showers used for the detection of electrons and photons, spanning a pseudorapidity range $|\eta| < 3.2$. The surrounding hadronic calorimeter detects and measures energy signatures coming from hadronic particle showers. Energy measurement of EM and hadronic showers are possible up to $|\eta| = 4.9$ with liquid argon (LAr) forward calorimeters.

The outermost system of the ATLAS detector is the muon spectrometer (MS), which provides detection of muons and precise measurement of their associated momenta. A toroidal magnet system, consisting of one magnet in the barrel region of the detector and two inserted end-cap magnets, generates strong magnetic fields for the bending of the trajectories of muons traversing through the MS.

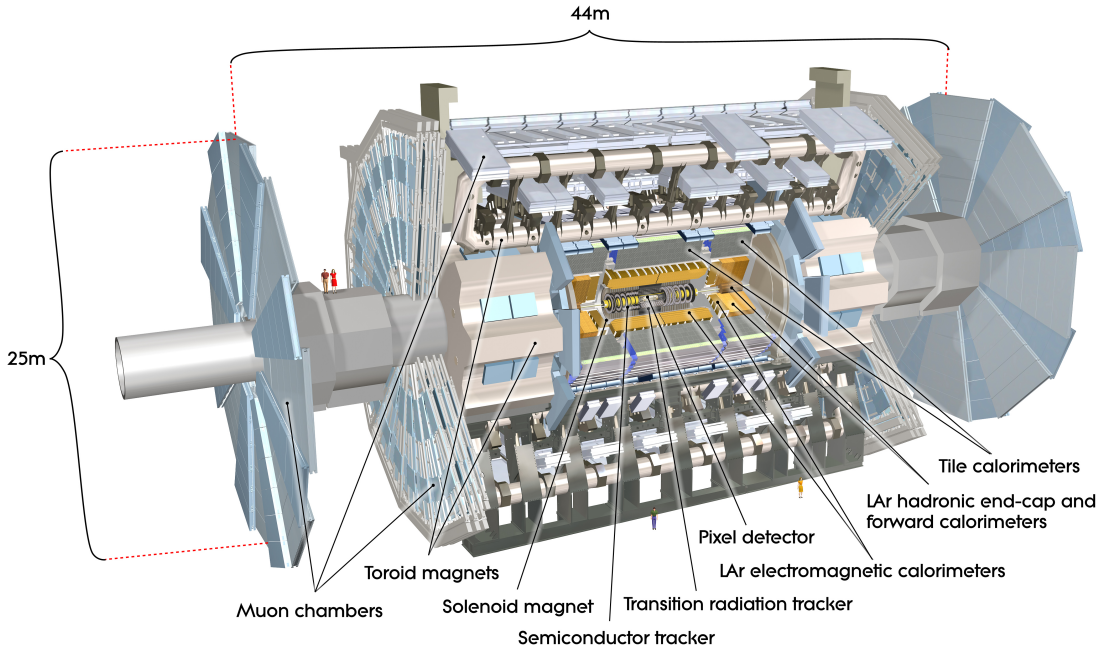

Figure 3.2: Overview of the ATLAS detector [28].

During the operational break of the LHC, extensive work went into maintenance, repair, and upgrade of the ATLAS sub-detectors as well as the data acquisition and trigger systems, increasing the overall acceptance of the detector and consolidate all components for the demands of Run-II proton-proton collisions [29].

3.2.1 Coordinate System

This section will give a brief summary of the coordinate system of the ATLAS detector and the common nomenclature used to describe particle decays originating from proton-proton collisions [27]. The right-handed coordinate system of ATLAS is oriented with the z-axis along and the x-y plane transverse to the beam line, with the origin defined as the nominal interaction point. The positive direction of the x-axis points to the centre of the LHC ring and the positive y-axis is pointing upwards. The azimuthal angle ϕ is measured around the z-axis and the polar angle θ defines the separation angle from the beam line. As a measure for the forward direction, the pseudorapidity η is defined as

$$\eta = -\ln \tan\left(\frac{\theta}{2}\right), \tag{3.1}$$

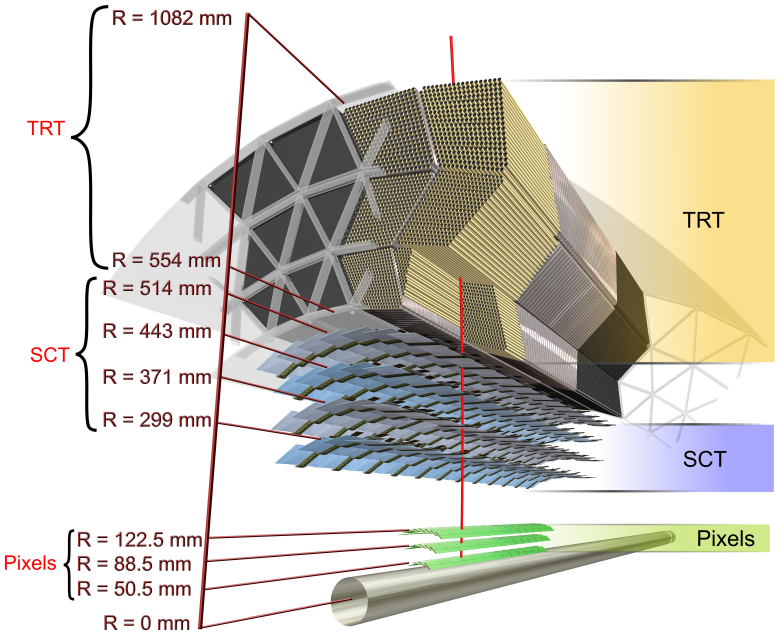

Figure 3.3: Overview of the inner detector [30]. The new innermost pixel layer (IBL) is not depicted.

whereas the rapidity y is used for massive objects:

$$y = \frac{1}{2} \ln \left[\frac{E + p_z}{E - p_z} \right]. \tag{3.2}$$

The transverse components of momentum and energy, p_{T} and E_{T}, are defined as their respective projections to the x-y plane. The distance ΔR in the η-ϕ space is defined as

$$\Delta R = \sqrt{\Delta\eta^2 + \Delta\phi^2}. \tag{3.3}$$

3.2.2 Inner Detector

The inner detector [27] consists of three independent sub-detector systems. From the beam pipe outwards, layers of silicon pixel and silicon microstrip (SCT) trackers are installed, followed by the gaseous straw tubes of the Transition Radiation Tracker (TRT), interleaved with transition radiation material. Pixel and SCT layers are arranged on concentric cylinders around the beam line in the barrel region and as disks perpendicular to the beam axis in the end-cap regions. They provide a high-resolution pattern recognition over the acceptance range of the ID ($|\eta| < 2.5$). The TRT provides measurements over the

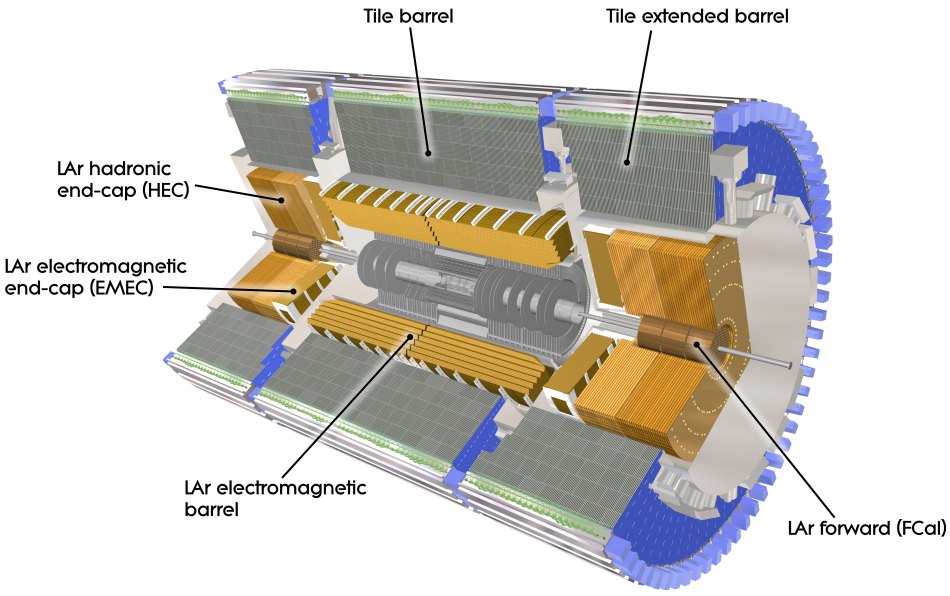

Figure 3.4: Layout of the ATLAS calorimeter system [33].

range $|\eta| < 2.0$ to enhance the pattern recognition and improve track momentum resolution, with additional electron identification capabilities complementary to the calorimeter electron detection.

In preparation of the LHC Run-II operation, an additional pixel insertable B-layer (IBL) has been installed directly on the beam pipe [29, 31]. The IBL complements the measurements of the other three pixel layers, in particular the innermost one (B-layer), to increase the track and vertex reconstruction resolution, recover tracking efficiency due to pixel module failures, and preserve tracking performance with the increase in peak luminosity for Run-II.

The intrinsic accuracy of the pixel and SCT modules in the barrel region is determined separately in the plane spanned by the radius r and ϕ (r-ϕ) and the z-direction [27]. The accuracy in the r-ϕ plane (z-direction) is 10 (115) and 17 (580) μm, for the pixel and SCT modules, respectively. In the end-cap regions, the accuracy along the z-axis translates to the precision in radial direction, due to the perpendicular orientation of the disks, whereas the modules have the same intrinsic accuracy in the r-ϕ plane. The intrinsic resolution of the newly installed IBL is 8 (r-ϕ) and 40 (z) μm [32]. The 4 mm diameter straw tubes of the TRT provide tracking information in the transverse plane only, with an intrinsic accuracy of 130 μm per straw [27].

Figure 3.3 shows a schematic overview of the ID sub-systems.

3.2.3 Calorimeter System

The ATLAS calorimeter system [27] consists of two main layers of sampling calorimeters. The inner layer is comprising a barrel and two end-cap regions, embedded in separate cryostats, which cool the active detector medium of the calorimeters. The barrel cryostat houses the EM barrel calorimeter, while the end-cap region consists of the EM end-cap calorimeter (EMEC), the hadronic end-cap calorimeter (HEC), and the forward calorimeter (FCal), which detects EM and hadronic showers. The inner layer calorimeters use LAr as active medium and lead, copper, and copper-tungsten as absorber material for the EM calorimeters, the HEC, and the FCal, respectively. In the range $|\eta| < 2.5$, devoted to precision physics, the EM calorimeter spans three active layers in depth and two layers for $2.5 < |\eta| < 3.2$. The FCal extends the EM coverage up to $|\eta| = 4.9$.
The hadronic tile calorimeter, divided into one central and two extended barrels, forms the outer layer of the calorimeter system. Scintillating tiles act as active material and steel is used as absorber medium. The tile calorimeter covers a range of $|\eta| < 1.7$, providing a full hadronic coverage over $|\eta| < 4.9$, in combination with the HEC and FCal.
The granularity of the calorimeter system is defined by the size of the separate calorimeter cells in the different calorimeter layers and regions [27]. The cell size ranges from $\Delta\eta \times \Delta\phi = 0.025 \times 0.025$ to 0.025×0.1 and 0.075×0.025 in the EM barrel calorimeter, 0.025×0.025 to 0.1×0.1 in the EMEC, 0.1×0.1 to 0.2×0.2 in the HEC, and 0.1×0.1 to 0.2×0.1 in the central and extended barrel region of the hadronic tile calorimeter. The granularity of the FCal is between $\Delta x \times \Delta y = 3.0$ cm $\times$ 2.6 cm and 5.4 cm $\times$ 4.7 cm.
The layout of the EM and hadronic calorimeters is depicted in Figure 3.4.

3.2.4 Muon Detector

The muon spectrometer [27] forms the outermost layer of the ATLAS detector, which detects muons traversing the calorimeter system with minimal absorption and measures their momenta within $|\eta| < 2.7$. In the barrel region ($|\eta| < 1.05$), precision-tracking chambers are installed between and on the coils of the barrel toroid magnet. Additional end-cap chambers are located in front and behind the end-cap toroid magnets. The muon chambers are arranged symmetrical in ϕ in eight sections, subdivided in two slightly overlapping sectors, to close gaps in the coverage of the detector. Three layers of barrel chambers are installed at increasing radii around the beam axis. The chambers in the end-cap regions are arranged in wheels perpendicular to the z-axis at different distances from the interaction point. A central service shaft for the ID, the solenoid magnet, and the calorimeters leaves a gap in coverage around $|\eta| = 0$, leading to a small angular range (up to $|\eta| < 0.8$) where high momentum tracks are not recorded in all three muon chamber layers. Additional gaps in acceptance occur due to the detector support structures on the bottom side of the ATLAS detector.
Muon Drift Tube (MDT) chambers provide muon momentum measurements over the full acceptance range of the MS ($|\eta| < 2.7$). The chambers consist of three to eight layers of drift tubes, providing an average resolution of 80 μm per tube, which combines to

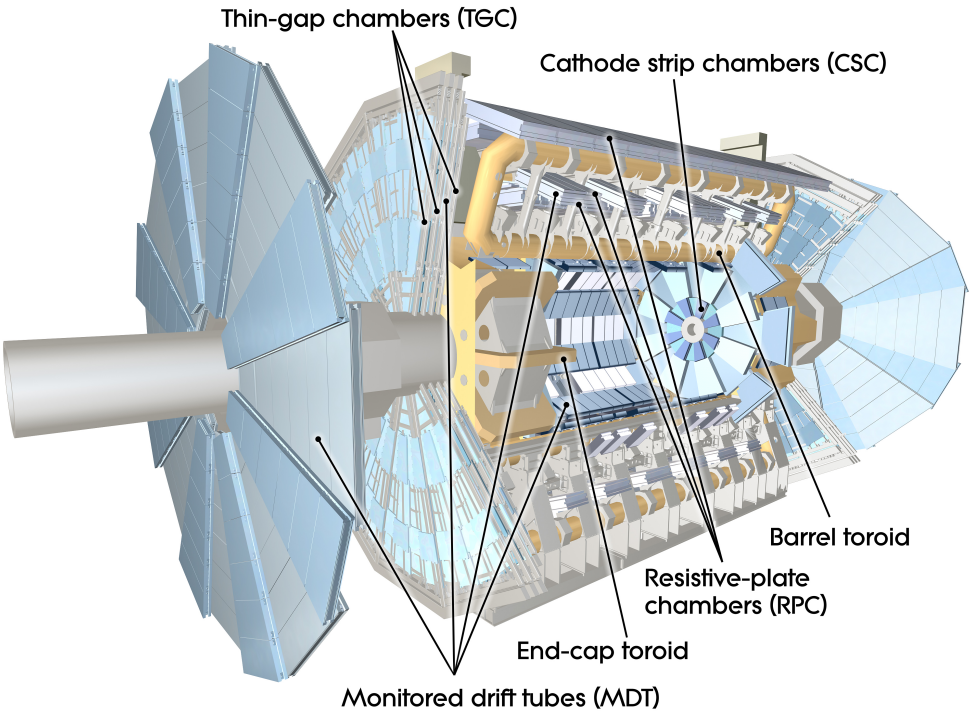

Figure 3.5: Layout of the muon spectrometer [34].

approximately 35 μm for each chamber. Cathode-Strip Chambers (CSC) are installed in the range of $2 < |\eta| < 2.7$ in the tracking layer closest to the beam axis, due to their higher rate capability and time resolution. Each CSC has a resolution of 40 μm in the bending (η) plane and 5 mm in the transverse plane.
The precision-tracking chambers are complemented by fast trigger chambers, to provide trigger capability on muon tracks in the detector. Resistive Plate Chambers (RPC) are installed in the barrel region, while Thin Gap Chambers (TGC) are used in the end-cap regions ($1.05 < |\eta| < 2.4$).
Figure 3.5 shows the layout of the MS.

3.2.5 Trigger System

Trigger systems are experimental tools to restrict a large amount of continuous data collection to a manageable rate of interesting observations. It is a common tool in physics at particle colliders, where particle decays are induced at an overwhelming rate. The ATLAS trigger system was upgraded during LS1 from a three-stage to a two-stage system, consisting of a hardware Level-1 (L1) and a software-based high-level trigger (HLT) [27, 35]. Event[1] rates are reduced from 40 MHz to 100 kHz by the L1 trigger, down to an output rate of 1 kHz of the HLT. The L1 system consists of the L1 calorimeter (L1Calo) and

[1] An event is the crossing of proton bunches with a hard scatter interaction occurring.

muon (L1Muon) trigger system, and the newly introduced L1 topological trigger modules (L1Topo). On the hardware level, the information from the calorimeter and muon systems is used to make a first-stage decision on events and find general regions of interest (RoI) in η and ϕ, which are passed to the HLT. These RoI are further processed in the second stage together with the full event information from the ATLAS detector, reducing the data rate to a manageable amount to be written to persistent storage. The L1Topo modules derive event topological quantities from L1 objects, which allows to trigger on topological decisions on the level of the hardware readout.

3.3 Particle Reconstruction

The signatures detected in the different sub-systems of the ATLAS detector are used to reconstruct the particles that emerge from the hard parton-parton interactions occurring in hadron-hadron collisions. The reconstruction methodology of the particles and physics quantities relevant for the analysis in Chapter 4 are introduced in the following sections.

3.3.1 Tracks and Vertices

The trajectories of charged particles are reconstructed as tracks in the ID, using the spatial measurements of the different sub-systems [36–38] and the solenoid magnetic field. Track seeds are identified from signal hits in the pixel detector and first layer of the SCT, which point to the close vicinity of the interaction region. In an iterative chain of fitting procedures and quality selections, the seed tracks are extended outwards throughout the layers of the SCT and the TRT, to form the fully reconstructed track. Complementary to this approach, tracks are reconstructed by extrapolation of unused track segments in the TRT inwards to the SCT and pixel detector. Similarly to the ID track reconstruction, tracks of charged particles, that escape the ID and calorimeter systems, are reconstructed in the MS [38, 39]. Hit patterns in each muon chamber are formed to segments, which are used to perform fits on layer hits to build muon track candidates.
Vertices of particle decays, compatible with originating from a hard scatter interaction, are denoted as primary vertices. They are reconstructed by iteratively running vertex finding and fitting algorithms [37,40]. This procedure selects a vertex seed candidate according to the reconstructed tracks originating from the interaction point and fits the vertex position with the position of the seed and its associated tracks. Tracks incompatible with the vertex are used as seeds for new vertices until no further tracks are present in the event.

Detector Pileup and Underlying Event

The number of reconstructed vertices is highly dependent on the number of simultaneous proton-proton interactions per bunch crossing of the LHC proton beams [37]. These follow a Poisson distribution with mean value μ. The value of μ and its average ($\langle\mu\rangle$) is used as a measure of the hard scatter activity during collisions, other than the decays coming from

the main primary vertex in a given event. The effect of multiple proton-proton interactions in the same or neighbouring bunch crossings is called detector pileup.
The activity in an event from a hard parton-parton interaction, which is not directly associated to that interaction, is represented by the "underlying event" (UE) [41]. This includes multiple parton interactions (MPI), where more than one parton-parton interaction is occurring in a single hadron-hadron collision, and particles emerging from proton beam remnants. Depending on the particular definition of UE, the contamination from gluon and photon radiation of constituents of the hard scatter process are considered for the UE as well. In general, the distinction is made between initial state radiation (ISR) and final state radiation (FSR), which specifies whether the production or decay of a process was involved in the gluon or photon emission.

3.3.2 Electrons

Electrons are reconstructed from a signature of clustered energy deposits in the EM calorimeter, associated to a charged particle track in the ID [42, 43]. Energy clusters in the calorimeter are reconstructed with the "sliding window" clustering algorithm [44], which first searches for a local maximum of deposited energy above an E_{T} threshold of 2.5 GeV with a sliding window of size 3×5 in units of calorimeter cells in the η-ϕ plane. The size of one cell corresponds to the granularity of the EM calorimeter middle layer ($\Delta\eta \times \Delta\phi = 0.025 \times 0.025$). Depending on this initial cluster of energy deposition, the EM cluster is formed by a rectangle of size 3×7 in the barrel region and 5×5 in the end-cap regions of the calorimeter. The reconstructed cluster is matched to a track, for which a minimum number of ID layer hits is required, using the distance in η-ϕ of the extrapolated track to the barycentre of the cluster.

3.3.3 Muons

Muons are reconstructed predominantly with the information from the ID and MS, complemented with the measurements from the calorimeter system [39]. The muons are categorised according to the reconstruction approach that is applied. In case that a track can be fully reconstructed in both the ID and the MS, *combined* muons are formed by globally fitting a track to ID and MS hits. With this approach, most muons are first reconstructed in the MS and then extrapolated to an ID track. The inverted case, where ID tracks are extrapolated to MS tracks, amounts to a small fraction of the reconstructed *combined* muons. If a muon leaves a signature in the MS that is insufficient for a full MS track reconstruction, it can be reconstructed as a *segment-tagged* muon, if an ID track is associated to at least one local track segment in the MS. *Extrapolated* muons are formed only based on a fully reconstructed MS track with additional requirements on the track originating from the interaction point. Finally, a *calorimeter-tagged* muon is reconstructed without information from the MS, if an ID track can be matched to an energy deposit in the calorimeter, compatible with a minimum ionising particle.

3.3.4 Jets

Hadronically interacting particles with high energy interact with the detector material, leading to distinct decay cascades of energetic jets of particles. This manifests as large energy deposits in the hadronic calorimeter. Jets are reconstructed with the anti-k_t algorithm [45] with distance parameter $R = 0.4$ and topological energy clusters (topo-clusters) [46] as input. Topo-clusters are reconstructed by collecting calorimeter cells in three dimensions around an initially selected seed cell in the calorimeter, which is required to have a significant signal-to-noise ratio [38, 47]. Cells, which are directly adjacent to the initial seed, are collected in the cluster. Furthermore, two additional layers of neighbouring cells are added, for which the required threshold on the signal-to-noise ratio is gradually reduced. In the final step, a splitting algorithm searches for local maximums and splits the cluster if more than one is found. Jets within the acceptance of the ID are associated to tracks according to the ghost association procedure [47, 48]. The tracks are assigned with an infinitesimal momentum and included in the clustering of the anti-k_t algorithm. This allows for the unique association of tracks to the respective jet, without altering its reconstructed momentum.
Jets are commonly categorised according to their flavour, which refers to the parton from which the jet originates. Jet flavour distinguishes between b quarks, c quarks, and light-flavour partons, referring to u, d, s quarks and gluons.

3.3.5 B-tagging

Hadron decays of b quarks have distinct properties, which can be exploited for discrimination from decays of hadrons containing lighter quarks [38]. The relatively high mass of b hadrons results in large transverse momenta of the decay products with respect to the jet axis, leading to large angular separation between them. In addition, the b hadron keeps a large fraction of the momentum of the original b quark. Finally, the most important feature of b quark decays is the long lifetime of b hadrons, resulting in travelling lengths of several millimetres in the detector. This leads to a distinct secondary decay vertex, which can be reconstructed separately from the hard scatter vertex. In ATLAS, algorithms based on impact parameter (IP) selection, secondary vertex (SV) finding and reconstruction of the full b hadron decay chain (JetFitter) are used to target the different properties of b quark decays [49]. The resulting output of these algorithms is combined in a multivariate b-tagging evaluation, which is used in the analysis presented in Chapter 4 to distinguish jets coming from b quark decays.

3.3.6 Missing Transverse Energy

Stable particles that hardly interact with matter traverse the layers of the ATLAS detector without leaving significant signatures, which prevents reconstruction by direct measurement. In the SM, this is the case only for neutrinos, but extended theories also predict particles which are invisible to the detector. The kinematic properties of these particles

can be quantified by exploiting momentum conservation in the transverse plane of the detector. The vector sum of transverse momenta for a given event adds up to zero, within measurement uncertainties of the detector systems. The imbalance of the visible momenta in the transverse plane is reconstructed as "missing transverse momentum" $\boldsymbol{E}_{\mathrm{T}}^{\mathrm{MISS}}$, with magnitude $E_{\mathrm{T}}^{\mathrm{MISS}}$, taken as the negative sum of transverse momenta of all reconstructed objects in the detector [50, 51].

3.4 Simulated Data Generation

Simulated events of high energy particle collisions are used to describe and model signal and background processes according to their theoretical prediction within the framework of the SM and theories beyond. For proton-proton collisions at the LHC, the calculation of perturbative QCD interactions at the highest scale of momentum transfer as well as the non-perturbative modelling of hadron formation, at the scale of parton confinement, is crucial for the accurate description of particle decays, as seen in data [41]. Monte Carlo (MC) generators are used to simulate the components for a full description of the physics processes analysed in Chapter 4.

At the core of the simulation of collision events is the generation of hard scatter interactions involving large momentum transfers [41]. The generator performs fixed order calculations of the cross section of scattering subprocesses with the parton distribution functions (PDF) of the colliding hadrons and the matrix element (ME) constructed from Feynman diagrams involved in the respective subprocess. These calculations are in particular dependent on the choice of a specific PDF set, which is evaluated from experimental data, and the choice of unphysical QCD energy scales, which is motivated from empirical considerations. The ME calculations are generally done to leading order (LO) precision, though the need for higher accuracy motivated the implementation of next-to-leading order (NLO) hard scatter simulation for several processes in general purpose generators. The inclusive cross section evaluation of some processes, for the prediction on overall production rates, involves calculations of even higher order.

Fixed order calculations of the hard scatter interactions describe the properties of outgoing particles of the processes involved well, but are not sufficient to give a proper description of higher order QCD effects [41]. In particular, the accurate description of the internal structure of jets and the distributions of accompanying particles is not possible by ME calculations alone. The probabilistic approach of parton shower (PS) simulations is used to complement the calculation of hard scatter interactions. PS algorithms typically describe higher order effects by evolution in momentum transfer from the scale of the hard interaction process to lower scales of the level of parton confinement. The combination with fixed-order ME calculations allows for an accurate description of processes generated in proton-proton collisions at the LHC, but requires a careful matching of partons coming from both approaches to prevent the double counting of contributions. Furthermore, a good understanding is required of effects coming from the UE and pileup, as well as accurate hadronisation models, which describe the transition from the partonic final state to

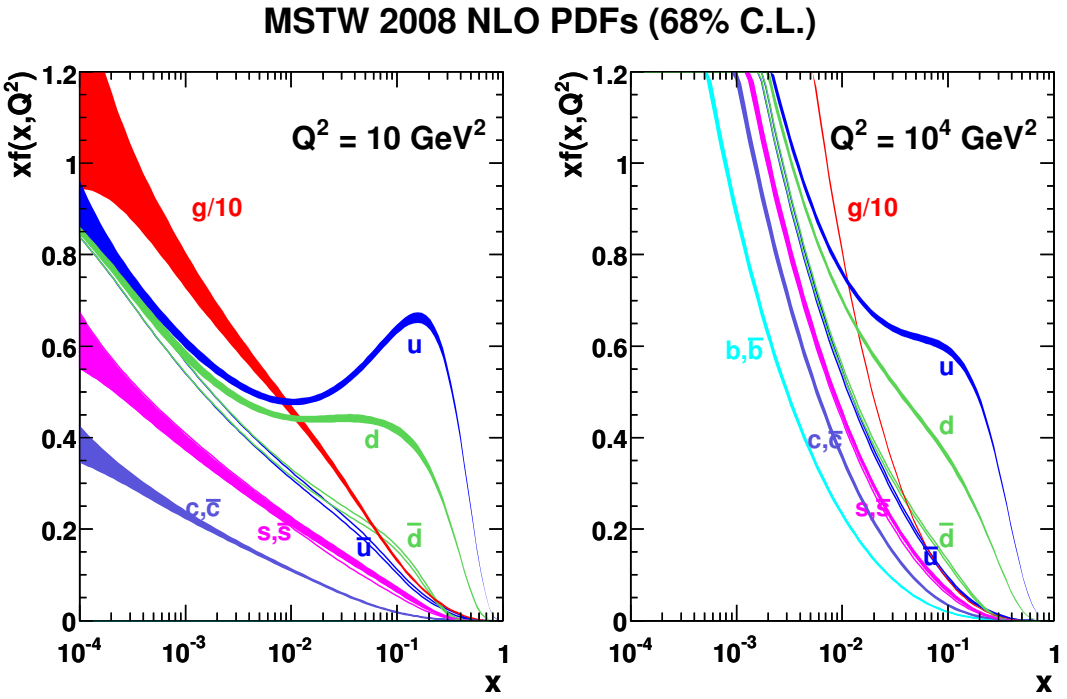

Figure 3.6: The MSTW 2008 PDF set at NLO for an energy scale of $Q^2 = 10$ GeV^2 and $Q^2 = 10^4$ GeV^2 [53].

the actual hadronic final state in event generators.

In ATLAS, a large array of general purpose MC generators is used [52] to cover the requirements of the multitude of processes relevant for proton-proton collisions at the LHC. The hard scatter generation and PS simulation are either performed by separate generators or the same one, depending on the particular requirements of the process to be modelled.

Parton Distribution Functions

Parton distribution functions are essential for the description of hard scatter processes by ME calculations as well as the simulation of parton showers and multiple parton interactions [41, 53]. At lowest order a PDF describes the probability $f_i(x, Q^2)$ of a parton type i to be measured with a momentum fraction x when a proton is probed at an energy scale Q^2. The PDF distributions are obtained from global fits to experimental data of deep inelastic scattering and other related hard scattering interaction measurements. Figure 3.6 shows the distribution for the MSTW 2008 PDF set at NLO, for an energy scale of $Q^2 = 10$ GeV^2 and $Q^2 = 10^4$ GeV^2 [53].

Simulation and Reconstruction of Particles in the ATLAS Detector

After simulation by MC generators, events have to undergo three additional steps of processing to accurately describe decays as observed in the detector. First, the interaction of particles coming from the MC event generation with all components of the ATLAS detector is simulated in GEANT4 [52, 54]. The simulated signatures are then evaluated with the ATLAS digitisation software to simulate the respective detector response [52]. Finally, the simulated detector measurements are processed with the same reconstruction software that is used for the data recorded with the ATLAS detector [55, 56].
Alternatively to a full simulation of particle interactions with the detector systems, fast simulation approaches are used to fulfil the requirement of sufficient statistical precision with limited computing resources [52]. The ATLFAST-II simulation is commonly used when a large amount of simulated data statistics is required and a small performance degradation in terms of physics description is acceptable. ATLFAST-II directly simulates the input to the reconstruction software, with the option to use full simulation for any sub-detector for an increased level of accuracy. Tracks are simulated with the reconstruction geometry, which provides a simplified description of the full detector geometry, using approximations of less sensitive detector components. Instead of a full simulation of particle interactions in the calorimeters, the particle showers are deposited directly using parameterisations of the energy profile.

Chapter 4

Search for a High-Mass Higgs Boson in the $e\mu\nu\nu$ Decay Channel

In this chapter, the search for a high-mass Higgs Boson in the $H \to W^+W^- \to \ell^+\nu\ell^-\bar{\nu}$ channel is presented. The analysed data corresponds to 13.2 fb^{-1} of integrated luminosity of proton-proton collisions at a centre-of-mass energy of $\sqrt{s} = 13$ TeV.
First, the simulated data samples used for the estimation of signal and background contributions and the data recorded by ATLAS are introduced in Section 4.1. Section 4.2 describes the requirements and corrections employed to the reconstructed objects relevant for the presented analysis, as well as the full selection criteria on events selected in MC simulation and data. The estimation and modelling of the background processes described in Section 2.3.2, 2.3.3, and 2.3.4 is outlined in Section 4.3, followed by the introduction of the considered signal interpretations in Section 4.4. Experimental and theoretical uncertainties on the analysis results are discussed in Section 4.5. The methods used for the statistical evaluation of the observed and simulated data events selected by the analysis is described in Section 4.6. Finally, the preliminary results of the analysis are presented in Section 4.7.

4.1 Data and Monte Carlo Simulation Samples

Signal and background predictions are modelled with a multitude of MC generators [41], which are chosen to suit the requirements for the respective physics processes. The generators Powheg-Box, MadGraph5_aMC@NLO, and Sherpa are used for the generation of the hard scatter interaction. Powheg-Box performs NLO ME calculations and matches them to the PS simulation of MC shower generators according to the Powheg method [57]. MadGraph5_aMC@NLO [58] merges the features of the MadGraph5 generator and the aMC@NLO tool. MadGraph5 [59] allows for the event generation of any model that can be written in the form of a Lagrangian, while aMC@NLO [60] facilitates the merging of NLO ME calculations with the PS simulation. Sherpa [61] is a general-purpose event generator that allows for ME calculations of multi-parton processes up to NLO. Further-

Process	Generator
NWA ggF	Powheg+Pythia8
NWA VBF	Powheg+Pythia8
LWA ggF	MadGraph5_aMC@NLO+Pythia8
$t\bar{t}/tW$	Powheg+Pythia
$qq \to WW/gg \to WW$	Sherpa v2.1
$WZ/ZZ/Z\gamma/W\gamma/W\gamma^*$	Sherpa v2.1
SM VBF Higgs	Powheg+Pythia8
$Z+$jets	MadGraph5_aMC@NLO+Pythia8

Table 4.1: Summary of the MC generators used for the different processes considered in the analysis.

more, Sherpa performs the simulation of the PS, UE, and hadronisation and the merging of NLO ME calculations with the PS. The Pythia generator [62, 63] is another tool for simulating a large range of processes in collider physics and is used as an interface to the hard scatter generators, except Sherpa, to perform the modelling of the PS, UE, and hadronisation. The version 8 of Pythia is a rewrite in C++ of the previous versions that were based on Fortran. While most features are propagated to version 8, older versions with well developed tuning are still used for some processes. For the systematic uncertainty evaluation in Section 4.5.2, Herwig++ [64] is also used as an alternative generator for the simulation of the PS.

In the following, the generators that are used for the various background processes and the NWA and LWA signal processes are specified, which is summarised in Table 4.1. Furthermore, the experimental data analysed in this thesis is introduced and the normalisation of simulated events according to the integrated luminosity of the data and with the technique of data control regions is demonstrated.

Signal Processes

The NWA signal samples are generated with Powheg-Box 2.0 with the CT10 PDF set [65]. Signal samples for the LWA interpretation are produced with MadGraph5_aMC@NLO using the NNPDF23LO PDF set [66]. The PS simulation for the NWA and LWA simulated events is performed by the Pythia generator with version number 8.186. For the NWA signal, dedicated samples for masses between 300 and 3000 GeV have been generated in increments of 100 GeV up to 1000 GeV and 200 GeV up to 3000 GeV. The samples for the LWA interpretation are generated in increments of 200 GeV, in the mass range between 400 and 3000 GeV.

Top Quark Processes

Events from single top and $t\bar{t}$ decays [67] are simulated with POWHEG-BOX 2.0 using the CT10 PDF set. The simulation of the PS, hadronisation, and UE is performed by PYTHIA v6.428, where the PERUGIA2012 tune [68] and CTEQ6L1 PDF set [69] is used. The properties of bottom and charm hadron decays are modelled with EVTGEN 1.2.0 [70] and the assumed top quark mass is set to 172.5 GeV.

Vectorboson Pair and Higgs Boson Processes

SHERPA v2.1.1 is used for the hard scatter generation and PS simulation of diboson processes [71], using the CT10 PDF set. MC datasets for each leptonic final state, inclusive in the intermediate diboson processes, are used to estimate contributions coming from fully-leptonic decays from vectorboson pair production. Semi-leptonic and hadronic final states of the WW, WZ, and ZZ production modes as well as $Z\gamma$, $W\gamma$, and $W\gamma^*$ decays are described by dedicated MC samples. Samples for the $V\gamma$ processes are produced separately according to the lepton flavour of the decay products and the p_{T} of the W or Z boson.
For the $qq \to WW$ process with fully leptonic decay, matrix elements are generated with up to three additional partons or up to one additional parton in the final state, at LO and NLO precision, respectively. The loop induced $gg \to WW$ process, where the W bosons decay into leptons, is simulated with matrix elements including up to one additional parton in the final state to LO accuracy. Contributions from the SM Higgs boson ggF production mode and interference effects with the WW background are included. The VBF produced SM Higgs boson is considered with a dedicated MC sample, produced with the same generator setup as for the NWA signal samples.

Z+jets Processes

$Z+$jets events [72] are generated with MADGRAPH5_AMC@NLO using the NNPDF23LO PDF set. PYTHIA v8.186 is used for the modelling of the PS, UE, and hadronisation. Matrix elements are generated for up to four jets at LO precision. MC samples for $Z \to ee$ and $Z \to \tau\tau$ decays are split according to the number of additional partons, while datasets for $Z \to \mu\mu$ decays are sliced according to the combined magnitude of transverse energies in the event and the flavour of additional partons.

Data Recorded by ATLAS

The experimental data used in the analysis is recorded by the ATLAS detector in 2015 and the first half of 2016, with proton-proton beam collisions of the LHC with a bunch spacing of 25 ns at $\sqrt{s} = 13$ TeV [73]. Data was recorded with a steadily increasing instantaneous luminosity, peaking at $5 \cdot 10^{33} \frac{1}{cm^2\, s}$ in 2015 up to $\sim 1 \cdot 10^{34} \frac{1}{cm^2\, s}$ for the 2016 data. Consequently, the mean number of interactions per bunch crossing ($\overline{N}_{\mathrm{INT.}}$) significantly changes between the two periods of data taking, which is depicted in Figure 4.1. The data suited

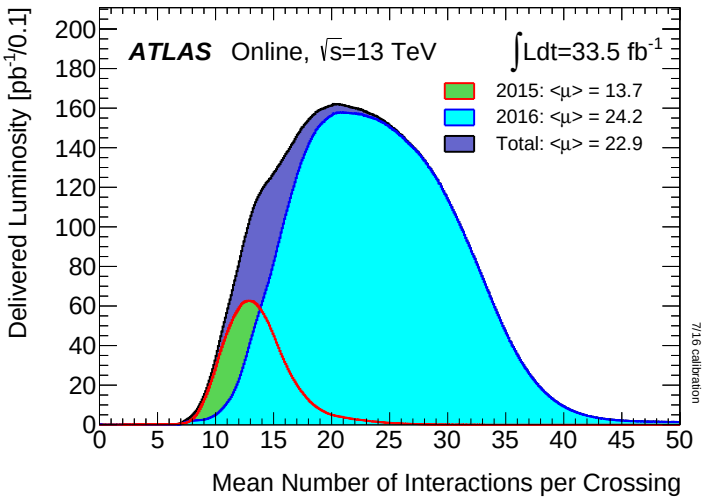

Figure 4.1: The luminosity weighted distribution of the mean number of interactions per bunch crossing for the combined 2015 and 2016 data [73]. The contribution of 2016 data reflects the recorded amount up to the 16th of September, which exceeds the data considered for the analysis.

for physics analysis amounts to 3.2 fb^{-1} for 2015 and 10 fb^{-1} for the recording period considered for 2016, which sums up to a combined integrated luminosity of 13.2 fb^{-1}.

Normalisation of Simulated Events

Selected events from MC simulation are normalised to the integrated luminosity $\left(\int \text{L dt}\right)_{\text{DATA}}$ of the recorded data considered for analysis. The normalisation is described by a scaling factor f_{LUMI}, defined as

$$f_{\text{LUMI}} = k \cdot \epsilon_{\text{FILTER}} \cdot \frac{\left(\int \text{L dt}\right)_{\text{DATA}} \cdot \sigma_{\text{MC}}}{N_{\text{MC}}}, \tag{4.1}$$

with the k-factor k, the filter efficiency ϵ_{FILTER} of the generator, the cross section σ_{MC} of the process, and the full sum of events N_{MC} of the MC sample. The k-factor accounts for higher order corrections on the process cross section or other correction factors evaluated after event simulation. Filters on generator level are used to enhance the statistics of MC datasets, by selecting specific decay topologies at the level of event simulation, which reduces the amount of resources spent on the computing intensive subsequent detector simulation and particle reconstruction. Events from such a filtered sample are scaled by ϵ_{FILTER} to properly reflect the selection rate of the respective process. The calculation of N_{MC} is done at a stage of the analysis where no selection is applied yet and includes the generator specific per event MC weight. Tables B.1, B.2, and B.3 list the cross sections, k-factors, and filter efficiencies for all nominal MC samples used in the analysis.

Data Control Regions

The normalisation of background contributions according to the cross section relies on the precise theoretical prediction of the contributing processes. Control regions (CR) allow for an estimation of the background normalisation with data from regions enriched with events coming from one specific background process. This allows for a data-driven normalisation, which is independent from the theoretical prediction of the background cross section and specific for the kinematical requirements employed by the analysis. The selection of a CR is chosen to be as close as possible to the one targeted at the signal topology, while the inversion of requirements on one or more selection quantities is used to ensure that the data sample from the CR is separate from the one used for the signal analysis, denoted as signal region (SR).

4.2 Analysis Selection

This section introduces the requirements on the objects used in the analysis as well as the full event selection targeted at a high-mass Higgs boson in the $H \to W^+W^- \to \ell^+\nu\ell^-\bar{\nu}$ channel. The selection criteria are optimised for the search of a heavy scalar boson with a decay topology of two charged leptons[1] and two neutrinos and a mass between 300 and 3000 GeV.

4.2.1 Object Selection

Physical objects are reconstructed according to the signatures they leave in the various components of the ATLAS detector, as described in Section 3.3. For this analysis, the relevant objects are muons, electrons, jets, and neutrinos in form of $E_{\mathrm{T}}^{\mathrm{MISS}}$. In the following, the requirements employed on these objects to be considered for further analysis are described in detail. Leptons and jets fully satisfying these requirements are denoted as *signal* objects.
The common recommendations within ATLAS, regarding quality and selection criteria, energy and momentum corrections, and data to MC efficiency corrections, are followed closely to ensure the highest selection efficiency with optimal background suppression.

Primary Vertex

The full reconstruction of all objects used in the analysis requires the identification of the hard scatter interaction they originate from, in the form of a primary vertex. Events are required to have at least one primary vertex, which is associated to two or more reconstructed tracks in the ID [74]. Tracks, which are considered for the vertex reconstruction, must have a p_{T} of at least 400 MeV and $|\eta| < 2.5$, while also satisfying criteria on the number of hits in the different ID layers. In the case that multiple primary vertices are reconstructed, the one with the highest $\sum p_{\mathrm{T}}^2$ of the associated tracks is chosen for the subsequent reconstruction of physics objects in the event.

Electrons and Muons

Combined muons (see Section 3.3.3) are considered as *signal* lepton candidates. Their momentum in simulation is calibrated to correct for discrepancies between data and MC simulation [39]. Calibration constants related to the momentum scale and resolution in the ID and MS are obtained from data using a binned maximum-likelihood fit with templates derived from simulation, comparing dimuon invariant mass distributions in $Z \to \mu\mu$ and $J/\Psi \to \mu\mu$ events from data and MC simulation. The corrected muon p_{T} is evaluated by combination of the weighted average of the corrected momenta from the ID and MS and used to derive momentum corrections, dependent on p_{T} and η of the muon.

[1] In the context of the analysis selection definition, only electrons and muons are referred to as leptons.

Quality requirements are employed to target muons from hard scatter interactions [39]. This includes criteria on the number of hits in the MS detector layers, compatibility between the MS and ID regarding the charge to momentum ratio as well as the momentum measurement, and agreement of the combined track fit. According to these requirements, muon candidates are defined as *Loose*, *Medium*, and *Tight* [39], with increasing stringency on the criteria. Selection efficiencies of the *Loose*, *Medium*, and *Tight* criteria are 97% (98%), 95% (96%), and 90% (92%) for muons with $p_{\mathrm{T}} < 20$ GeV ($20 < p_{\mathrm{T}} < 100$ GeV), evaluated from simulated $t\bar{t}$ events [39].
For this analysis, all muons have to satisfy the *Medium* selection, which provides a good selection efficiency and a large rejection rate of muons originating from hadron decays [39]. In order to increase suppression of backgrounds from jet misidentification, the *Tight* requirements are applied as well for muons with p_{T} smaller than 25 GeV. Muons are required to be within the acceptance of the ID ($|\eta| < 2.5$) and fulfil $p_{\mathrm{T}} > 15$ GeV.

Electrons are reconstructed as described in Section 3.3.2. Their associated calorimeter cluster energy is calibrated using MC simulation based multivariate analysis (MVA) techniques [43]. In order to equalise the response of the longitudinal layers of the EM calorimeter between data and MC simulation, uniformity corrections are applied to data [43]. Residual disagreements between data and MC are corrected with in-situ energy scale measurements in $Z \to ee$ events [43]. The fully reconstructed four-momenta of the electrons are formed with the energy of the calibrated clusters, while the angular information is taken from the ID track which best matches the selected cluster [42].
Signal electron candidates have to pass additional identification criteria to further discriminate between electrons coming from signal and background processes [42, 75]. A likelihood-based method utilising MVA techniques is used, which simultaneously evaluates input quantities related to the shape of EM showers in the calorimeter, tracking, and the track-to-cluster matching. The method defines multiple selections, namely *LooseLH*, *MediumLH*, and *TightLH* [42, 75], with increasing requirements on the likelihood-based identification criteria, such that the selection efficiency of an electron with $E_{\mathrm{T}} \approx 40$ GeV is 95%, 90% and 80%, respectively [75].
For this analysis, all electrons have to satisfy the criteria of the *MediumLH* selection, which provides a good selection efficiency while largely rejecting electrons that come from jet decays, jet misidentification or photon conversion to an electron-positron pair [42]. Electron candidates with a p_{T} smaller than 25 GeV also must fulfil the *TightLH* requirements to further suppress backgrounds from jet misidentification. Electrons are selected to have $p_{\mathrm{T}} > 15$ GeV and be within the coverage of the central EM calorimeter systems ($|\eta| < 2.47$), excluding the transition area between the barrel and the endcap regions ($1.37 < |\eta| < 1.52$).

Electrons and muons are further required to have their associated tracks be compatible with the primary vertex in the event, to ensure the relation to a hard scattering process and to reduce contributions from background processes, such as photon conversions or secondary vertex decays. Conditions are applied to the longitudinal (z_0) and transverse (d_0) impact parameters, which reflect the closest separation of the track to the primary vertex in the

respective direction. Muons and electrons are required to fulfil $|z_0 \sin\theta| < 0.5$ mm [74]. In addition, muons have to satisfy $|d_0|/\sigma_{d_0} < 3$ and electrons $|d_0|/\sigma_{d_0} < 5$, where σ_{d_0} represents the estimated uncertainty on d_0 [74].

Background contamination due to leptons that originate from hadron decays is further suppressed by constraints on the detector activity in close proximity to the reconstructed muons and electrons (lepton isolation). Leptons are required to be isolated from other particles, which is achieved by satisfying requirements on dedicated isolation variables [39]. These are based on track momenta and calorimeter energy deposits in defined distances of ΔR around the lepton, excluding the contribution from the lepton itself and correcting for effects from pileup and the UE. Muons and electrons have to satisfy the criteria defined by the *Gradient* isolation selection [39], which employs gradually increasing requirements, depending on the p_{T} of the lepton. The resulting selection efficiency is required to be larger than 90% at 25 GeV, with a gradual increase to an efficiency larger than 99% at 60 GeV [39]. Furthermore, the *GradientLoose* isolation selection [39] employs less stringent criteria to increase the efficiency to be at least 95% at 25 GeV and is used to veto additional leptons, as described in Section 4.2.2. Some of the HLT triggers used in the analysis (see Section 4.2.2) employ requirements with fixed selections on the isolation variables.

For the lepton reconstruction, identification and isolation selection, selection efficiencies as a function of p_{T} and η are evaluated in $Z \to \ell\ell$ and $J/\Psi \to \ell\ell$ events, using tag-and-probe techniques [39, 42]. Efficiency corrections, determined by comparison of the selection performance between data and MC simulation, are applied to simulated events as additional event weights.

Jets

Jets are reconstructed as described in Section 3.3.4, using topological energy clusters calibrated to the EM energy scale [46]. The jets are corrected to point to the identified primary vertex and to account for pileup effects [47]. Furthermore, a p_{T} and η dependent calibration, derived from simulated MC events, is applied, which takes into account biases coming from different calorimeter technologies in different η regions of the detector [47]. Further corrections are applied to reduce the dependence of the jet energy measurement on the directional structure of the jets, as well as corrections for jets, which are not fully contained in the calorimeter [47].

In order to mitigate contamination of jets originating from pileup, a selection is applied on the output of the jet-vertex-tagger (JVT) algorithm [76]. The algorithm performs a two dimensional likelihood evaluation with variables targeting the association of non-pileup jet tracks to the primary vertex, based on calorimeter and ID information. For jets with a p_{T} smaller than 60 GeV and $|\eta| < 2.4$, the resulting JVT output variable is required to be larger than 0.59 [77]. Jet p_{T} dependent efficiency corrections on the JVT selection are applied to events to correct for discrepancies between data and MC simulation [76]. The

corrections are evaluated with a tag-and-probe method in Z + jets events, measuring the number of jets passing the JVT requirement, where the contamination from pileup jets is subtracted.
For further suppression of jets originating from background sources, such as showers from cosmic rays, calorimeter noise, or beam induced secondary cascades, additional criteria have to be fulfilled by *signal* jet candidates [78]. Jets are probed to satisfy requirements on the signal pulse shape in the LAr calorimeters, jet energy ratio variables, and properties of the tracks associated to the jets. For this analysis, jets have to pass the *Loose* selection requirements, which provide a selection efficiency of at least 99.5% for $p_{\mathrm{T}} > 20$ GeV and 99.9% for $p_{\mathrm{T}} > 100$ GeV [78]. If an event is found with a jet passing the JVT requirement but failing the *Loose* jet selection, the event is omitted. In the following, this is referred to as "bad jet veto".
Jets considered in this analysis are required to have a p_{T} of at least 30 GeV and fulfil $|\eta| < 4.5$. The wide η range selection is required to be sensitive to the VBF topology, which has two jets in the forward direction of the detector.

Jets from b quark hadron decays are identified by applying a selection on the output of the MV2c10 b-tagging algorithm, such that the selection efficiency is 85%, as determined in simulated $t\bar{t}$ events [49]. The jets selected by this procedure are denoted as b-jets. The rejection rate of light-flavour jets is 33, and 3.1 for jets containing c quark hadrons [49]. The p_{T} requirement for b-jets is lowered to $p_{\mathrm{T}} > 20$ GeV, to enhance the suppression of backgrounds containing b quark decays. The b-tagging identification is applied only on jets within $|\eta| < 2.5$, since the measurements from the ID are required for the evaluation of the tagging algorithms (see Section 3.3.5).
Simulated events selected by b-jet identification, either by requiring or omitting jets from b quark decays, are calibrated according to the jet flavour with efficiency and inefficiency measurements on the b-tagging in data and MC simulation [79]. The b-tagging efficiency for b-jets is determined in $t\bar{t}$ events, using a combinatorial likelihood method [80]. For the b-tagging efficiency of c-jets, the number of reconstructed D^{*+} decays within jets is compared before and after the tagging requirements [81]. Finally, the mistag efficiency of light-flavour jets is evaluated in a dijet sample with the negative tag method [81], which inverts the sign of input parameters to the IP and SV tagging algorithms (see Section 3.3.5).

Overlap Removal

With the high activity in the detector during proton-proton collisions, the reconstruction of two different particles can occur from the signature left by one particle decay. Furthermore, two nearby reconstructed objects are likely to originate from the same decay chain in the detector. For example, an electron close to a jet may originate from the decay cascade of the jet, or part of the signature related to the jet decay is misidentified as the electron. In order to reduce the impact of selecting objects that do not originate directly from the hard scatter interaction, an additional overlap removal procedure is employed [82, 83]. In the case that *signal* candidates for muons, electrons, or jets are in close proximity to other

fully selected objects, they are removed according to the following overlap rules in the order given:

Electrons Share ID track with another electron and have lower p_{T}

Electrons Share ID track with a muon

Jets Within $\Delta R < 0.2$ to an electron

Electrons Within $\Delta R < 0.4$ to a jet

Jets Within $\Delta R < 0.2$ or ghost-matched (see Section 3.3.4) to a muon and $(N^{\mathrm{JET}}_{\mathrm{TRACK}} < 3)$ or $\left(\frac{p_{\mathrm{T},\mu}}{p_{\mathrm{T,J}}} > 0.5 \text{ and } \frac{p_{\mathrm{T},\mu}}{\sum p^{\mathrm{JET}}_{\mathrm{T,TRACK}}} > 0.7\right)$

Muons Within $\Delta R < 0.4$ to a jet

$N^{\mathrm{JET}}_{\mathrm{TRACK}}$ is the number and $\sum p^{\mathrm{JET}}_{\mathrm{T,TRACK}}$ the sum of transverse momenta of tracks associated to a jet.

Missing Transverse Energy

As described in Section 3.3.6, the $\boldsymbol{E}^{\mathrm{MISS}}_{\mathrm{T}}$ is reconstructed as the negative vector sum of all reconstructed objects in the event [50,51]. For the calculation of $\boldsymbol{E}^{\mathrm{MISS}}_{\mathrm{T}}$, muons and electrons are calibrated and must pass loosened selection requirements compared to the *signal* object definition, whereas no selection criteria are employed on the jets, which are calibrated as described before. Transverse momentum measurements in the detector, which cannot be associated to a fully reconstructed object, are used to form "soft term" contributions. These are either reconstructed from energy deposits in the calorimeter, or as track-based soft terms (TST) from ID track measurements. The $E^{\mathrm{MISS}}_{\mathrm{T}}$ definition in this analysis takes TST contributions into account, which provide a better performance under the pileup conditions of Run-II [51].

4.2.2 Event Selection

Reconstructed *signal* muons, electrons, and jets, according to the definitions in Section 4.2.1, are used to determine the selection on each event, targeted at the topology of a scalar high-mass boson in the $e\mu\nu\nu$ decay channel. Figure 4.2 shows the relative contributions of the background processes considered in the analysis, at each step of the full analysis selection described in this section.

Pre-selection

Events have to fulfil several criteria associated to the WW decay topology to be considered for this analysis, which will be referred to as "pre-selection". The requirements are employed for data and MC simulated events unless specified otherwise. Data events not suited

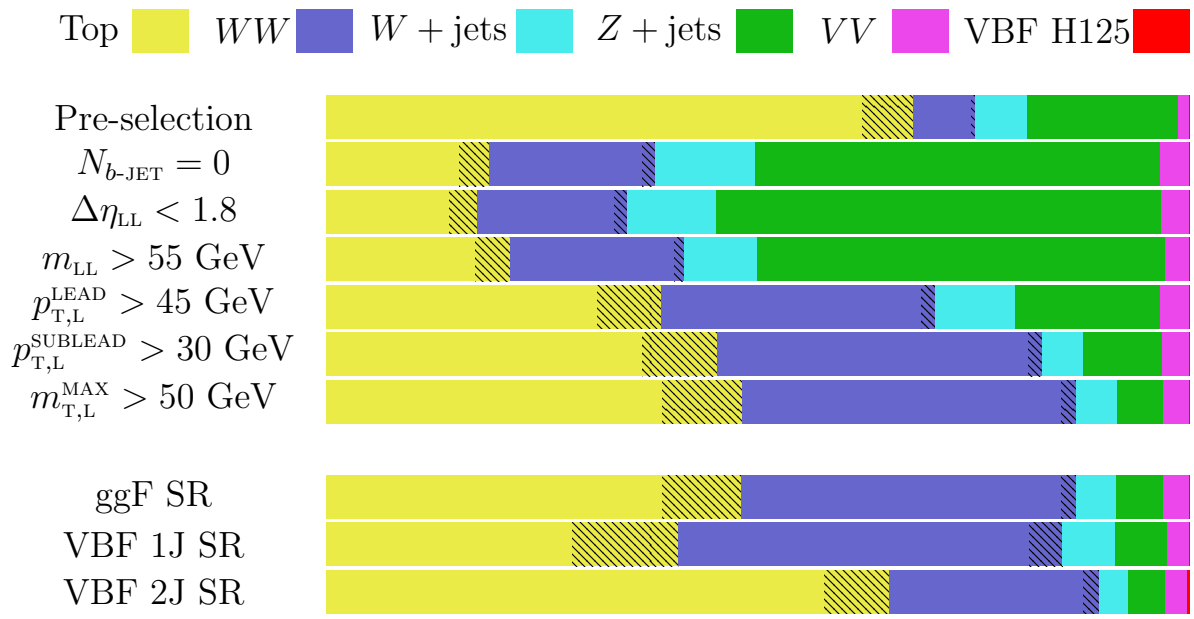

Figure 4.2: The relative background contributions at each step of the signal selection and in each signal category. The hatched areas indicate the relative contribution of the tW and $gg \to WW$ process to the top quark and WW background, respectively.

for physics analysis, due to faulty behaviour of a detector sub-system or turned off detector systems, are omitted. Furthermore, at least one primary vertex, which satisfies the criteria in Section 4.2.1, is required to be present in the event, to allow for a full reconstruction of all constituents of the decays coming from the hard scatter interaction. Finally, events have to pass the bad jet veto, defined in Section 4.2.1.

The presence of a leptonic signature in the event is ensured by electron and muon HLT triggers [84] with various requirements on the lepton p_{T} threshold as well as the isolation and quality selections, during the data recording of the ATLAS detector. The trigger criteria depend on the data taking periods, to account for the increased rates at which data is written, with increasing performance of the LHC. For data recorded during collisions in 2015 (2016), three electron triggers are used with a p_{T} threshold of 24 (24), 60 (60), and 120 (140) GeV and the requirement to pass the *MediumLH* (*TightLH*), *MediumLH* (*MediumLH*), and *LooseLH* (*LooseLH*) criteria, respectively. For muons, two triggers with a respective p_{T} threshold of 20 (24) and 50 (50) GeV are chosen, where the lower p_{T} threshold is accompanied with a loose(medium) requirement on isolation. Furthermore, for 2016 collisions an additional requirement on loose isolation is introduced to the electron trigger with the lowest p_{T} threshold. If an event is selected by any of the triggers for the respective data taking period, it is considered for further analysis. An overview of all triggers used in the analysis is shown in Table 4.2, denoted with the ATLAS specific naming convention. Simulated events are corrected according to the difference in trigger efficiency between data and simulation, as measured in $Z \to \ell\ell$ events [39, 42].

Exactly one electron and one muon, satisfying the *signal* criteria described in Section 4.2.1,

Year	Name	Description
2015	HLT_e24_lhmedium_L1EM20VH	$p_{\mathrm{T}} > 24$ GeV, *MediumLH* quality
	HLT_e60_lhmedium	$p_{\mathrm{T}} > 60$ GeV, *MediumLH* quality
	HLT_e120_lhloose	$p_{\mathrm{T}} > 120$ GeV, *LooseLH* quality
	HLT_mu20_iloose_L1MU15	$p_{\mathrm{T}} > 20$ GeV, loose isolation
	HLT_mu50	$p_{\mathrm{T}} > 50$ GeV
2016	HLT_e24_lhtight_nod0_ivarloose	$p_{\mathrm{T}} > 24$ GeV, *TightLH* quality, loose isolation
	HLT_e60_lhmedium	$p_{\mathrm{T}} > 60$ GeV, *MediumLH* quality
	HLT_e140_lhloose_nod0	$p_{\mathrm{T}} > 140$ GeV, *LooseLH* quality
	HLT_mu24_ivarmedium	$p_{\mathrm{T}} > 24$ GeV, medium isolation
	HLT_mu50	$p_{\mathrm{T}} > 50$ GeV

Table 4.2: The HLT triggers used in the analysis.

are selected to form the pair of leptons associated to the fully leptonic decay of a W boson pair. The dilepton pair has to be charge neutral and its invariant mass (m_{LL}) is required to be larger than 10 GeV, to remove signatures from low-mass hadron resonances, like the Υ meson. The lepton with the higher p_{T}, denoted as the "leading" one, is required to have $p_{\mathrm{T,L}}^{\mathrm{LEAD}} > 25$ GeV. The second, "sub-leading " lepton must satisfy the p_{T} requirement employed in Section 4.2.1. If any additional lepton is found, satisfying the full *signal* lepton requirements with the loosened *GradientLoose* isolation selection (see Section 4.2.1), the event is omitted to reduce background coming from diboson and triboson decays with three or more charged leptons. Finally, at least one of the selected leptons is required to be associated to one of the triggers that selected the event. The reconstructed angular direction of the lepton is matched to the directional information of the trigger decision, to be in close proximity in the η-ϕ plane. The matched lepton is required to have a p_{T} of at least 25 GeV, to ensure that it is above the lowest p_{T} threshold of the triggers used. For muons in 2015 collisions, this requirement is reduced to $p_{\mathrm{T,L}} > 21$ GeV.

Pileup Reweighting

MC simulated events are generated with a pre-defined distribution of $\overline{N}_{\mathrm{INT.}}$, which reflects the pileup for a certain running period. The distribution is set to the best estimate on the expectation for the combined data taken in 2015 and 2016. In order to reflect the observation in data with the MC simulation, a pileup reweighting (PRW) is applied [85]. The luminosity weighted information on $\overline{N}_{\mathrm{INT.}}$, for all data runs considered, is used to evaluate and apply weights for each MC simulated event. The data distribution is scaled by a factor of $\frac{1}{1.16}$ before the PRW evaluation is performed, to compromise on the agreement between data and MC simulation for the distribution of $\overline{N}_{\mathrm{INT.}}$ and the number of primary vertices (N_{PV}). Figure 4.3 shows the comparison of both distributions after the pre-selection, before and after the PRW is applied.

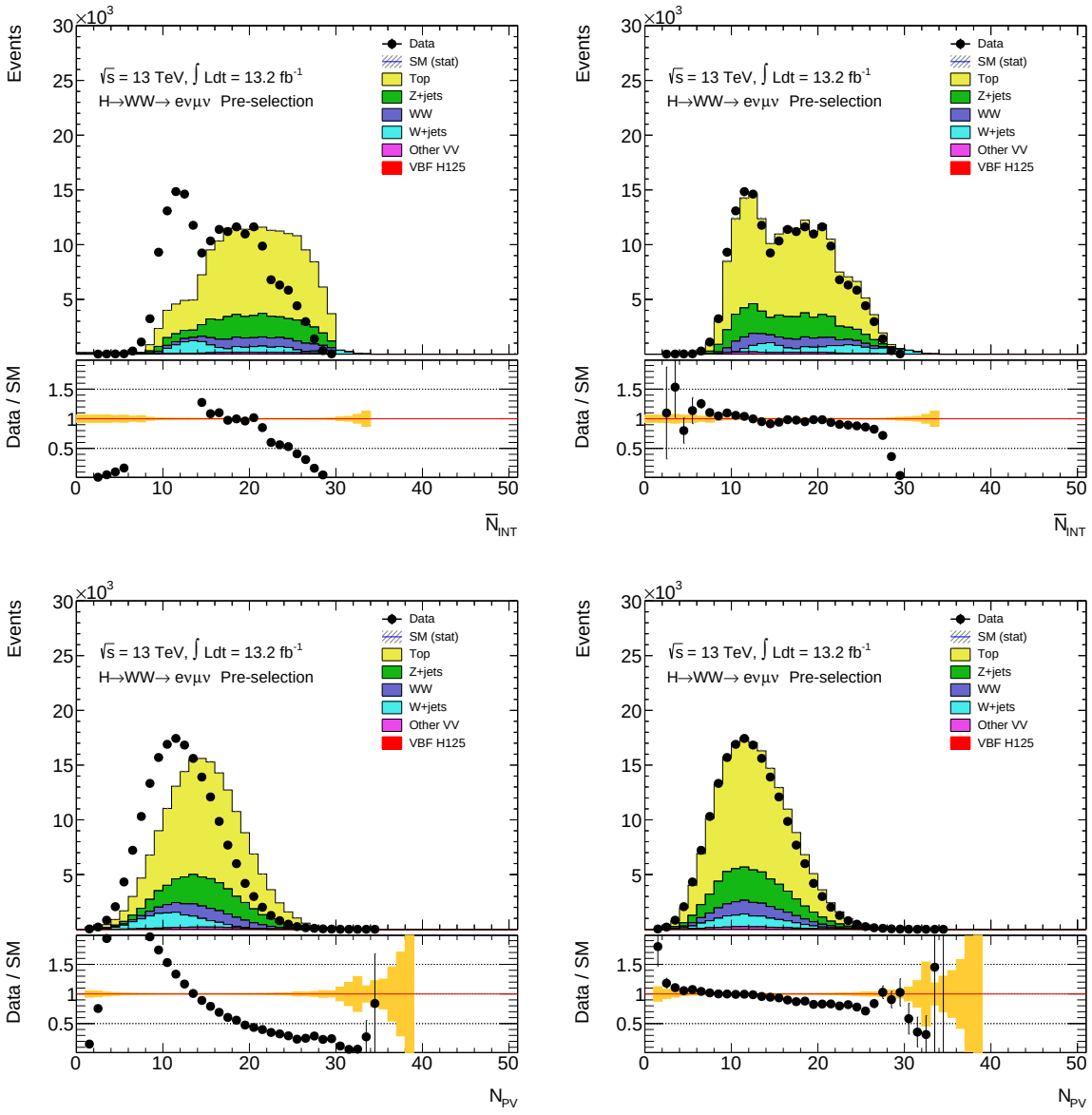

Figure 4.3: The distributions of $\overline{N}_{\mathrm{INT.}}$ (top) and N_{PV} (bottom), before (left) and after (right) applying the pileup reweighting, after all pre-selection requirements are fulfilled. The hatched band in the top panel and the shaded band in the bottom panel depict the statistical uncertainty on the full background. The data distribution of $\overline{N}_{\mathrm{INT.}}$ after the reweighting is shifted by a factor of $\frac{1}{1.16}$, to reflect the data scaling in the PRW procedure.

Signal Selection

The pre-selection criteria reflect the general features of a fully leptonic decay of a W boson pair. Additional requirements are employed to target the decay topology of a high-mass spin-0 boson, while also further reducing contributions from background processes. The large contamination by processes involving top quark decays is reduced drastically by demanding the absence of b-jets ($N_{b\text{-JET}} = 0$), according to the definition in Section 4.2.1. Further requirements exploit kinematic properties of the leptons characteristic for a heavy scalar boson decay.

The p_{T} distributions of the two leptons after the pre-selection are depicted in Figure 4.4a and 4.4b, showing the stacked background contributions as well as the scaled NWA ggF signal interpretation for a heavy boson mass of 300 and 700 GeV. The signal distributions are shifted to higher values compared to the background spectrum, which increases with the mass of the heavy boson. The p_{T} of the leading lepton ($p_{\mathrm{T,L}}^{\mathrm{LEAD}}$) is required to be at least 45 GeV while the sub-leading lepton p_{T} ($p_{\mathrm{T,L}}^{\mathrm{SUBLEAD}}$) is selected to be 30 GeV or higher. This provides a high suppression of background processes for which low kinematic properties of the leptons are characteristic, such as SM Higgs boson decays, misidentified lepton backgrounds (W + jets), and decays from Z + jets events. The lepton criteria are also chosen to preserve a high selection efficiency of the heavy Higgs signal, where the lowest considered mass of 300 GeV is used as references.

The high mass of the hypothesised heavy boson translates to a high invariant mass of the dilepton pair, which is depicted in Figure 4.4c. With increasing mass of the heavy boson, the signal distribution of m_{LL} shifts to higher values, while background contributions are predominantly located at lower values of the m_{LL} spectrum. A requirement of $m_{\mathrm{LL}} > 55$ GeV is chosen to further suppress contributions from SM Higgs boson, W + jets, and Z + jets decays, while preserving a high selection efficiency of the signal.

Figure 4.4d shows the separation in η between the two leptons ($\Delta\eta_{\mathrm{LL}}$), which is used to exploit the spin correlation between leptons originating from the $H \to W^+W^- \to \ell^+\nu\ell^-\bar{\nu}$ decay (see Section 2.3.1). An upper selection requirement of 1.8 further discriminates between signal and background, while it is also used for the definition of the data control regions for the WW background (see Section 4.3.2).

Residual contributions from Z+jets decays are suppressed with a selection on the maximum transverse lepton mass ($m_{\mathrm{T,L}}^{\mathrm{MAX}}$), which is defined as

$$m_{\mathrm{T,L}}^{\mathrm{MAX}} = max\left(m_{\mathrm{T,L}}^{\mathrm{LEAD}}, m_{\mathrm{T,L}}^{\mathrm{SUBLEAD}}\right), \tag{4.2}$$

with

$$m_{\mathrm{T,L}}^{(\mathrm{SUB})\mathrm{LEAD}} = \sqrt{2 \cdot \left(p_{\mathrm{T,L}}^{(\mathrm{SUB})\mathrm{LEAD}} E_{\mathrm{T}}^{\mathrm{MISS}} - \boldsymbol{p}_{\mathrm{T,L}}^{(\mathrm{SUB})\mathrm{LEAD}} \cdot \boldsymbol{E}_{\mathrm{T}}^{\mathrm{MISS}}\right)}. \tag{4.3}$$

The distribution of $m_{\mathrm{T,L}}^{\mathrm{MAX}}$ is shown in Figure 4.5. The Z + jets contributions are distinctly located at lower values compared to other background processes and the signal. A selection requirement of $m_{\mathrm{T,L}}^{\mathrm{MAX}} > 50$ GeV was found to give a good suppression of the remaining Z + jets contamination.

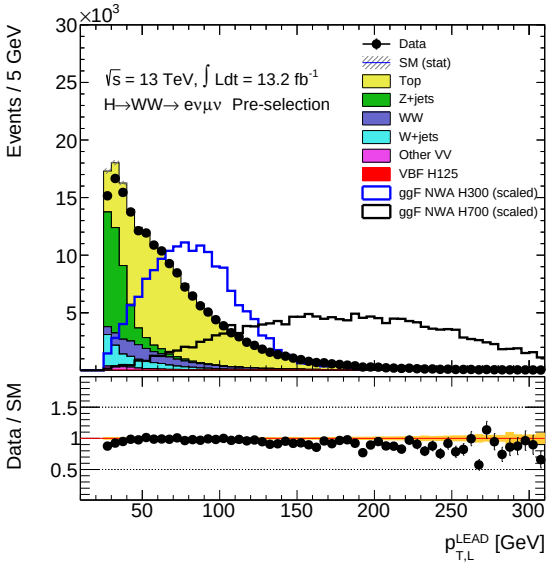

(a) $p_{\mathrm{T,L}}^{\mathrm{LEAD}}$

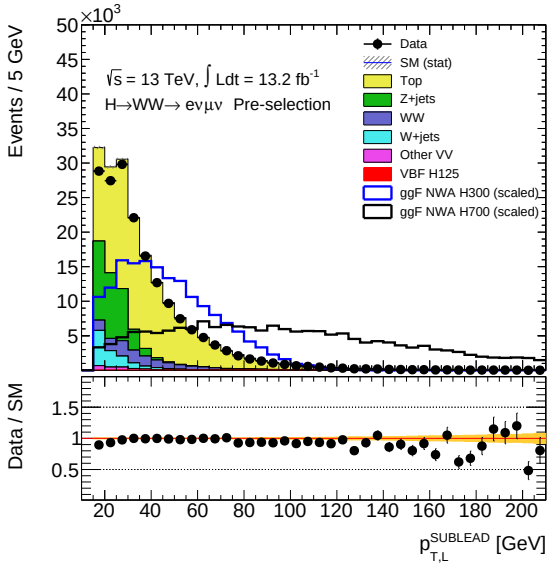

(b) $p_{\mathrm{T,L}}^{\mathrm{SUBLEAD}}$

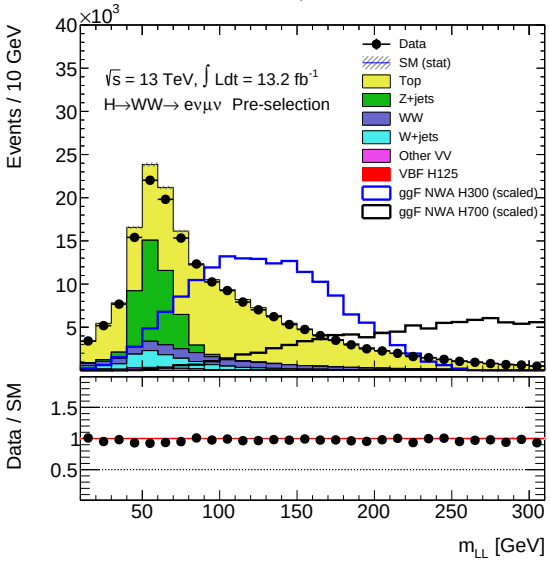

(c) m_{LL}

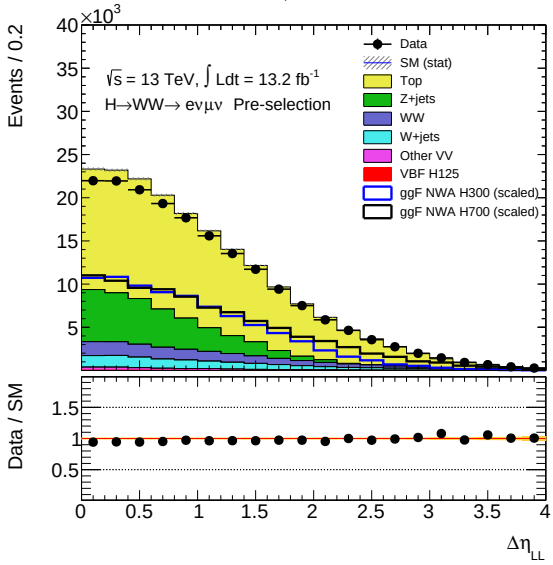

(d) $\Delta\eta_{\mathrm{LL}}$

Figure 4.4: The distribution of $p_{\mathrm{T,L}}^{\mathrm{LEAD}}$ (a), $p_{\mathrm{T,L}}^{\mathrm{SUBLEAD}}$ (b), m_{LL} (c), and $\Delta\eta_{\mathrm{LL}}$ (d) for the stacked background contributions and the NWA ggF signal interpretation at mass values of 300 (blue) and 700 GeV (black), after all pre-selection requirements are fulfilled. The hatched band in the top panel and the shaded band in the bottom panel depict the statistical uncertainty on the full background.

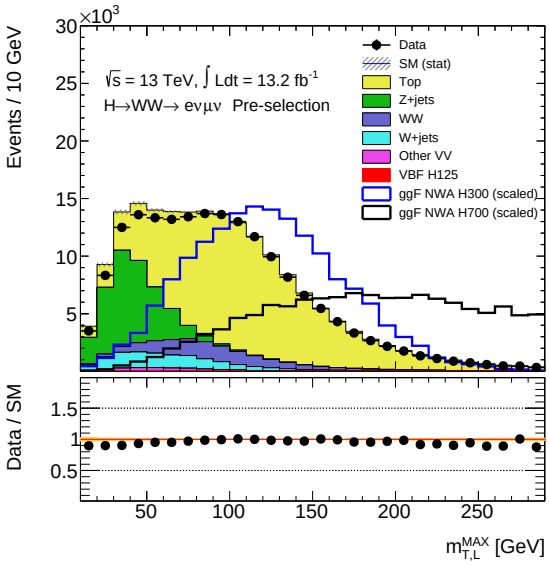

Figure 4.5: The distribution of $m_{\mathrm{T,L}}^{\mathrm{MAX}}$ for the stacked background contributions and the NWA ggF signal interpretation at mass values of 300 (blue) and 700 GeV (black), after all pre-selection requirements are fulfilled. The hatched band in the top panel and the shaded band in the bottom panel depict the statistical uncertainty on the full background.

Signal Categorisation

The distinct topology of the VBF production mode allows to exploit the characteristic properties of kinematic variables related to the additional jets in the event. The sensitivity on a heavy Higgs boson produced with VBF is substantially enhanced by employing further requirements on the invariant mass of the two leading jets (m_{JJ}) and their separation in rapidity (ΔY_{JJ}), if at least two *signal* jets are found ($N_{\mathrm{JET}} \geq 2$). For the case that exactly one *signal* jet is identified ($N_{\mathrm{JET}} = 1$), additional selections are applied on the pseudo-rapidity of the jet (η_{J}) and the minimum separation in η between the jet and one of the leptons

$$\Delta\eta_{\mathrm{LJ}}^{\mathrm{MIN}} = min\left(\Delta\eta_{\mathrm{LJ}}^{\mathrm{LEAD}}, \Delta\eta_{\mathrm{LJ}}^{\mathrm{SUBLEAD}}\right). \tag{4.4}$$

The two leading jets in the event represent the associated jets in the VBF production mode. Consequently, a large separation in rapidity is expected between them, reflecting the decay topology of two high energy jets in opposite direction. This is depicted in Figure 4.6a, where the clear separation between the background and the VBF signal in the ΔY_{JJ} distribution is shown. Furthermore, a large invariant mass of the two highly energetic jets is expected. As shown in Figure 4.6b, the VBF signal is distributed over a large range in m_{JJ} whereas the background is predominantly located at lower values.
In a significant fraction of VBF signal events, only one *signal* jet passes the selection requirements. This prevents the use of kinematic properties related to the dijet system, but the characteristic orientation of the jet close to the proton beam line is still a good handle to isolate the VBF signal. Figure 4.6c depicts the distribution of η_{J}, where a clear

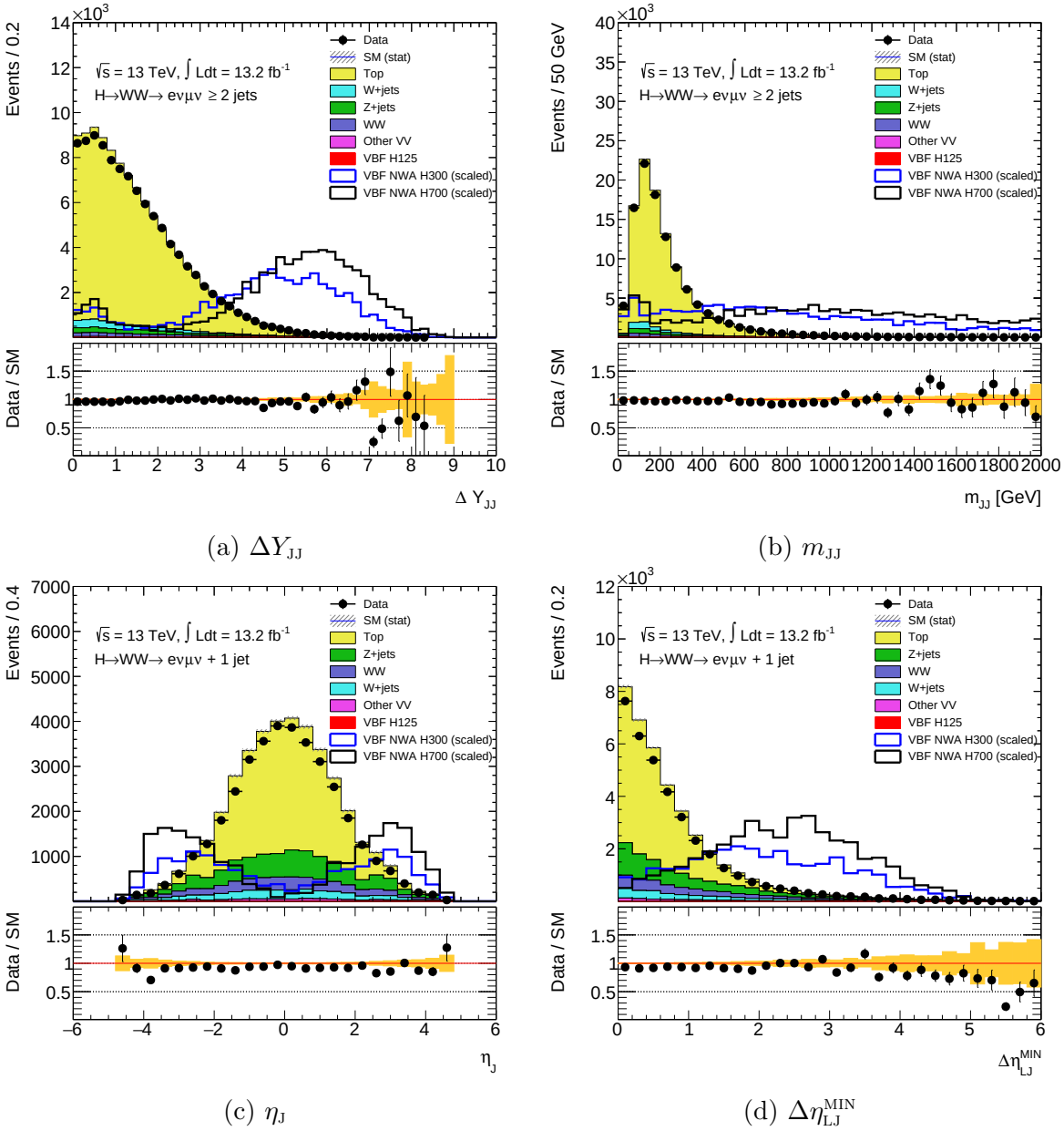

(a) ΔY_{JJ} (b) m_{JJ}

(c) η_{J} (d) $\Delta\eta_{\mathrm{LJ}}^{\mathrm{MIN}}$

Figure 4.6: The distribution of ΔY_{JJ} (a), m_{JJ} (b), η_{J} (c), and $\Delta\eta_{\mathrm{LJ}}^{\mathrm{MIN}}$ (d) for the stacked background contributions and the NWA VBF signal interpretation at mass values of 300 (blue) and 700 GeV (black), after all pre-selection requirements and additional selections on $N_{\mathrm{JET}} \geq 2$ (ΔY_{JJ} and m_{JJ}) and $N_{\mathrm{JET}} = 1$ (η_{J} and $\Delta\eta_{\mathrm{LJ}}^{\mathrm{MIN}}$) are fulfilled. The hatched band in the top panel and the shaded band in the bottom panel depict the statistical uncertainty on the full background.

Pre-selection	Event cleaning Trigger selection One muon and one electron with opposite charge Trigger matching $p_{\mathrm{T,L}}^{\mathrm{LEAD}} > 25$ GeV, $p_{\mathrm{T,L}}^{\mathrm{SUBLEAD}} > 15$ GeV No additional lepton with $p_{\mathrm{T,L}} > 15$ GeV $m_{\mathrm{LL}} > 10$ GeV		
Background suppression	$N_{b\text{-JET}} = 0$ $m_{\mathrm{T,L}}^{\mathrm{MAX}} > 50$ GeV		
High-mass topology $H \to W^+W^- \to \ell^+\nu\ell^-\bar{\nu}$	$\Delta\eta_{\mathrm{LL}} < 1.8$ $m_{\mathrm{LL}} > 55$ GeV $p_{\mathrm{T,L}}^{\mathrm{LEAD}} > 45$ GeV $p_{\mathrm{T,L}}^{\mathrm{SUBLEAD}} > 30$ GeV		
Categories	ggF	VBF 1J	VBF 2J
Description	not VBF 2J not VBF 1J	$N_{\mathrm{JET}} = 1$ $\lvert\eta_{\mathrm{J}}\rvert > 2.4$ $\Delta\eta_{\mathrm{LJ}}^{\mathrm{MIN}} > 1.75$	$N_{\mathrm{JET}} \geq 2$ $m_{\mathrm{JJ}} > 500$ GeV $\Delta Y_{\mathrm{JJ}} > 4$

Table 4.3: Summary of the pre- and signal selection requirements and the signal categorisation of the analysis.

separation is shown between the background, for which the jet is predominantly in the central detector region, and the VBF signal. Furthermore, the separation in η between the two leptons and the jet is expected to be small in background decays, but large in the VBF signal process where the leptonic decay of the W bosons is occurring in the central η region. This is demonstrated in Figure 4.6d, which shows the distinct separation between the VBF signal and the background contributions in the $\Delta\eta_{\mathrm{LJ}}^{\mathrm{MIN}}$ distribution.

The selection on m_{JJ}, ΔY_{JJ}, η_{J}, and $\Delta\eta_{\mathrm{LJ}}^{\mathrm{MIN}}$ defines in total three signal categories. Events with at least two *signal* jets, where $m_{\mathrm{JJ}} > 500$ GeV and $\Delta Y_{\mathrm{JJ}} > 4$ is satisfied, are assigned to the VBF 2J category. If exactly one *signal* jet is found, while $|\eta_{\mathrm{J}}| > 2.4$ and $\Delta\eta_{\mathrm{LJ}}^{\mathrm{MIN}} > 1.75$ is fulfilled, the event falls into the VBF 1J category. Finally, all events that do not satisfy the requirements of either the VBF 2J or the VBF 1J category are grouped in the ggF category. This makes the ggF category inclusive in jet multiplicity, except for the small, separated jet phase space targeted at the VBF topology.
Table 4.3 shows the summary of the full pre- and signal selection as well as the signal categorisation used in the analysis, which defines the ggF ($\mathrm{SR_{ggF}}$), VBF 1J ($\mathrm{SR_{VBF\ 1J}}$) and VBF 2J ($\mathrm{SR_{VBF\ 2J}}$) signal region.

The invariant mass spectrum reconstructed from the Higgs decay products provides a

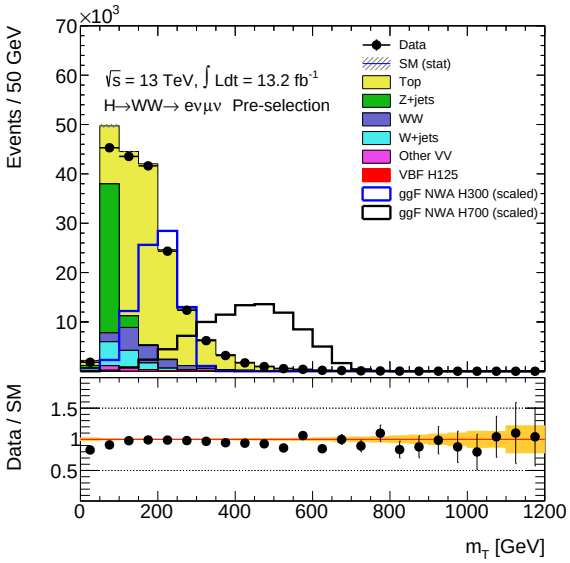

Figure 4.7: The distribution of m_{T} for the stacked background contributions and the NWA ggF signal interpretation at mass values of 300 (blue) and 700 GeV (black), after all pre-selection requirements are fulfilled. The hatched band in the top panel and the shaded band in the bottom panel depict the statistical uncertainty on the full background.

good observable to identify a high-mass resonance, since SM background processes show only non-resonant behaviour in the mass range beyond the Z boson mass. For the $H \to W^+W^- \to \ell^+\nu\ell^-\bar{\nu}$ decay channel, the two neutrinos prevent the full reconstruction of the invariant mass of the Higgs boson, since they can only be taken into account as missing momentum in the transverse plane of the detector (see Section 3.3.6). The transverse mass m_{T} is reconstructed from the two leptons and the $\boldsymbol{E}_{\mathrm{T}}^{\mathrm{MISS}}$:

$$m_{\mathrm{T}} = \sqrt{(E_{\mathrm{T,LL}} + E_{\mathrm{T}}^{\mathrm{MISS}})^2 - \left|\boldsymbol{p}_{\mathrm{T,LL}} + \boldsymbol{E}_{\mathrm{T}}^{\mathrm{MISS}}\right|^2}, \tag{4.5}$$

with

$$E_{\mathrm{T,LL}} = \sqrt{\left|\boldsymbol{p}_{\mathrm{T,LL}}\right|^2 + m_{\mathrm{LL}}^2}. \tag{4.6}$$

As demonstrated in Figure 4.7, the m_{T} distribution of a heavy scalar boson decay shows a broad resonant behaviour below the hypothesised heavy boson mass, but still provides a good discrimination between the signal and the combined SM background, which is located predominantly in the lower range of the m_{T} spectrum. It is used as the main observable to identify a resonant signal excess above the SM background in the statistical evaluation described in Section 4.6.

ggF Top	ggF WW	VBF Top	VBF 1J WW
$N_{b\text{-JET}} = 1$	$N_{b\text{-JET}} = 0$	$N_{b\text{-JET}} \geq 1$	$N_{b\text{-JET}} = 0$
$\Delta\eta_{\text{LL}} < 1.8$	$\Delta\eta_{\text{LL}} > 1.8$	-	$\Delta\eta_{\text{LL}} > 1.8$ or $m_{\text{LL}} < 55$ GeV
$m_{\text{T,L}}^{\text{MAX}} > 50$ GeV		-	-
$m_{\text{LL}} > 55$ GeV		-	-
$p_{\text{T,L}}^{\text{LEAD}} > 45$ GeV		$p_{\text{T,L}}^{\text{LEAD}} > 25$ GeV	
$p_{\text{T,L}}^{\text{SUBLEAD}} > 30$ GeV		$p_{\text{T,L}}^{\text{SUBLEAD}} > 15$ GeV	$p_{\text{T,L}}^{\text{SUBLEAD}} > 25$ GeV

Table 4.4: Summary of the control region requirements after pre-selection and signal categorisation.

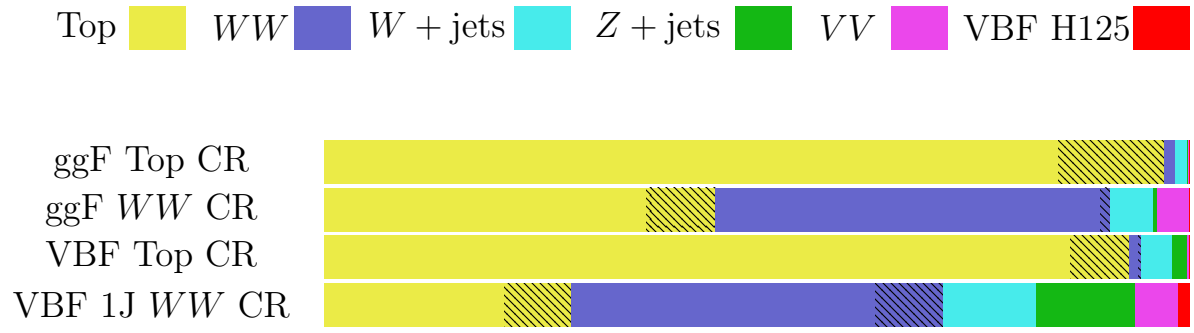

Figure 4.8: The relative background contributions in the top quark and WW background control regions. The hatched areas indicate the relative contribution of the tW and $gg \to WW$ process to the top quark and WW background, respectively.

4.3 Background Modelling

Background contamination for the analysis selection described in Section 4.2.2 comes from processes with similar signatures to the $H \to W^+W^- \to \ell^+\nu\ell^-\bar{\nu}$ signal topology, either containing real leptons, or jets which are misidentified as electrons or muons. As demonstrated in Figure 4.2, the main background processes are decays involving top quarks and the non-resonant W boson pair production, which are discussed in Section 4.3.1 and 4.3.2. Predictions from MC simulated events are used for the description of kinematic distributions. The normalisation of these backgrounds is estimated by dedicated data control regions, except for the WW background in the VBF 2J SR, where the kinematic distributions and the normalisation are estimated from MC simulation. The selection criteria for the top quark and WW background control regions are summarised in Table 4.4 and the relative background compositions in these regions are depicted in Figure 4.8.
Additional small contributions come from Z + jets decays to a lepton pair (electrons, muons, or taus) and diboson processes other than WW, including WZ, ZZ, $W\gamma$, $W\gamma^*$, and $Z\gamma$ decays, which are denoted as VV. For these backgrounds the prediction from MC simulation is used for the kinematic distribution and normalisation description. Finally, the

contamination of events coming from the production of a single W boson with associated jets is estimated with a data-driven technique, which is described in Section 4.3.3.

4.3.1 Top Quark Background

The background contributions induced by top quark decays predominantly come from top quark pair production, with a small fraction from processes containing a single top quark in association with a W boson, indicated by the hatched area in Figure 4.2 and 4.8. Both background processes provide a topology with two real W bosons, satisfying the requirements employed on the leptons, as well as one or two b-jets. The b-jet veto applied in the analysis selection highly suppresses top quark background contributions by a factor of 10. Still, a large fraction of the background composition comes from top quark decays, due to the limited efficiency of the b-jet identification and the large cross section of the $t\bar{t}$ process. This is particularly true for the VBF 2J category, where top quark induced decays are the dominant background source, as demonstrated in Figure 4.2.
The normalisation of the top quark background contributions in the different signal regions is estimated using two separate control regions. The ggF Top CR ($\mathrm{CR}^{\mathrm{Top}}_{\mathrm{ggF}}$) is defined with almost the same selection as the ggF SR, to stay as close as possible to the kinematic phase space of the signal selection. An orthogonal selection to the SR is achieved by the requirement that exactly one b-jet is present in the event, which also yields a very high purity in top quark background events of $\sim 98\%$. This high amount of purity also allows to identify a mismodelling of the top quark induced background, which manifests as a discrepancy between data and MC simulation in the distribution of $p_{\mathrm{T,L}}^{\mathrm{LEAD}}$, depicted in Figure 4.9a. The discrepancy is clearly visible and gets larger with increasing value of $p_{\mathrm{T,L}}^{\mathrm{LEAD}}$. The difference in data and MC simulation is fitted according to a linear function $f^{\mathrm{CORR}}_{p_{\mathrm{T,LEP}}}$, described by

$$f^{\mathrm{CORR}}_{p_{\mathrm{T,LEP}}} = 1.108 - 1.15 \cdot 10^{-3} \frac{p_{\mathrm{T,L}}^{\mathrm{LEAD}}}{\mathrm{GeV}}, \tag{4.7}$$

which is used in the ggF SR, as well as in the ggF Top CR and ggF WW CR, to correct the top quark background contributions [86–88]. The impact of the correction on the $p_{\mathrm{T,L}}^{\mathrm{LEAD}}$ distribution in the ggF Top CR is shown in Figure 4.9b. The agreement between data and MC simulation with respect to the description of the $p_{\mathrm{T,L}}^{\mathrm{LEAD}}$ shape increases significantly.
The mismodelling observed in the $p_{\mathrm{T,L}}^{\mathrm{LEAD}}$ distribution also leads to a significant discrepancy between data and MC simulation in the description of the m_{T} distribution in the ggF Top CR, as shown in Figure 4.10a. In particular in the high m_{T} region, which is most relevant for the high-mass signal, the large disagreement between data and the combined background is clearly visible. The description of the m_{T} shape in the ggF Top CR significantly improves when the $p_{\mathrm{T,L}}^{\mathrm{LEAD}}$ correction according to Eq. 4.7 is applied, which is demonstrated in Figure 4.10b.
The categorisation according to VBF 1J and VBF 2J leads to a limited statistical precision for the modelling of the top quark background. For that reason, the normalisation of the top quark background contributions in the respective VBF signal regions is estimated using

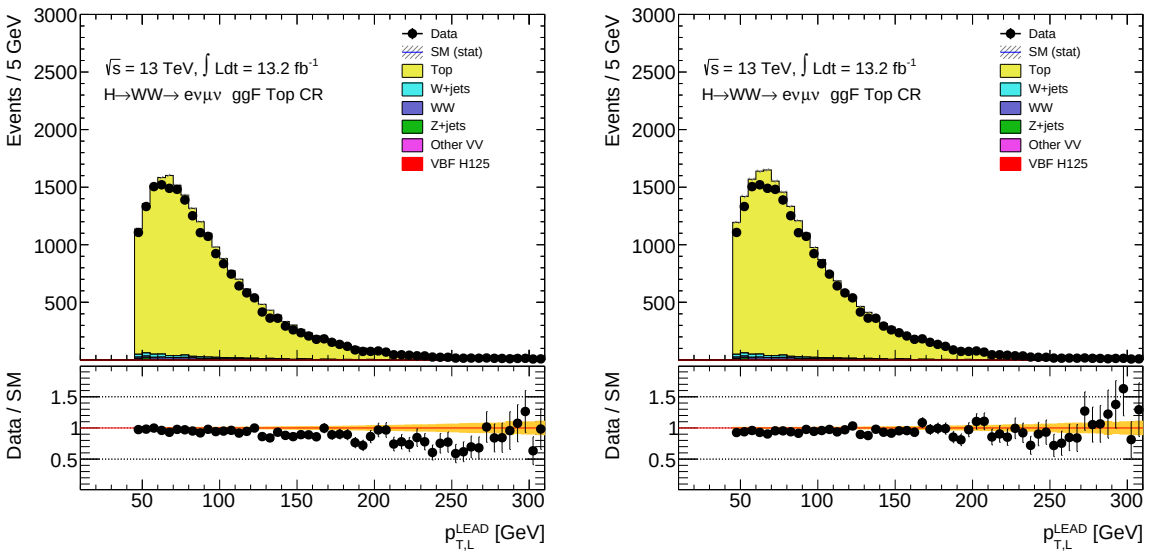

(a) $p_{\mathrm{T,L}}^{\mathrm{LEAD}}$ before correction (b) $p_{\mathrm{T,L}}^{\mathrm{LEAD}}$ after correction

Figure 4.9: The distribution of $p_{\mathrm{T,L}}^{\mathrm{LEAD}}$ in the ggF Top CR, before (a) and after (b) the correction on $p_{\mathrm{T,L}}^{\mathrm{LEAD}}$, described in Eq. 4.7. The hatched band in the top panel and the shaded band in the bottom panel depict the statistical uncertainty on the full background.

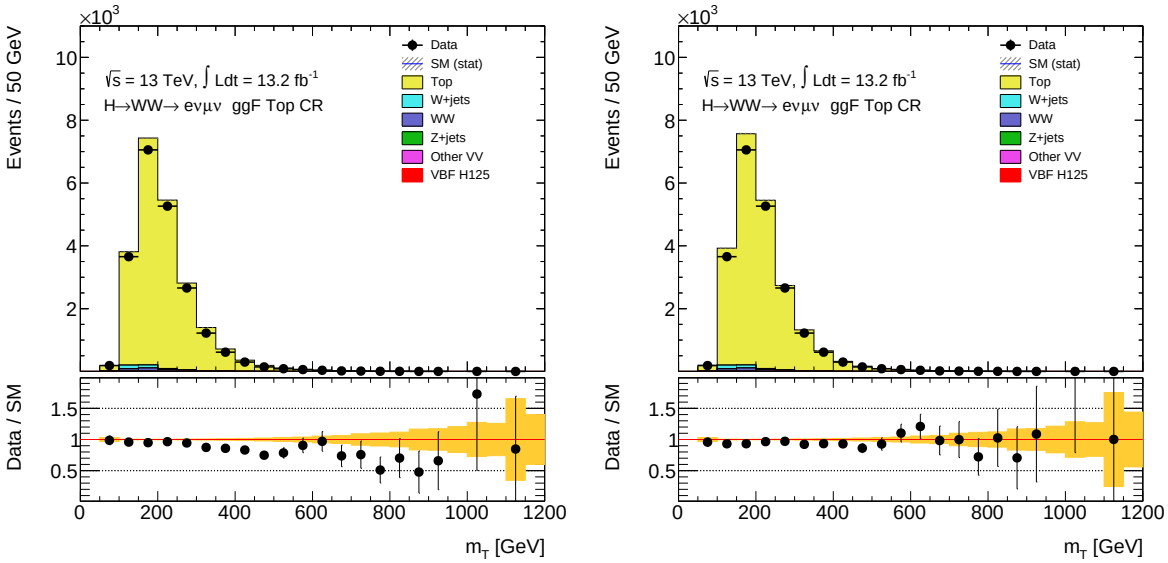

(a) m_{T} before $p_{\mathrm{T,L}}^{\mathrm{LEAD}}$ correction (b) m_{T} after $p_{\mathrm{T,L}}^{\mathrm{LEAD}}$ correction

Figure 4.10: The distribution of m_{T} in the ggF Top CR, before (a) and after (b) the correction on $p_{\mathrm{T,L}}^{\mathrm{LEAD}}$, described in Eq. 4.7. The hatched band in the top panel and the shaded band in the bottom panel depict the statistical uncertainty on the full background.

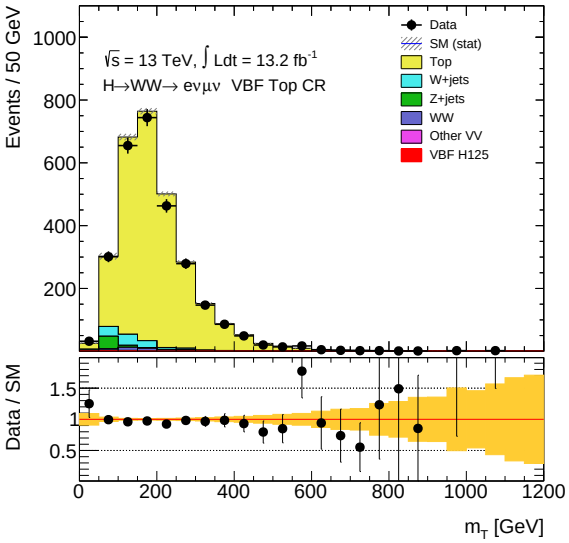

Figure 4.11: The distribution of m_{T} in the VBF Top CR. The hatched band in the top panel and the shaded band in the bottom panel depict the statistical uncertainty on the full background.

one inclusive VBF Top CR ($\mathrm{CR}^{\mathrm{Top}}_{\mathrm{VBF}}$). Events are considered for this CR, if they fulfil the pre-selection requirements as well as either the VBF 1J or VBF 2J criteria, while also at least one b-jet is present. The additional SR selections are omitted to further preserve statistical power for this CR, leading to an overall top background purity of $\sim 90\%$.
The mismodelling observed in the ggF Top CR does not significantly manifest in the VBF Top CR, within the statistical precision of this region. For that reason, no further corrections on the top background are applied in the VBF regions. Figure 4.11 shows the m_{T} distribution of the VBF Top CR.

4.3.2 *W* Boson Pair Background

The background coming from the non-resonant, fully leptonic decay of a W boson pair produces an identical topology to the one from the signal high-mass scalar boson. This makes the suppression of the WW background particularly difficult and the definition of control regions with sufficient purity of events from WW decays challenging. The WW background mainly consists of $qq \to WW$ processes with a small contribution from $gg \to WW$, which is indicated by the hatched area in Figure 4.2 and 4.8.
The normalisation of WW background contributions in the ggF SR is estimated with the ggF WW CR ($\mathrm{CR}^{WW}_{\mathrm{ggF}}$). For this CR, the same selection requirements as for the SR definition are employed, except the selection on $\Delta\eta_{\mathrm{LL}}$, which is inverted to keep the signal and control region definition orthogonal.
The contribution of WW background events amounts to $\sim 24\%$ of the background composition in the VBF 2J SR, as shown in Figure 4.2. Furthermore, the definition of a WW

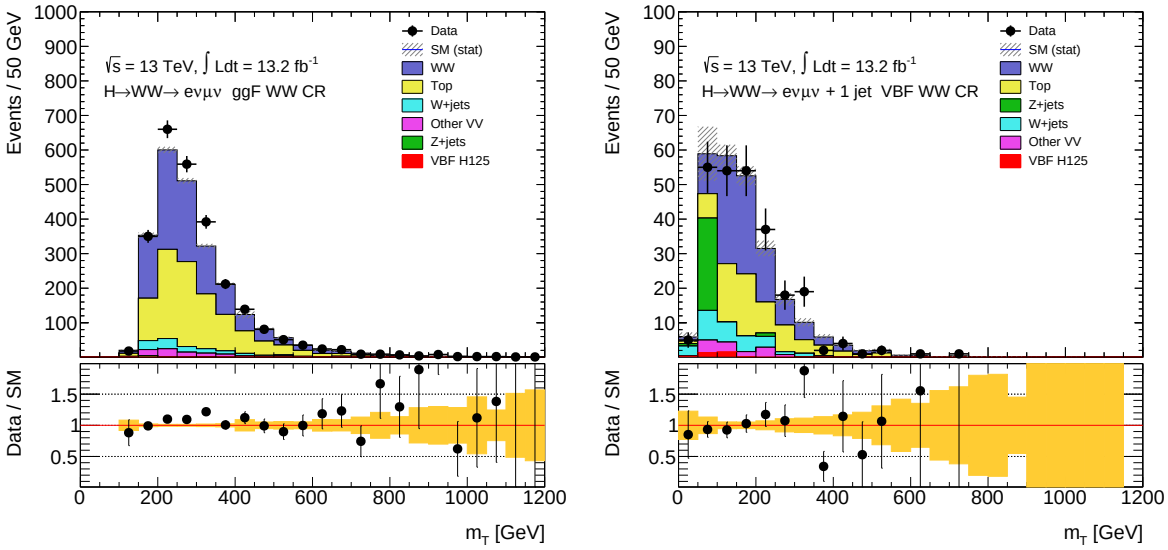

(a) ggF WW CR (b) VBF 1J WW CR

Figure 4.12: The distribution of m_{T} in the ggF (a) and VBF 1J (b) WW CR. The hatched band in the top panel and the shaded band in the bottom panel depict the statistical uncertainty on the full background.

CR in this category with sufficient purity was found to be very difficult. For these reasons, the prediction from MC simulation is used to estimate the WW background normalisation in the VBF 2J SR.

Finally, a dedicated VBF 1J WW CR ($\mathrm{CR}^{WW}_{\mathrm{VBF\ 1J}}$) is defined to estimate the normalisation in the VBF 1J SR. In order to preserve statistical precision, several requirements of the SR selection are omitted or loosened. Events considered for this CR have to satisfy the pre-selection criteria, the b-jet veto, and require a leading and sub-leading $p_{\mathrm{T,L}}$ of at least 25 GeV. Furthermore, the separation to the VBF 1J SR is ensured by requiring either $\Delta\eta_{\mathrm{LL}} > 1.8$ or $m_{\mathrm{LL}} < 55$ GeV.

The purity of WW events in the WW control regions is relatively low, with $\sim 46\%$ and $\sim 43\%$ for the ggF WW CR and VBF 1J WW CR, respectively. Still, they provide reliable descriptions of the WW normalisation in the respective signal regions, since the remaining contributions predominantly come from the top quark induced background, which is well constrained by the very pure top quark background control regions used in this analysis. The distribution of m_{T} in the ggF and VBF 1J WW CR is shown in Figure 4.12.

As discussed in Section 4.1, the WW background is evaluated to a limited order of precision in terms of ME calculations. The impact of higher order corrections on gluon and quark induced non-resonant diboson backgrounds has been studied extensively [89] during the Run-I data period of the ATLAS experiment and is shown to have a large impact on the cross section, both inclusive and differential in the invariant diboson mass spectrum or related quantities.

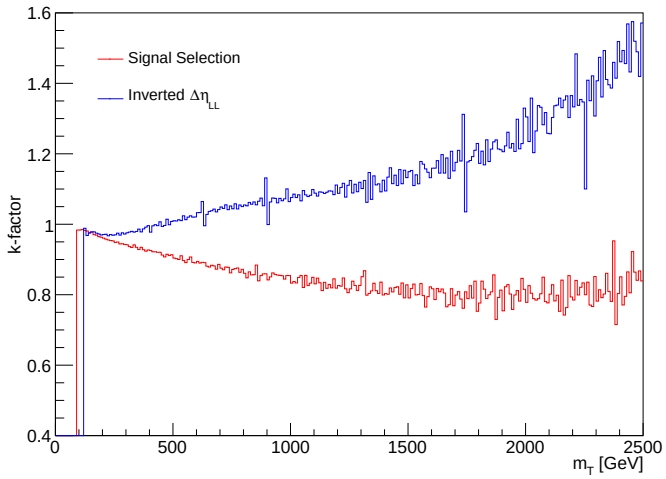

Figure 4.13: Correction factors on the $qq \to WW$ background, according to EW NLO calculations provided by the authors of Ref. [94]. The calculations are evaluated separately for the full signal selection (red) and the signal selection with inverted $\Delta\eta_{\mathrm{LL}}$ requirement (blue), as a function of m_{T}.

For the background contribution coming from the $gg \to WW$ process, an additional k-factor of 1.7 is used to account for higher order corrections on the cross section, following the studies presented in Refs. [90–93].
The effect of higher order EW corrections on the $qq \to WW$ background cross section is shown to have a strong dependency on the invariant mass spectrum of the W boson pair [89], which directly translates to the reconstructed m_{T} distribution. Figure 4.13 shows correction factors as a function of m_{T}, obtained from EW NLO calculations, provided by the authors of Ref. [94]. The calculations are evaluated separately for the full signal selection as well as for the signal selection with an inverted $\Delta\eta_{\mathrm{LL}}$ requirement, to estimate the impact of EW NLO corrections on the differential cross section of this background in the ggF SR and ggF WW CR. The relative corrections for the signal selection range from -2% at $m_{\mathrm{T}} = 100$ GeV to -17% at $m_{\mathrm{T}} = 1000$ GeV, while they show a reversed behaviour for the selection with the inverted $\Delta\eta_{\mathrm{LL}}$ requirement. The corrections on the $qq \to WW$ cross section are used as an additional source of systematic uncertainty on the WW background, which is discussed in Section 4.5.2.

4.3.3 W+jets Background

Background contributions originating from events with one W boson with additional associated jets are selected by misidentification of at least one of the jets, which satisfies the lepton requirements described in Section 4.2.1. Although quality criteria on the leptons are optimised to suppress the rate of these misidentifications to happen, the very large production cross section of the single W boson production mode still leads to a sizeable

contamination of this background process. The $W+$jets background is estimated with the data-driven fake factor technique of the $H \to W^+W^- \to \ell^+\nu\ell^-\bar{\nu}$ couplings analysis for the published Run-I data results [95], updated for analysis in the Run-II data period of the LHC [96]. Background contributions from multi-jet events, where at least two jets are misidentified as leptons, amount to a very small fraction of the background composition and are neglected.

The fake factor method defines a $W+$ jets control sample selection orthogonal to the signal and control regions in the analysis [95, 96]. The selection is targeted at an enhanced selection rate of jets misidentified as leptons. Events, which are selected in this separate data sample, are scaled by a fake factor, to obtain the correct rate of jet misidentification to occur in the regions used in the analysis.
The $W+$jets selection requires one lepton to pass the full lepton selection criteria, whereas the second lepton has to fail the *signal* lepton selection but fulfil less stringent criteria. In the following, the lepton fulfilling the full *signal* lepton requirements is denoted as *ID* and the one satisfying only the loosened criteria as *anti-ID*.
This selection defines a $W+$jets control sample for each region considered in the analysis, which is used to estimate the shape and normalisation of the $W+$ jets background. The background contribution in the signal and control regions, coming from $W+$ jets decays, is determined by

$$N^{W+\text{jets}}_{\text{ID, ID}} = \left(N_{\text{ID, ANTI-ID}} - N^{\text{EW}}_{\text{ID, ANTI-ID}}\right) \cdot f_{\text{FAKE}}, \tag{4.8}$$

where $N^{W+\text{jets}}_{\text{ID, ID}}$ is the estimate on $W+$ jets events with both leptons being selected as *ID* and $N_{\text{ID, ANTI-ID}}$ is the number of data events selected with one *ID* and one *anti-ID* lepton. The contributions of other background processes in the $W+$ jets sample ($N^{\text{EW}}_{\text{ID, ANTI-ID}}$) is estimated from MC simulation and subtracted from the selected data events. The fake factor f_{FAKE} is defined as

$$f_{\text{FAKE}} = \frac{N_{\text{ID}}}{N_{\text{ANTI-ID}}}, \tag{4.9}$$

which extrapolates the $W+$ jets background rate from the $W+$ jets control sample to the respective region where two *ID* leptons are selected. The fake factors are extracted separately for electrons and muons from a data sample enriched with dijet events, dependent on the p_{T} and η of the misidentified jet. N_{ID} and $N_{\text{ANTI-ID}}$ denote the number of jets passing the *ID* and *anti-ID* selection requirements, respectively.

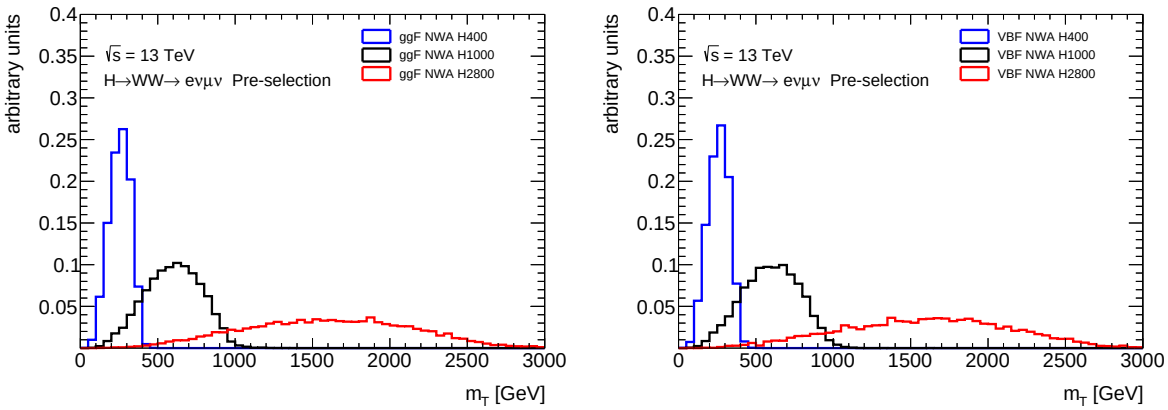

(a) ggF (b) VBF

Figure 4.14: The distribution of m_{T} for the NWA signal interpretation in the ggF (a) and VBF (b) production mode for m_H values of 400 (blue), 1000 (black), and 2800 GeV (red). The distributions are normalised to have an integral of one.

4.4 Signal Modelling

4.4.1 Signal Interpretations

In the context of an extension of the SM Higgs sector, the search for a heavy scalar boson with mass up to 3000 GeV is performed in the analysis described in this thesis. For the statistical results presented in Section 4.7, two signal interpretations are studied.
For the normalisation of the particular signal interpretations, no specific model dependent cross section is assumed. For simplification, the cross sections of all signal processes, independent of m_H and interpretation, are set to 1 pb times the branching ratio of both W bosons decaying leptonically. In particular, no assumption is made on the ratio of the ggF and VBF production mode cross sections.

Narrow Width Approximation

The NWA interpretation assumes a negligible line width of the boson, much smaller than the experimental resolution. The ggF and VBF production modes are considered for the NWA signal with dedicated MC samples and signal categorisations in the analysis, as described in Section 4.1 and 4.2.2. Figure 4.14 shows the m_{T} distribution of NWA signals for the ggF and VBF production mode, with different assumed pole masses m_H of the high-mass boson. The two production channels show very similar behaviour of the m_{T} shape, which indicates that there is little difference of the kinematic properties in the transverse plane between the two modes. This motivates the choice of an identical signal selection in terms of kinematic properties related to the leptons, but a ggF and VBF specific categorisation related to the additional jets in the signal topologies, to exploit the characteristic properties of the predominantly forward oriented jets from VBF production.

The difference between the ggF and VBF NWA signal for several values of m_H, with respect to the lepton variables used in the signal selection in Section 4.2.2, is shown in Figure 4.15.

Large Width Assumption

In addition to the signal interpretation with negligible line width, a heavy scalar boson with a width up to 15% of m_H is studied as hypothetical new particle. The upper value for the considered widths is motivated by constraints on the signal width in the most common BSM models, driven by observations in experimental data. In particular, measurements of the SM Higgs boson signal strength and couplings to SM particles set limits on the coupling parameter of models like 2HDM or EWS [7] and consequently constrain the line width of the predicted heavy Higgs bosons. For the LWA interpretation, only the ggF production mode is considered[2]. Figure 4.16a shows the m_{T} distributions of the LWA signal with $15\% \times m_H$ line width for different masses, compared to the equivalent NWA signal distributions. For low masses of the hypothesised particle, the difference in the shape of the m_{T} distribution between the two width assumptions is relatively small, but gets significantly larger with increasing signal mass. For very high masses, the LWA distribution shows a pronounced shift to smaller values in m_{T} as well as a generally broader spectrum, compared to the NWA signal. This is also reflected in the invariant mass (m_{WW}) spectrum of the two W bosons, reconstructed on the particle level of the MC simulation, which is shown in Figure 4.16b. In particular for very high masses the m_{WW} spectrum shows outliers to low values, which translate to a tendency to lower values in m_{T}.
Events for the LWA interpretation with $15\% \times m_H$ line width are studied using dedicated MC simulated samples for the considered signal masses. Smaller widths are generated by reweighting of the simulated $15\% \times m_H$ width events, according to the ratio f_{WIDTH} of the respective hypothesised particle propagator terms [86, 87, 97]. The definition of f_{WIDTH} is

$$f_{\mathrm{WIDTH}} = \frac{\left(m_{WW}^2 - m_H^2\right)^2 + m_H^2 \cdot \Gamma_{H_{\mathrm{GEN}}}^2}{\left(m_{WW}^2 - m_H^2\right)^2 + m_H^2 \cdot \Gamma_{H_{\mathrm{RWGT}}}^2}. \tag{4.10}$$

where $\Gamma_{H_{\mathrm{GEN}}}$ is the resonance width generated in MC simulation and $\Gamma_{H_{\mathrm{RWGT}}}$ is the width after reweighting. For the statistical results of the analysis presented in this thesis, discussed in Section 4.7, signal widths of 15%, 10%, and 5% of m_H are considered. Figure 4.17 shows the comparison of the different line widths, with respect to the m_{WW} spectrum and the distribution of m_{T}, for different masses of the heavy scalar boson. The LWA m_{T} shape changes to the distribution expected from an NWA signal with incremental reduction of the resonance width, which is consistent with the assumptions made on the line width for the two interpretations.
For the LWA interpretation, the same signal selection as for the NWA hypothesis is used. Variables, that are strongly correlated with the mass spectrum of the heavy boson, show

[2]For the analysis results presented in this thesis, no validated LWA samples for the VBF production mode were available yet.

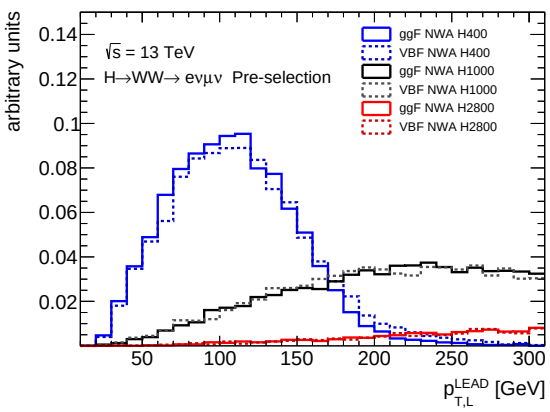

(a) $p_{\mathrm{T,L}}^{\mathrm{LEAD}}$

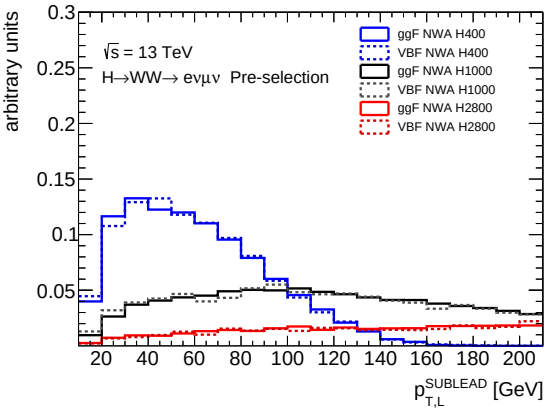

(b) $p_{\mathrm{T,L}}^{\mathrm{SUBLEAD}}$

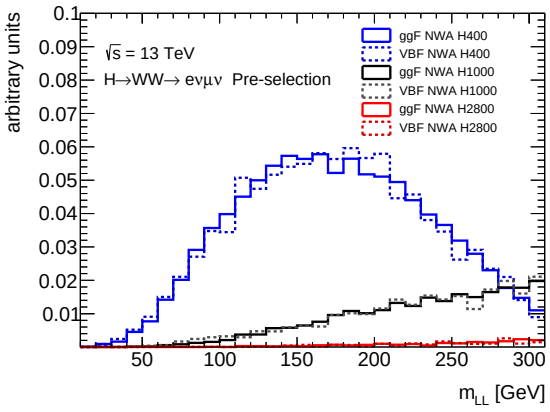

(c) m_{LL}

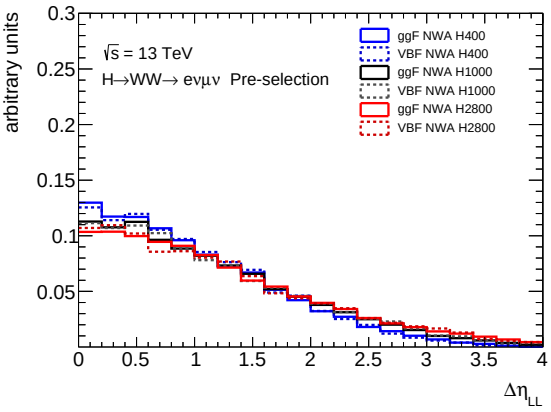

(d) $\Delta\eta_{\mathrm{LL}}$

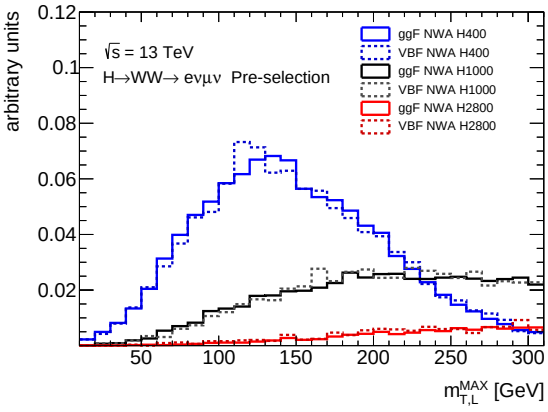

(e) $m_{\mathrm{T,L}}^{\mathrm{MAX}}$

Figure 4.15: The distribution of $p_{\mathrm{T,L}}^{\mathrm{LEAD}}$ (a), $p_{\mathrm{T,L}}^{\mathrm{SUBLEAD}}$ (b), m_{LL} (c), $\Delta\eta_{\mathrm{LL}}$ (d), and $m_{\mathrm{T,L}}^{\mathrm{MAX}}$ (e) for the NWA ggF (solid line) and VBF (dashed line) signal interpretation at m_H values of 400 (blue), 1000 (black), and 2800 GeV (red). The distributions are normalised to have an integral of one.

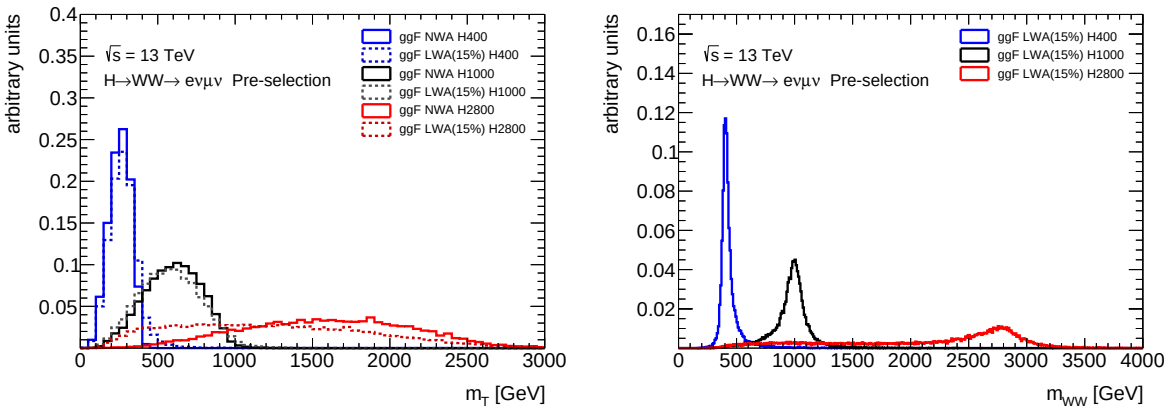

(a) m_{T} (b) m_{WW}

Figure 4.16: The distribution of m_{T} (a), for the NWA (solid line) and LWA (dashed line) signal interpretation, and m_{WW} (b), for the LWA signal interpretation, at m_H values of 400 (blue), 1000 (black), and 2800 GeV (red). The distributions are normalised to have an integral of one.

distinct differences between the two signal types. This is demonstrated in Figure 4.18, which shows the comparison between the NWA and LWA signal of the distributions for the lepton variables used for the signal selection. Still, the inclusive selection requirements employed on the lepton properties ensure similar selection efficiencies for the NWA and LWA interpretations, especially for higher values of the assumed heavy boson mass. Figure 4.19 shows the combined efficiency of all signal requirements after the pre-selection, dependent on the assumed heavy boson mass, for the LWA and NWA signal, respectively.

Signal Category Correction on the NWA ggF Signal

The ggF signal contributions for the NWA interpretation are described insufficiently in the VBF specific signal regions, due to the limited precision of associated jet description of the Powheg+Pythia generated events. For that reason, correction factors are applied to the signal predictions [86, 87, 97], obtained from the comparison of selection rates on particle level between NWA signal events generated with the Powheg and MadGraph5_aMC@NLO generators. The scale factors are defined as

$$f_{\text{VBF NJ}} = \frac{N^{\text{VBF NJ}}_{\text{MadGraph5}} / N^{\text{ggF}}_{\text{MadGraph5}}}{N^{\text{VBF NJ}}_{\text{Powheg}} / N^{\text{ggF}}_{\text{Powheg}}}, \tag{4.11}$$

with the amount of selected events $N^{\text{VBF NJ}}_{\text{MadGraph5}}$ and $N^{\text{ggF}}_{\text{MadGraph5}}$ in the VBF NJ and ggF signal regions, evaluated with MadGraph5 simulation. VBF NJ denotes either the VBF 1J or VBF 2J signal category. The respective predictions for Powheg generated events are $N^{\text{VBF NJ}}_{\text{Powheg}}$ and $N^{\text{ggF}}_{\text{Powheg}}$.

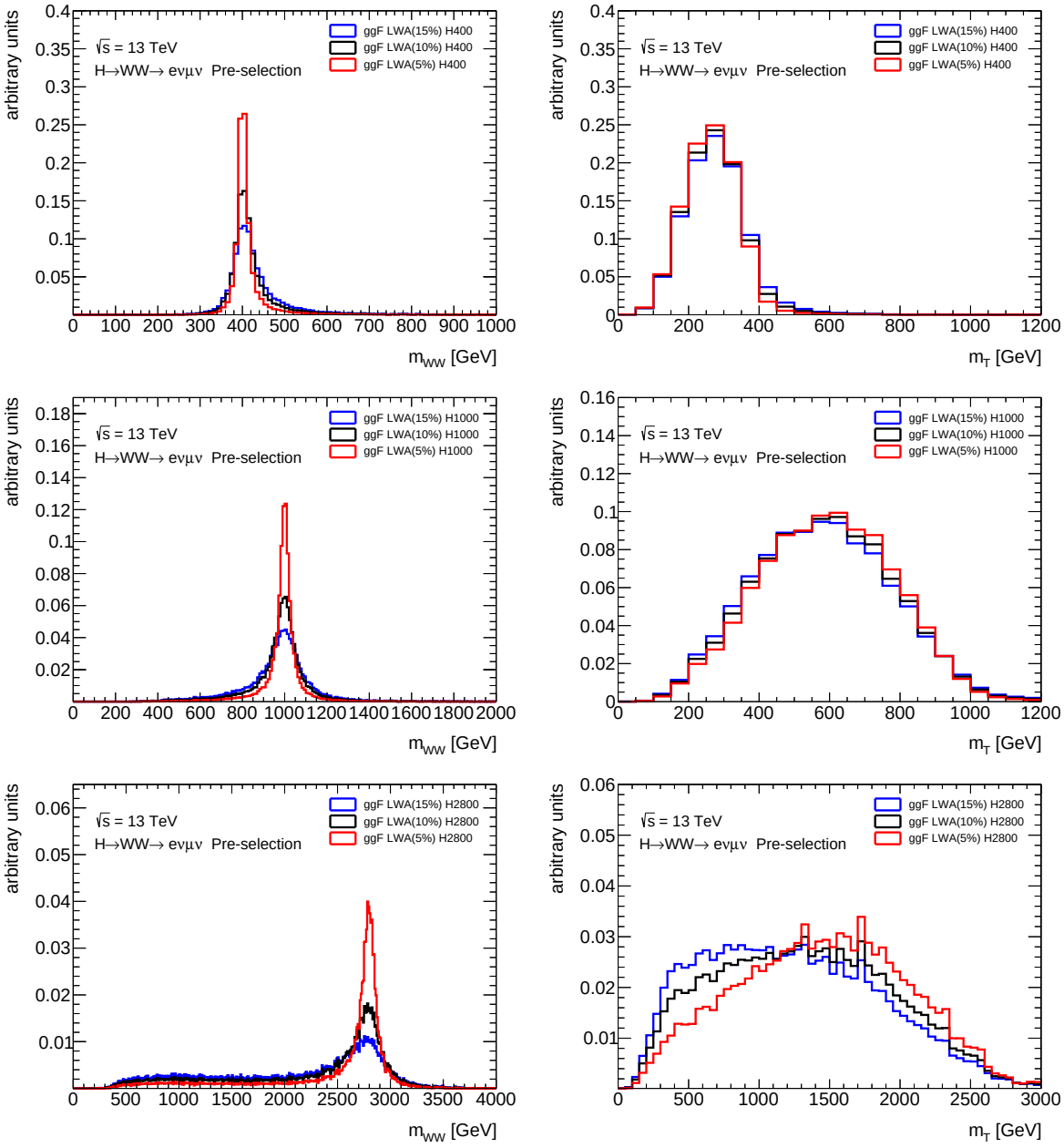

Figure 4.17: The distribution of m_{WW} (left) and m_{T} (right) of the LWA signal interpretation with m_H values of 400 (top), 1000 (middle), and 2800 GeV (bottom) and a line width of 15% (blue), 10% (black), and 5% (red) of m_H. The distributions are normalised to have an integral of one.

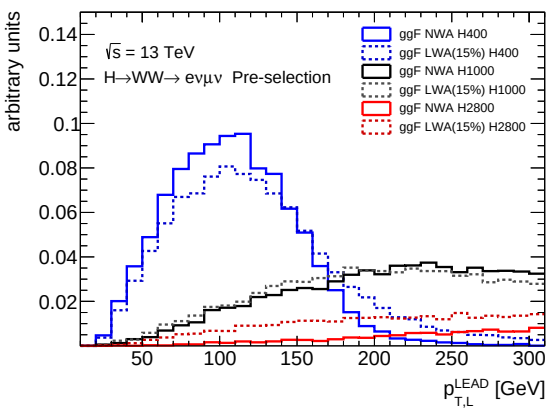

(a) $p_{\mathrm{T,L}}^{\mathrm{LEAD}}$

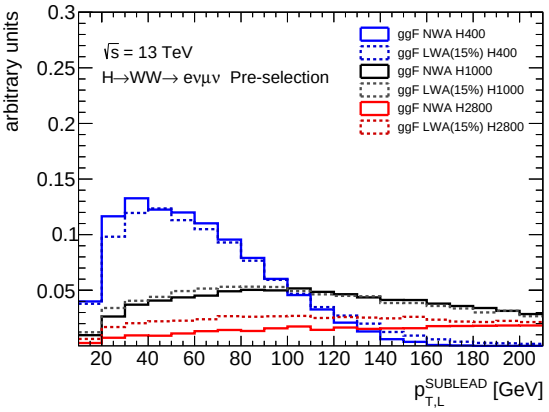

(b) $p_{\mathrm{T,L}}^{\mathrm{SUBLEAD}}$

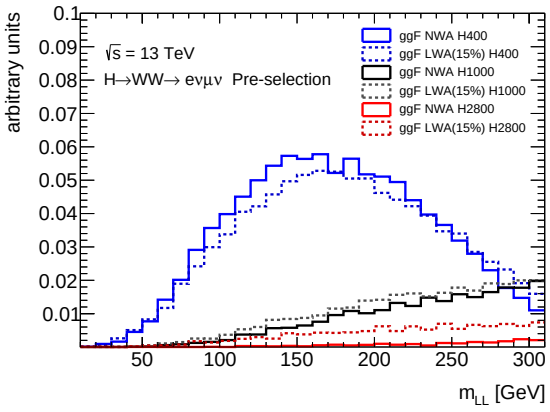

(c) m_{LL}

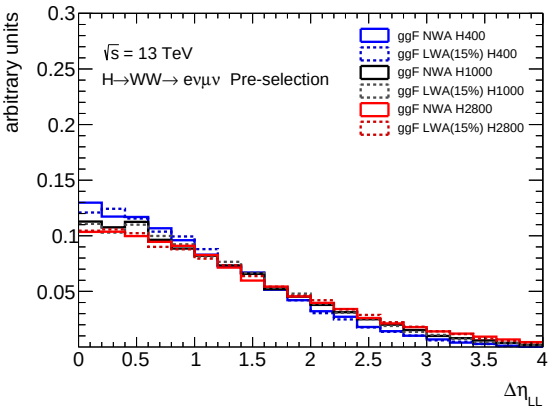

(d) $\Delta\eta_{\mathrm{LL}}$

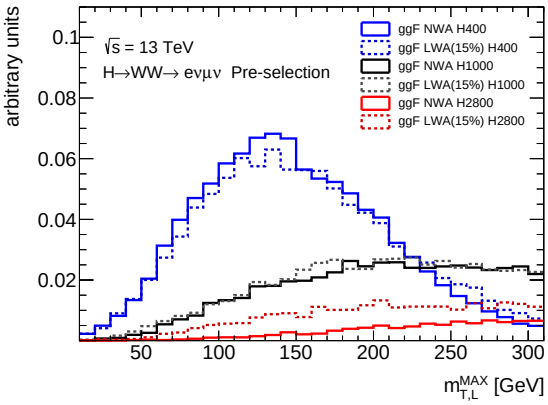

(e) $m_{\mathrm{T,L}}^{\mathrm{MAX}}$

Figure 4.18: The distribution of $p_{\mathrm{T,L}}^{\mathrm{LEAD}}$ (a), $p_{\mathrm{T,L}}^{\mathrm{SUBLEAD}}$ (b), m_{LL} (c), $\Delta\eta_{\mathrm{LL}}$ (d), and $m_{\mathrm{T,L}}^{\mathrm{MAX}}$ (e) for the NWA ggF (solid line) and LWA ggF (dashed line) signal interpretation at m_H values of 400 (blue), 1000 (black), and 2800 GeV (red). The distributions are normalised to have an integral of one.

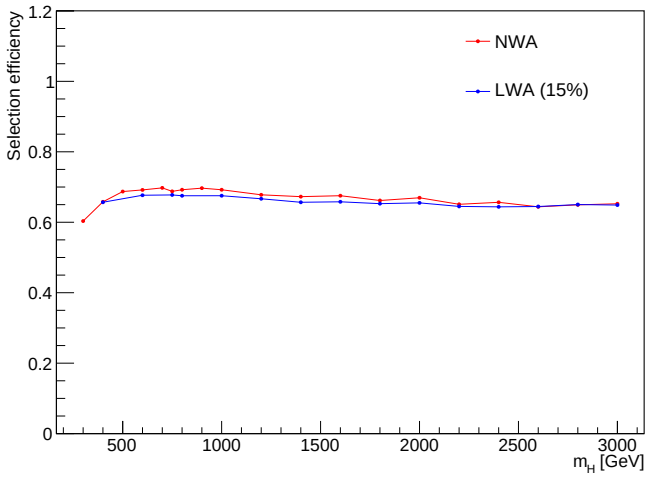

Figure 4.19: Selection efficiency of the signal requirements after the pre-selection for the NWA (red) and LWA (blue) signal interpretation, as a function of m_H.

The double ratio described in Eq. 4.11 is evaluated for several masses of the high-mass boson and used to determine functional descriptions for any value of m_H of the VBF 1J and VBF 2J correction factors [87]. The resulting equations for $f_{\text{VBF 1J}}$ and $f_{\text{VBF 2J}}$ are

$$f_{\text{VBF 1J}} = 1.816 \cdot 10^{-8} \frac{m_H^2}{\text{GeV}^2} - 1.344 \cdot 10^{-4} \frac{m_H}{\text{GeV}} + 1.014 \tag{4.12}$$

and

$$f_{\text{VBF 2J}} = 6.032 \cdot 10^{-8} \frac{m_H^2}{\text{GeV}^2} - 3.611 \cdot 10^{-4} \frac{m_H}{\text{GeV}} + 1.539. \tag{4.13}$$

Selection rates for the NWA interpretation of the ggF signal in the VBF 1J and VBF 2J SR are scaled by the correction factors obtained from Eqs. 4.12 and 4.13, without altering the overall number of events selected in all three signal regions.

Interference Effects

For the results of the Run-I high-mass $H \to W^+W^- \to \ell^+\nu\ell^-\bar{\nu}$ analysis [8], interference effects of the non-resonant WW spectrum with the heavy Higgs boson with non-negligible line width are taken into account. The impact of this interference was shown to be significant on the shape of the m_{T} distribution, as well as the total cross section. Interference effects for the NWA interpretation are shown to be negligible and thus are not considered in the analysis.
For the LWA interpretation, interference effects as discussed in Ref. [8] are expected to have a similar impact. Furthermore, the interference between the hypothesised heavy Higgs boson and the SM Higgs boson is shown to have a significant impact on the line shape of the high-mass Higgs boson in the ggF [98] and VBF [99] production mode. The interference

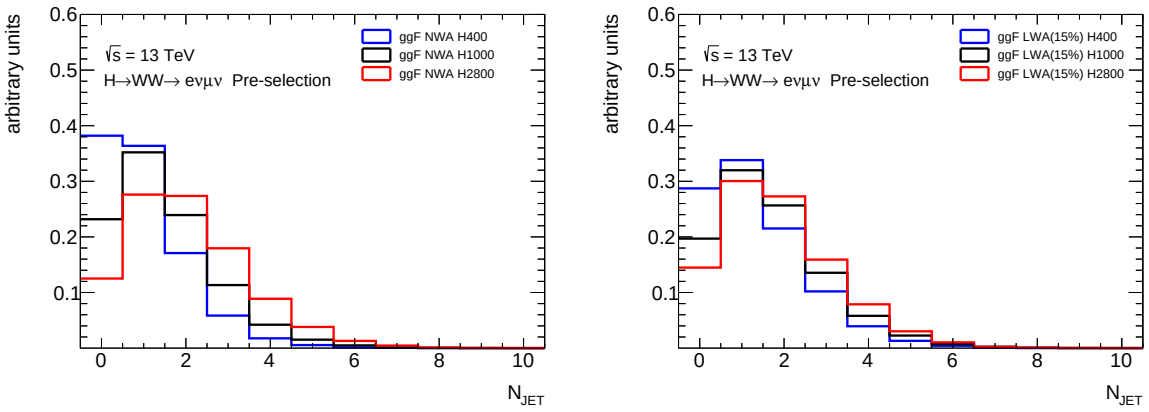

(a) NWA ggF (b) LWA ggF

Figure 4.20: The distribution of the number of reconstructed jets in the event for the NWA (a) and LWA (b) ggF signal interpretation at m_H values of 400 (blue), 1000 (black), and 2800 GeV (red). The distributions are normalised to have an integral of one.

effects are demonstrated to show an opposite behaviour to the impact from interference with the non-resonant WW background, leading to cancellation effects between the two sources of interference. This behaviour necessitates thorough studies on the overall impact of interference effects on the considered signal interpretations.
In depth studies regarding interference effects on the heavy Higgs signal are planned for the further progression of the Run-II high-mass $H \to W^+W^- \to \ell^+\nu\ell^-\bar{\nu}$ analysis. For the preliminary results presented in Section 4.7, the impact of interference effects on the LWA signal are neglected and are assumed to be negligible for the NWA interpretation, following the results of the Run-I analysis [8].

4.4.2 Impact of Jet Multiplicity on the ggF Signal Categorisation

The presence of energetic jets, in addition to the charged leptons and neutrinos, is a distinct characteristic of the VBF production mode, but it only occurs through additional QCD parton emission from the intital state in the case of the ggF topology (see Section 2.3.1). The SM Higgs analysis for the $H \to W^+W^- \to \ell^+\nu\ell^-\bar{\nu}$ channel [95] predominantly considers the decay with up to one additional jet for the ggF production, while the topology with two or more jets is mostly sensitive to the VBF channel. For the Run-I high-mass $H \to W^+W^- \to \ell^+\nu\ell^-\bar{\nu}$ analysis [8], the same approach was adopted and continued for the first results with Run-II data [100] (*jet-exclusive* analysis).
Figure 4.20 shows the number of reconstructed jets in the event for the NWA and LWA ggF signal, after pre-selection requirements are applied. For lower masses, the majority of events fall into the zero and one additional jet category. With increasing mass of the heavy boson, the jet multiplicity distribution shifts to higher values. A measure for the hadronic recoil of additional jets in the event is the transverse momentum of the heavy

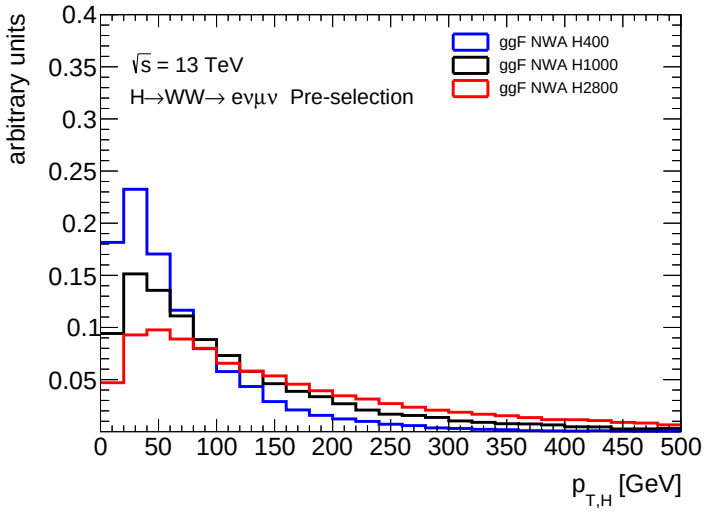

Figure 4.21: The distribution of $p_{\mathrm{T},H}$ for the NWA ggF signal interpretation at m_H values of 400 (blue), 1000 (black), and 2800 GeV (red). The distributions are normalised to have an integral of one.

boson ($p_{\mathrm{T},H}$) produced in the ggF mode. Figure 4.21 shows the distribution of $p_{\mathrm{T},H}$ for the NWA ggF signal, on the level of event generation after pre-selection requirements are applied. The $p_{\mathrm{T},H}$ distribution shifts to higher values with increasing mass of the hypothesised heavy boson, which indicates that the hadronic activity in the event increases as well. The behaviour of the number of jets in ggF produced events in the context of the SM Higgs production has been studied in Ref. [101], where an increase in jet multiplicity is shown to occur for high values in the $p_{\mathrm{T},H}$ spectrum. This is consistent with the behaviour of the NWA ggF signal shown in Figure 4.20a and 4.21.

The behaviour of the jet multiplicity with increasing values of m_H leads to a decline in sensitivity to the ggF production mode with the Run-I analysis strategy. This is due to the VBF targeted selection for events with at least two jets, which are similar to the VBF requirements described in Section 4.2.2. Figure 4.22 shows the comparison of exclusion limits[3] on the cross section times branching ratio ($\sigma \times BR(H \to WW)$) of the decay to two W bosons (see Section 4.6) for the NWA and LWA ggF signal, between the *jet-exclusive* analysis strategy and a selection inclusive in jet multiplicity (*jet-inclusive*) with a separate, VBF targeted region for events with at least two jets. Events with two or more jets that do not fulfil the VBF requirements are omitted by the *jet-exclusive* analysis. This leads to a significant decrease in exclusion power compared to a selection inclusive in the number of jets, indicating a significantly lower sensitivity to the ggF produced signal.
The loss of sensitivity motivates the adoption of the *jet-inclusive* selection strategy for the

[3]Previous preliminary results considered masses down to 600 GeV, whereas the results presented in this thesis are extended to 300 GeV for the NWA, and 400 GeV for the LWA interpretation.

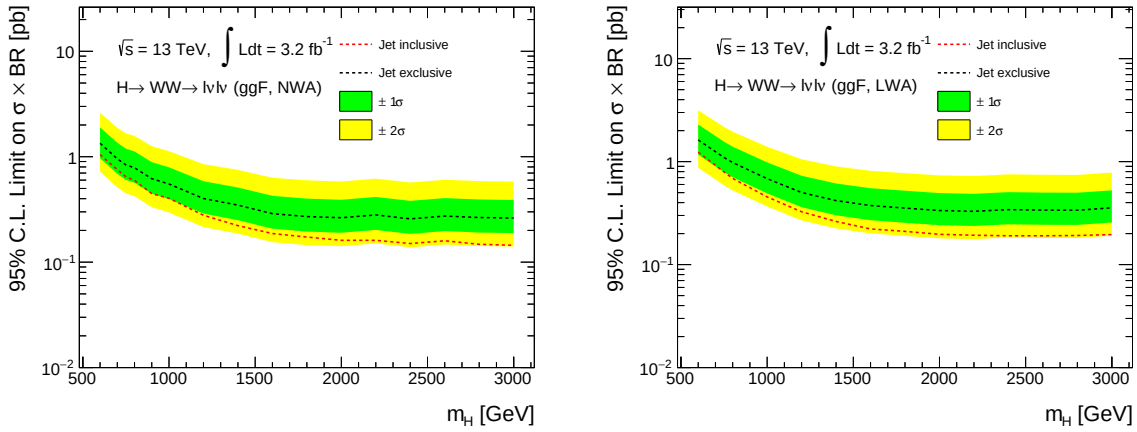

(a) NWA ggF

(b) LWA ggF

Figure 4.22: Comparison of exclusion limits between the *jet-exclusive* (black) and *jet-inclusive* (red) analysis strategy for the NWA (a) and LWA (b) ggF signal interpretation. In the likelihood fit, only statistical uncertainties are considered. For the respective signal interpretations, high-mass bosons with a value of $\sigma \times BR(H \rightarrow WW)$ higher than the limit can be excluded at 95% C.L., at a given value of m_H.

ggF production mode. For the VBF signal, however, the sensitivity is decreased compared to the *jet-exclusive* case, as shown in Figure 4.24a. VBF signal events with only one reconstructed jet are evaluated against a highly increased number of background events, due to the combination of events with no jet, one jet, and at least two jets, where the VBF requirements are not fulfilled.
Events, for which only one jet of the VBF topology is reconstructed, show characteristic differences in the direction in η of the jet and the angular separation between the jet and the two charged leptons, in comparison to the ggF production mode. Figure 4.23 shows the distribution of the variables, which are used in Section 4.2.2 to discriminate the VBF 1J category, for the ggF and VBF NWA signal with $m_H = 1000$ GeV. The clear separation between the ggF and VBF production mode motivates the dedicated selection on VBF events with one jet to recover the loss in sensitivity. Figure 4.24b shows the exclusion limit comparison for the VBF NWA signal, between the *jet-exclusive* analysis and the full selection described in Section 4.2.2. The inclusion of a dedicated VBF 1J category recovers and even increases the sensitivity to the VBF production mode.
In addition to the improvements to the signal sensitivity, the choice of a *jet-inclusive* selection for the ggF production mode strongly reduces theoretical uncertainties related to jet multiplicity migration, which have been found to have a large impact on the ggF signal when a strategy with categorisation according to the number of jets is followed [95]. The impact from this uncertainty is further discussed in Section 4.5.3.

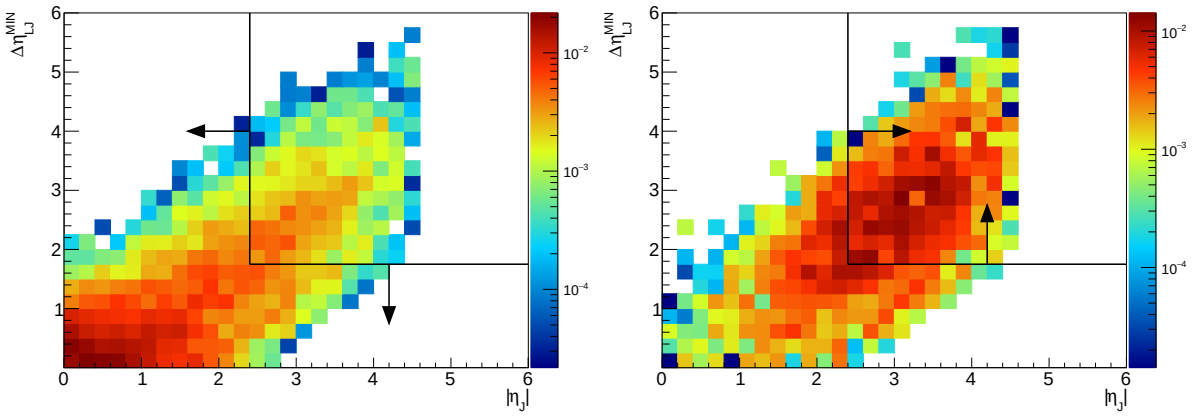

(a) ggF (b) VBF

Figure 4.23: The two dimensional distributions of $|\eta_J|$ and $\Delta\eta_{LJ}^{MIN}$ for the ggF (a) and VBF (b) production mode for $m_H = 1000$ GeV. The arrows indicate the kinematic regions selected by the VBF 1J categorisation. The distributions are normalised to have an integral of one.

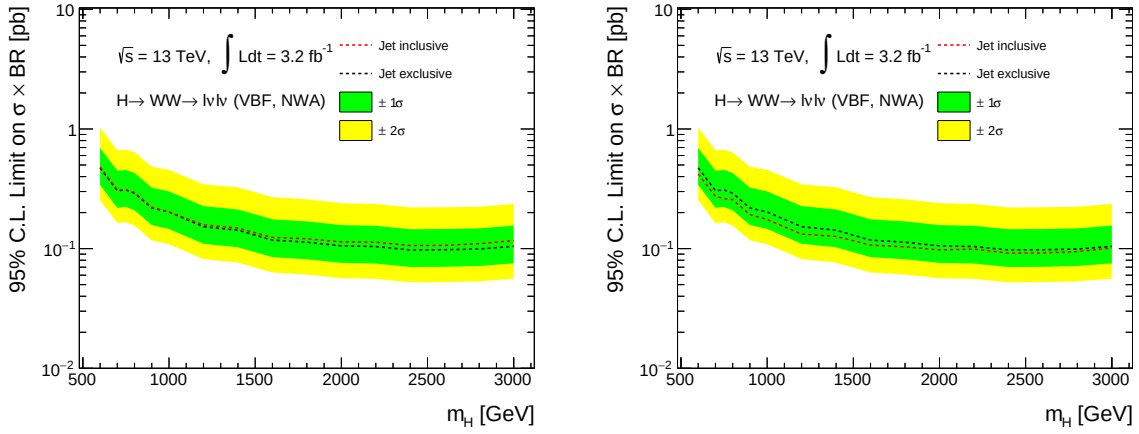

(a) *jet-inclusive* + VBF 2J (b) *jet-inclusive* + VBF 1J + VBF 2J

Figure 4.24: Comparison of exclusion limits for the NWA VBF signal interpretation between the *jet-exclusive* (black) and *jet-inclusive* (red) analysis strategy with additional selection on VBF 2J (a) and VBF 1J + VBF 2J (b). In the likelihood fit, only statistical uncertainties are considered. For the respective signal interpretations, high-mass bosons with a value of $\sigma \times BR(H \to WW)$ higher than the limit can be excluded at 95% C.L., at a given value of m_H.

4.5 Systematic Uncertainties

In this section, the systematic uncertainties on the signal and background descriptions, which are considered in the high-mass $H \to W^+W^- \to \ell^+\nu\ell^-\bar{\nu}$ analysis, are presented. This includes uncertainties on the experimental methods for data acquisition, calibration, and correction as well as theoretical uncertainties on the modelling of signal and background processes. The impact on signal and background contributions in terms of the number of selected events and kinematic shapes is estimated by variation of statistically independent parameters related to the experimental and theoretical uncertainty components. For the normalisation of backgrounds constrained by data control regions, the uncertainty arises from the extrapolation from control to signal regions, rather than just the impact on the number of events from MC simulation in the signal regions.

4.5.1 Experimental Uncertainties

Systematic uncertainties on the experimental data processing methods are evaluated for the dominant background sources from top quark and WW decays and the minor background contributions from $Z+\text{jets}$ and VV, as well as for the NWA ggF and VBF and LWA ggF signal interpretation at each mass point considered. For the data-driven estimate of the $W+\text{jets}$ background, dedicated experimental uncertainties are evaluated from systematic variations on the fake factors.

Integrated Luminosity and Pileup Reweighting

The integrated luminosity used for normalisation of simulated events is assigned with an uncertainty of 2.9%, which is derived from a preliminary calibration of the luminosity scale using x-y beam-separation scans performed in 2015 and 2016, following the methodology in Refs. [102] and [103]. One systematic parameter is assigned to the uncertainty on the PRW procedure, described in Section 4.2.2. The impact of this uncertainty is estimated by variation of the data scale factor to $\frac{1}{1.09}$ and $\frac{1}{1.23}$ [85].

Leptons

Experimental uncertainty sources related to muons are considered for the muon momentum calibration and the efficiency corrections on muon identification, isolation, and trigger selection [39]. The impact of systematic uncertainties coming from the muon calibration is estimated by variation of three systematic parameters related to the momentum resolution smearing and the momentum scale correction, combining uncertainties on the choice of selection requirements and the template fit parameterisation. Two variation parameter are used for the muon identification, isolation, and trigger efficiency correction, respectively. One represents the uncertainty due to the limited statistical precision and the second combines uncertainties on the background estimate, uncertainties from particle level comparisons, and uncertainties due to the choice of selection criteria, related to the respective efficiency measurements.

Systematic uncertainties associated to electrons are taken into account for the electron calibration [43] and electron efficiency corrections on reconstruction, identification, isolation, and trigger selection [42]. Electron calibration is represented by one parameter for the electron energy scale and resolution, respectively, which consists of uncertainties related to the choice of selection criteria, the proton-proton beam configuration, the detector description, and the statistics of samples as well as the experimental procedures used for data-driven corrections. For each efficiency correction component, one variation parameter is used, which combines uncertainties on the definition of templates for background estimation, statistical uncertainties, and the choice of selection criteria of the efficiency measurements.

Jets

For the uncertainties related to jets, systematic components from the jet energy scale (JES) and resolution (JER) calibration [47], and the JVT selection efficiency correction [76, 77] are considered. A set of 19 systematic parameters is associated to the jet energy scale, which covers components from in-situ corrections, forward jet calibration, behaviour of high p_{T} jets, pileup effects, jet topology, and flavour composition and response. One parameter is used for the jet energy resolution, which reflects the variation of the jet energy smearing. For the JVT correction, one systematic parameter represents uncertainties related to the statistical precision and choice of MC generator in the measurements and residual contamination from pileup jets. Systematic parameters are considered for the b-tagging calibration, representing uncertainties on the b-jet [80] and c-jet [81] efficiency and light-flavour jet mistag efficiency [81] measurements, respectively.

Missing Transverse Energy

The impact of systematic variations affecting the four-momentum properties of electrons, muons, and jets is taken into account for the evaluation of $E_{\mathrm{T}}^{\mathrm{MISS}}$. In addition, three systematic parameters associated to the resolution and the scale of the TST measurement [51] are used to estimate the impact from uncertainties related to the soft term component of the $E_{\mathrm{T}}^{\mathrm{MISS}}$. The uncertainties are quantified with the axis direction of the vector sum of transverse momenta of all objects associated to the hard scatter interaction ($\boldsymbol{p}_{\mathrm{T}}^{\mathrm{HARD}}$), which provides a measure of the high-p_{T} activity in the event. Scale variation effects are mostly present longitudinal to the $\boldsymbol{p}_{\mathrm{T}}^{\mathrm{HARD}}$ axis, while shifts in the resolution appear both in longitudinal and transverse components. The uncertainties from comparison of different MC generators and on the $E_{\mathrm{T}}^{\mathrm{MISS}}$ reconstruction under the aspect of alternative azimuthal detector material distributions are considered for the full evaluation.

Uncertainties on the Backgrounds from Monte Carlo Simulation

All experimental uncertainty sources are evaluated by up and down variation of the respective parameters and processing of the full analysis chain with the varied component. This results in alteration of the signal and background predictions in terms of the shape of m_{T} as well as the number of selected events. All components are taken into account separately

Source	SR_{ggF}	CR^{Top}_{ggF}	CR^{WW}_{ggF}	$SR_{VBF\ 1J}$	$SR_{VBF\ 2J}$	CR^{Top}_{VBF}	$CR^{WW}_{VBF\ 1J}$
$\Delta_{\text{B-TAG}}$	16.7	4.5	17.0	6.2	13.5	3.2	7.0
$\Delta_{e\ \text{P4}}$	< 1.0	< 1.0	< 1.0	< 1.0	< 1.0	< 1.0	< 1.0
$\Delta_{e\ \text{SF}}$	1.1	1.1	1.2	< 1.0	1.2	1.5	1.2
Δ_{JET}	4.6	1.7	5.0	9.8	12.1	9.0	9.5
Δ_{JVT}	2.1	2.6	2.1	< 1.0	2.2	3.2	< 1.0
$\Delta_{E_{\text{T}}^{\text{MISS}}}$	< 1.0	< 1.0	< 1.0	< 1.0	< 1.0	< 1.0	< 1.0
$\Delta_{\mu\ \text{P4}}$	< 1.0	< 1.0	< 1.0	< 1.0	< 1.0	< 1.0	< 1.0
$\Delta_{\mu\ \text{SF}}$	1.3	1.4	1.2	1.7	< 1.0	1.5	1.2
Δ_{PU}	< 1.0	< 1.0	< 1.0	< 1.0	< 1.0	< 1.0	< 1.0

Table 4.5: The relative impact of experimental uncertainties on the number of top quark background events in the signal and control regions, in percentage of the nominal values. The uncertainties are grouped according to the systematic components described in the text.

as uncertainties on the signal and background contributions in the statistical evaluation described in Section 4.6.

Tables 4.5-4.8 show the relative impact on the number of events in each signal and control region of the experimental systematic components discussed in this section, for the top quark, WW, VV, and $Z+$jets background, respectively. The systematic parameters are grouped according to their respective source, by taking the sum in quadrature of the maximum impact for each component. Grouped components for the lepton calibration ($\Delta_{e\ \text{P4}}$ and $\Delta_{\mu\ \text{P4}}$) and efficiency corrections ($\Delta_{e\ \text{SF}}$ and $\Delta_{\mu\ \text{SF}}$), the JES and JER calibration (Δ_{JET}), the JVT correction (Δ_{JVT}), the $E_{\text{T}}^{\text{MISS}}$ soft term description ($\Delta_{E_{\text{T}}^{\text{MISS}}}$), the b-jet identification ($\Delta_{\text{B-TAG}}$), and the PRW procedure (Δ_{PU}) are shown.

The top quark background is predominantly affected by systematic uncertainties on the JES and JER, as well as components coming from the b-jet identification. The latter are particularly significant for the regions where a veto is applied on the b-jets from the top quark decays. The jet related components are also the main source of experimental uncertainty for the WW background, for which the highest impact is found in the VBF regions. Large uncertainties from the b-tagging are present for the top quark control regions, where the negligible WW contribution arises from misidentification of a light quark jet as b-jet.

The minor background contributions from VV and $Z+$jets show large uncertainties on the jet and b-tagging components as well. Estimation of the experimental uncertainties for these highly suppressed backgrounds suffers from limited statistical precision of the MC simulated samples, in particular in the VBF specific regions. Table 4.9 shows the relative uncertainty on the number of selected events in the signal and control regions, due to the limited statistics in MC generated events. Despite the high statistical and systematic uncertainties, the impact on the final results is small compared to the top quark and WW

Source	SR_{ggF}	CR^{Top}_{ggF}	CR^{WW}_{ggF}	$SR_{VBF\ 1J}$	$SR_{VBF\ 2J}$	CR^{Top}_{VBF}	$CR^{WW}_{VBF\ 1J}$
$\Delta_{\text{B-TAG}}$	1.7	22.1	1.5	< 1.0	3.4	21.8	< 1.0
$\Delta_{e\ \text{P4}}$	< 1.0	< 1.0	< 1.0	< 1.0	< 1.0	< 1.0	< 1.0
$\Delta_{e\ \text{SF}}$	1.1	1.2	1.2	< 1.0	1.2	1.5	1.3
Δ_{JET}	1.3	5.1	1.1	15.7	22.6	16.6	18.3
Δ_{JVT}	< 1.0	2.6	< 1.0	< 1.0	1.8	2.7	< 1.0
$\Delta_{E_{\text{T}}^{\text{MISS}}}$	< 1.0	< 1.0	< 1.0	< 1.0	< 1.0	< 1.0	< 1.0
$\Delta_{\mu\ \text{P4}}$	< 1.0	< 1.0	< 1.0	< 1.0	< 1.0	< 1.0	< 1.0
$\Delta_{\mu\ \text{SF}}$	1.2	1.4	< 1.0	1.7	1.6	1.7	1.5
Δ_{PU}	< 1.0	< 1.0	< 1.0	< 1.0	2.9	2.0	2.6

Table 4.6: The relative impact of experimental uncertainties on the number of WW background events in the signal and control regions, in percentage of the nominal values. The uncertainties are grouped according to the systematic components described in the text.

backgrounds. The contribution from $Z+\text{jets}$ and VV to the background composition is either negligible (top quark control regions) or minor compared to the dominant processes. Furthermore, the $Z+\text{jets}$ background is predominantly located at the lower end of the m_{T} spectrum, which is less relevant for the final statistical evaluation of the high-mass signal sensitivity.

Uncertainties on the Signal

The impact of experimental uncertainties on a heavy scalar boson with masses 400, 1000, and 2800 GeV is shown in Table 4.10 and 4.11 for the NWA and LWA interpretation, respectively. For the VBF specific regions the JES and JER components are the dominant uncertainty source in particular for the ggF signal. The systematic components show no strong dependency on the mass of the heavy boson, except for the lepton efficiency uncertainties on ggF and VBF and the uncertainties related to JES and JER on the ggF signal. For the lepton efficiency components the impact increases with increasing signal mass, due to the shift to higher values in the respective lepton p_{T} spectra, as shown in Figure 4.15. Electrons and muons with very high transverse momenta are assigned with larger uncertainties by the respective efficiency studies [39, 42], due to the statistical limitations in data of the tag-and-probe method at high values of p_{T} of the probe lepton.

Uncertainties on the $W+\text{jets}$ Background

Experimental uncertainties on the $W+\text{jets}$ background are estimated by variation of the fake factors used in the data-driven method [95, 96]. The impact on the full $W+\text{jets}$ estimation is evaluated separately for the electron and muon components of the fake factors. One systematic parameter is considered for the uncertainty on the theory prediction of the subtracted background components in the fake factor estimation. The background

Source	SR_{ggF}	CR^{Top}_{ggF}	CR^{WW}_{ggF}	$SR_{VBF\ 1J}$	$SR_{VBF\ 2J}$	CR^{Top}_{VBF}	$CR^{WW}_{VBF\ 1J}$
$\Delta_{\text{B-TAG}}$	2.2	16.1	1.8	1.8	3.9	21.1	< 1.0
$\Delta_{e\ \text{P4}}$	< 1.0	1.2	< 1.0	2.3	< 1.0	< 1.0	< 1.0
$\Delta_{e\ \text{SF}}$	1.3	1.4	1.6	1.1	1.7	1.7	1.5
Δ_{JET}	1.2	4.4	2.0	17.0	19.7	91.1	21.3
Δ_{JVT}	1.3	2.6	1.2	< 1.0	2.3	2.4	< 1.0
$\Delta_{E_{\text{T}}^{\text{MISS}}}$	1.1	1.8	< 1.0	1.6	4.1	< 1.0	< 1.0
$\Delta_{\mu\ \text{P4}}$	< 1.0	1.6	< 1.0	2.0	2.5	< 1.0	< 1.0
$\Delta_{\mu\ \text{SF}}$	1.1	2.4	< 1.0	< 1.0	< 1.0	8.6	< 1.0
Δ_{PU}	< 1.0	< 1.0	< 1.0	3.7	4.3	1.6	4.9

Table 4.7: The relative impact of experimental uncertainties on the number of VV background events in the signal and control regions, in percentage of the nominal values. The uncertainties are grouped according to the systematic components described in the text.

composition in the evaluation predominantly consists of $W+$jets and $Z+$jets processes, for which a flat 20% variation on the normalisation is used as uncertainty. This is motivated by the cross section uncertainties on the $V+$ jets processes as well as lepton modelling uncertainties in MC simulation. The uncertainty on the difference in flavour composition of the jets, between the dijet sample used for the fake factor estimation and the background contribution expected from $W+$ jets decays, is considered with an additional systematic component. The impact is derived from comparison of fake factors evaluated with the dijet sample with fake factors obtained from a separate $Z+$ jets data sample, which is expected to have a similar composition of jet flavours as $W+$ jets decays. In addition to the difference between these two evaluations, an extrapolation uncertainty of 20% from the $Z+$ jets to $W+$ jets process is taken into account for the uncertainty on the jet flavour composition. Finally the impact from the limited statistical precision of the fake factor evaluation is considered as a separate systematic component.
Table 4.12 shows the relative impact on the $W+$jets background contribution of the systematic fake factor variations, grouped according to the background subtraction ($\Delta^{\text{W+JETS}}_{\text{BKG SUBTR.}}$), jet flavour composition ($\Delta^{\text{W+JETS}}_{\text{COMP.}}$), and limited statistics ($\Delta^{\text{W+JETS}}_{\text{STAT.}}$) components. The largest impact comes from the uncertainty on the jet flavour composition, while the uncertainty from the limited statistics of the fake factor estimation is negligible. The uncertainty due to the limited statistical precision of the $W+$ jets control sample in the signal and control regions is shown in Table 4.9.

Source	SR_{ggF}	CR^{Top}_{ggF}	CR^{WW}_{ggF}	$SR_{VBF\ 1J}$	$SR_{VBF\ 2J}$	CR^{Top}_{VBF}	$CR^{WW}_{VBF\ 1J}$
$\Delta_{\text{B-TAG}}$	1.8	9.8	1.6	< 1.0	2.2	19.1	3.9
$\Delta_{e\ \text{P4}}$	1.2	15.3	< 1.0	< 1.0	< 1.0	< 1.0	9.9
$\Delta_{e\ \text{SF}}$	< 1.0	< 1.0	1.3	< 1.0	1.4	2.2	1.9
Δ_{JET}	5.1	46.6	3.7	46.9	58.6	46.7	23.0
Δ_{JVT}	< 1.0	2.0	< 1.0	< 1.0	< 1.0	1.4	< 1.0
$\Delta_{E_{\text{T}}^{\text{MISS}}}$	8.2	3.5	< 1.0	< 1.0	8.5	< 1.0	< 1.0
$\Delta_{\mu\ \text{P4}}$	4.7	2.4	< 1.0	< 1.0	< 1.0	4.5	4.0
$\Delta_{\mu\ \text{SF}}$	< 1.0	2.0	< 1.0	3.3	< 1.0	< 1.0	< 1.0
Δ_{PU}	< 1.0	6.6	10.7	6.4	11.5	7.7	12.6

Table 4.8: The relative impact of experimental uncertainties on the number of Z + jets background events in the signal and control regions, in percentage of the nominal values. The uncertainties are grouped according to the systematic components described in the text.

Background	SR_{ggF}	CR^{Top}_{ggF}	CR^{WW}_{ggF}	$SR_{VBF\ 1J}$	$SR_{VBF\ 2J}$	CR^{Top}_{VBF}	$CR^{WW}_{VBF\ 1J}$
Top	< 1.0	< 1.0	< 1.0	2.4	2.5	< 1.0	3.7
WW	< 1.0	2.3	1.5	2.6	4.8	6.3	3.6
VV	2.8	8.2	4.6	14.2	14.1	15.9	13.2
Z + jets	11.4	21.4	41.1	33.2	40.4	19.3	26.3
W + jets	3.2	5.0	6.1	11.1	24.7	7.7	13.1

Table 4.9: The relative statistical uncertainties on the prediction of the background components in the signal and control regions, in percentage of the nominal values. The values represent the uncertainty on the MC simulated statistics except for the W + jets background, where the combined statistical uncertainty from data and MC simulation in the W + jets control sample is considered.

	NWA H400 ggF			NWA H400 VBF		
Source	SR_{ggF}	$SR_{VBF\ 1J}$	$SR_{VBF\ 2J}$	SR_{ggF}	$SR_{VBF\ 1J}$	$SR_{VBF\ 2J}$
$\Delta_{\text{B-TAG}}$	1.9	$<$ 1.0	2.6	2.3	$<$ 1.0	1.7
$\Delta_{e\ \text{P4}}$	$<$ 1.0	$<$ 1.0	$<$ 1.0	$<$ 1.0	$<$ 1.0	$<$ 1.0
$\Delta_{e\ \text{SF}}$	1.2	1.1	1.1	1.2	1.1	1.2
Δ_{JET}	1.4	5.5	14.7	3.6	6.3	4.1
Δ_{JVT}	1.3	$<$ 1.0	1.3	1.1	$<$ 1.0	$<$ 1.0
$\Delta_{E_{\text{T}}^{\text{MISS}}}$	$<$ 1.0	$<$ 1.0	$<$ 1.0	$<$ 1.0	$<$ 1.0	$<$ 1.0
$\Delta_{\mu\ \text{P4}}$	$<$ 1.0	$<$ 1.0	$<$ 1.0	$<$ 1.0	$<$ 1.0	$<$ 1.0
$\Delta_{\mu\ \text{SF}}$	1.5	2.1	1.1	1.2	2.5	1.3
Δ_{PU}	$<$ 1.0	1.2	$<$ 1.0	1.7	1.5	$<$ 1.0
	NWA H1000 ggF			NWA H1000 VBF		
Source	SR_{ggF}	$SR_{VBF\ 1J}$	$SR_{VBF\ 2J}$	SR_{ggF}	$SR_{VBF\ 1J}$	$SR_{VBF\ 2J}$
$\Delta_{\text{B-TAG}}$	2.7	$<$ 1.0	3.0	2.0	$<$ 1.0	1.5
$\Delta_{e\ \text{P4}}$	$<$ 1.0	$<$ 1.0	$<$ 1.0	$<$ 1.0	$<$ 1.0	$<$ 1.0
$\Delta_{e\ \text{SF}}$	2.0	2.0	2.0	2.0	2.0	2.0
Δ_{JET}	1.5	5.6	11.1	5.2	6.9	5.9
Δ_{JVT}	1.6	$<$ 1.0	1.5	$<$ 1.0	$<$ 1.0	$<$ 1.0
$\Delta_{E_{\text{T}}^{\text{MISS}}}$	$<$ 1.0	$<$ 1.0	$<$ 1.0	$<$ 1.0	$<$ 1.0	$<$ 1.0
$\Delta_{\mu\ \text{P4}}$	$<$ 1.0	$<$ 1.0	$<$ 1.0	$<$ 1.0	$<$ 1.0	$<$ 1.0
$\Delta_{\mu\ \text{SF}}$	2.4	3.2	3.5	3.0	2.6	2.7
Δ_{PU}	$<$ 1.0	$<$ 1.0	$<$ 1.0	1.2	$<$ 1.0	$<$ 1.0
	NWA H2800 ggF			NWA H2800 VBF		
Source	SR_{ggF}	$SR_{VBF\ 1J}$	$SR_{VBF\ 2J}$	SR_{ggF}	$SR_{VBF\ 1J}$	$SR_{VBF\ 2J}$
$\Delta_{\text{B-TAG}}$	3.7	$<$ 1.0	3.3	1.3	$<$ 1.0	$<$ 1.0
$\Delta_{e\ \text{P4}}$	$<$ 1.0	$<$ 1.0	$<$ 1.0	$<$ 1.0	$<$ 1.0	$<$ 1.0
$\Delta_{e\ \text{SF}}$	2.3	2.3	2.3	2.3	2.4	2.3
Δ_{JET}	1.1	4.3	8.6	6.3	4.3	6.5
Δ_{JVT}	1.9	$<$ 1.0	1.6	$<$ 1.0	$<$ 1.0	$<$ 1.0
$\Delta_{E_{\text{T}}^{\text{MISS}}}$	$<$ 1.0	$<$ 1.0	$<$ 1.0	$<$ 1.0	$<$ 1.0	$<$ 1.0
$\Delta_{\mu\ \text{P4}}$	$<$ 1.0	$<$ 1.0	$<$ 1.0	$<$ 1.0	$<$ 1.0	$<$ 1.0
$\Delta_{\mu\ \text{SF}}$	4.2	4.4	4.2	4.3	4.2	4.8
Δ_{PU}	$<$ 1.0	$<$ 1.0	$<$ 1.0	$<$ 1.0	1.4	1.6

Table 4.10: The relative impact of experimental uncertainties on the number of ggF and VBF signal events in the signal regions for the NWA interpretation of a high-mass scalar boson with a mass of 400, 1000, and 2800 GeV, in percentage of the nominal values. The uncertainties are grouped according to the systematic components described in the text.

	LWA H400 ggF		
Source	SR_{ggF}	$SR_{VBF\ 1J}$	$SR_{VBF\ 2J}$
$\Delta_{\text{B-TAG}}$	2.5	< 1.0	2.8
$\Delta_{e\ \text{P4}}$	< 1.0	< 1.0	< 1.0
$\Delta_{e\ \text{SF}}$	1.3	1.2	1.3
Δ_{JET}	1.4	6.4	10.5
Δ_{JVT}	1.4	< 1.0	1.4
$\Delta_{E_{\text{T}}^{\text{MISS}}}$	< 1.0	< 1.0	< 1.0
$\Delta_{\mu\ \text{P4}}$	< 1.0	< 1.0	< 1.0
$\Delta_{\mu\ \text{SF}}$	1.6	1.8	2.2
Δ_{PU}	< 1.0	< 1.0	< 1.0
	LWA H1000 ggF		
Source	SR_{ggF}	$SR_{VBF\ 1J}$	$SR_{VBF\ 2J}$
$\Delta_{\text{B-TAG}}$	3.1	< 1.0	2.8
$\Delta_{e\ \text{P4}}$	< 1.0	< 1.0	< 1.0
$\Delta_{e\ \text{SF}}$	2.0	2.0	2.0
Δ_{JET}	1.4	4.1	11.3
Δ_{JVT}	1.6	< 1.0	1.3
$\Delta_{E_{\text{T}}^{\text{MISS}}}$	< 1.0	< 1.0	< 1.0
$\Delta_{\mu\ \text{P4}}$	< 1.0	< 1.0	< 1.0
$\Delta_{\mu\ \text{SF}}$	2.6	2.3	2.3
Δ_{PU}	< 1.0	< 1.0	< 1.0
	LWA H2800 ggF		
Source	SR_{ggF}	$SR_{VBF\ 1J}$	$SR_{VBF\ 2J}$
$\Delta_{\text{B-TAG}}$	3.5	< 1.0	3.0
$\Delta_{e\ \text{P4}}$	< 1.0	< 1.0	< 1.0
$\Delta_{e\ \text{SF}}$	2.2	2.2	2.2
Δ_{JET}	< 1.0	3.3	8.3
Δ_{JVT}	1.8	< 1.0	1.3
$\Delta_{E_{\text{T}}^{\text{MISS}}}$	< 1.0	< 1.0	< 1.0
$\Delta_{\mu\ \text{P4}}$	< 1.0	< 1.0	< 1.0
$\Delta_{\mu\ \text{SF}}$	3.5	3.1	3.9
Δ_{PU}	< 1.0	1.9	2.0

Table 4.11: The relative impact of experimental uncertainties on the number of ggF signal events in the signal regions for the LWA interpretation of a high-mass scalar boson with a mass of 400, 1000, and 2800 GeV, in percentage of the nominal values. The uncertainties are grouped according to the systematic components described in the text.

Source	SR_{ggF}	CR^{Top}_{ggF}	CR^{WW}_{ggF}	$SR_{VBF\ 1J}$	$SR_{VBF\ 2J}$	CR^{Top}_{VBF}	$CR^{WW}_{VBF\ 1J}$
$\Delta^{W+JETS}_{BKG\ SUBTR.}$	14.5	22.1	12.8	15.8	19.7	12.2	6.6
$\Delta^{W+JETS}_{COMP.}$	28.2	27.1	29.1	26.5	26.5	26.7	28.1
$\Delta^{W+JETS}_{STAT.}$	< 1.0	< 1.0	< 1.0	< 1.0	< 1.0	< 1.0	< 1.0

Table 4.12: The relative impact of the $W+$jets systematic uncertainties on the number of $W+$jets background events in the signal and control regions, in percentage of the nominal values. The uncertainties are grouped according to the systematic components described in the text.

4.5.2 Theory Uncertainties on the Background

Systematic uncertainties on the theoretical predictions of the dominant top quark and WW background contributions are considered in the analysis [86–88]. The impact from variation of systematic components on the number of events and the m_{T} distribution shape is evaluated on the level of event generation and assigned as uncertainties to the two backgrounds.

Top Quark Background

For the impact of uncertainties related to the top quark background, the nominal MC samples are evaluated against datasets with varied generator settings as well as samples produced with alternative generators, as recommended in Ref. [67]. Table B.4 lists the MC simulated samples used for the evaluation of the top background uncertainties. The uncertainty on the hard scatter generation is estimated by comparing samples which simulate the PS with Herwig++, but use Powheg and MadGraph5_aMC@NLO, respectively, for the ME calculation. Uncertainties on the PS modelling are estimated by comparison of the nominal samples with datasets produced with the same description of ME calculation by Powheg, but the alternative Herwig++ generator for simulation of the PS. The uncertainty on the treatment of interference between $t\bar{t}$ and single top tW production is estimated by comparing the Diagram Removal (DR) and Diagram Subtraction (DS) schemes used to subtract interference contributions from simulated tW events. An alternative sample, with the DS scheme employed, is used to evaluate the difference with respect to the nominal sample, which uses the DR scheme. The impact of uncertainties on additional gluon radiation is estimated using samples with simultaneous varied settings on the QCD scales in the ME calculation and the Perugia2012 tune used for the PS generation.
To account for discrepancies between the relative $t\bar{t}$ and single top normalisation, which is estimated simultaneously for both contributions in data control regions, an additional uncertainty is estimated by variation of the relative contribution of the single top process by 20% [87]. Finally, the impact coming from the choice of PDF for the hard scatter generation is estimated by variation of the parameters associated to the fitting procedure for the nominal CT10 PDF set and direct comparison to the alternative MMHT2014 [104] and NNPDF3.0 [105] PDF sets. The uncertainties are estimated by reweighting of the Powheg+Herwig sample to the different PDF configurations and alternative PDF sets. Table 4.13 summarises the relative impact on the number of top quark background events in the signal and control regions, grouped by the components related to the hard scatter modelling ($\Delta^{\mathrm{TOP}}_{\mathrm{ME}}$), the PS simulation ($\Delta^{\mathrm{TOP}}_{\mathrm{PS}}$), the $t\bar{t}$-tW interference subtraction ($\Delta^{\mathrm{TOP}}_{t\bar{t}\text{-}tW}$), the gluon radiation ($\Delta^{\mathrm{TOP}}_{\mathrm{SCALE}}$), the single top background normalisation ($\Delta^{\mathrm{TOP}}_{\sigma(\text{S-TOP})}$), and choice of the PDF for the ME calculation ($\Delta^{\mathrm{TOP}}_{\mathrm{PDF}}$) [87, 88]. For each component, the largest impact in the respective regions is shown. The impact of $\Delta^{\mathrm{TOP}}_{\mathrm{ME}}$ is large in the VBF signal regions, which is found to come from poor description of the jet rapidity of MadGraph5_aMC@NLO+Herwig when compared to Powheg+Herwig [86]. The overall impact is mitigated, since $\Delta^{\mathrm{TOP}}_{\mathrm{ME}}$ has a similar impact on the ggF Top CR.

Source	SR_{ggF}	CR^{Top}_{ggF}	CR^{WW}_{ggF}	$SR_{VBF\ 1J}$	$SR_{VBF\ 2J}$	CR^{Top}_{VBF}	$CR^{WW}_{VBF\ 1J}$
Δ^{TOP}_{ME}	< 1.0	< 1.0	3.8	16.9	48.1	42.4	17.5
Δ^{TOP}_{PS}	12.9	6.2	14.5	15.2	24.8	4.4	9.7
$\Delta^{TOP}_{t\bar{t}\text{-}tW}$	< 1.0	< 1.0	1.4	1.5	1.5	< 1.0	2.2
Δ^{TOP}_{SCALE}	3.2	< 1.0	6.4	4.1	7.9	3.6	4.5
$\Delta^{TOP}_{\sigma(S\text{-}TOP)}$	3.3	2.2	3.1	5.1	1.8	1.2	4.5
Δ^{TOP}_{PDF}	7.4	7.8	9.6	8.2	11.3	9.6	9.1

Table 4.13: The relative impact of theoretical uncertainties on the number of top quark background events in the signal and control regions, in percentage of the nominal values [87, 88]. The uncertainties are grouped according to the systematic components described in the text.

In addition to the uncertainties on the normalisation, the impact of the systematic components on the m_T shape of the top quark background contributions in the ggF SR is taken into account. The impact of the respective variations is parametrised according to first and second order polynomials [87, 88] and considered as additional systematic uncertainties on the shape of the m_T distribution in the final statistical result in Section 4.7. An additional shape uncertainty is derived from the $p^{LEAD}_{T,L}$ correction described in Section 4.3.1. The uncertainty is considered with 50% of the correction impact on the top quark background m_T distribution, as a two-sided variation [87, 88]. Figure 4.25a shows the impact of the shape uncertainty variations on the top quark background m_T distribution in the ggF SR, depicted with the binning strategy described in Section 4.7. The largest impact on the m_T shape comes from the uncertainty associated to the $p^{LEAD}_{T,L}$ correction on the top quark background. The systematic components related to the PS simulation and choice of QCD scale values also show large variation over the full range of the m_T distribution.

WW Background

The uncertainties on the WW background are evaluated in a similar approach to the top quark background theoretical uncertainties, following the recommendations in Ref. [71]. Table B.4 lists the MC simulated samples used for the estimation of the impact of systematic components considered for this background. As described in Section 4.1, the Sherpa generator is used for the simulation of the hard scatter process as well as the PS for the nominal MC sample. To that reason, the uncertainty related to the modelling of these two components is estimated together by comparing the number of selected events in the signal and control regions, obtained with Sherpa, with a sample generated by Powheg and interfaced with Herwig++ for the PS simulation. Uncertainties on the choice of QCD scale values in the ME calculation are derived by separate variation of each QCD scale component, similar to the evaluation for the top quark background. The impact of the choice of PDF for the hard scatter generation is estimated with the same approach as for the top quark background description. The k-factor on the $gg \to WW$ background

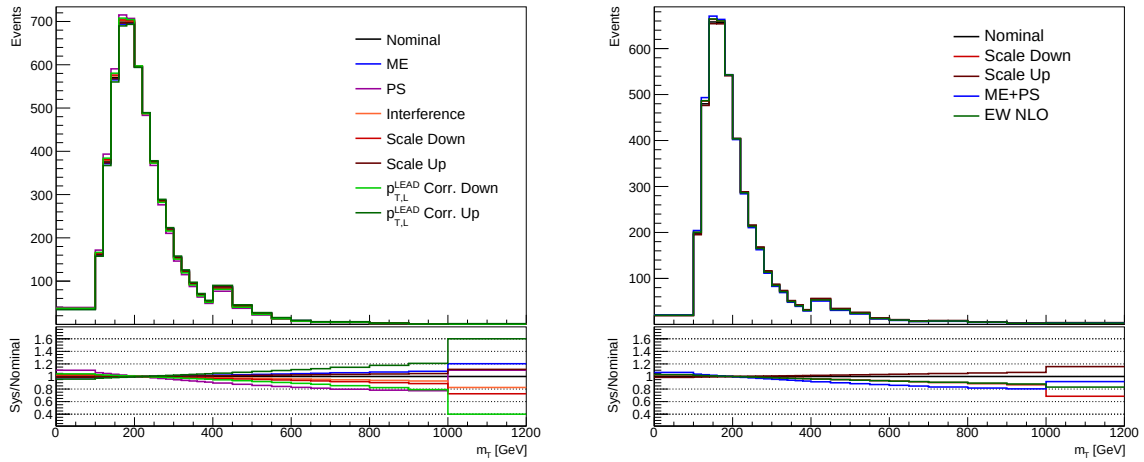

(a) Top quark background (b) WW background

Figure 4.25: The impact on the m_{T} distribution in the ggF SR for the top quark (a) and WW (b) background, according to first and second order polynomial fits of the relative impact from the respective systematic components [87, 88]. The choice of m_{T} intervals is according to the binning strategy described in Section 4.7.

contribution, described in Section 4.3.2, is assigned with a 60% uncertainty. Table 4.14 summarises the relative uncertainties on the number of WW background events in the signal regions and WW background control regions, grouped by the components related to the hard scatter and PS modelling ($\Delta^{\mathrm{WW}}_{\mathrm{ME+PS}}$), the choice of QCD scale values ($\Delta^{\mathrm{WW}}_{\mathrm{SCALE}}$) and PDF ($\Delta^{\mathrm{WW}}_{\mathrm{PDF}}$) for the ME calculation, and the higher order cross section correction of the $gg \to WW$ contribution ($\Delta^{\mathrm{WW}}_{\sigma(gg\to WW)}$) [87, 88]. For each component, the largest impact in the respective regions is shown. The impact of $\Delta^{\mathrm{WW}}_{\mathrm{ME+PS}}$ is large in the VBF signal regions due to significant discrepancies in the forward jet modelling between the nominal Sherpa generator and Powheg+Herwig [86]. Similar to the top quark description, this is mitigated for the VBF 1J SR due to the similar impact of $\Delta^{\mathrm{WW}}_{\mathrm{ME+PS}}$ in the respective WW CR.

Source	$\mathrm{SR}_{\mathrm{ggF}}$	$\mathrm{CR}^{WW}_{\mathrm{ggF}}$	$\mathrm{SR}_{\mathrm{VBF\ 1J}}$	$\mathrm{SR}_{\mathrm{VBF\ 2J}}$	$\mathrm{CR}^{WW}_{\mathrm{VBF\ 1J}}$
$\Delta^{\mathrm{WW}}_{\mathrm{ME+PS}}$	2.9	1.3	35.4	47.7	21.1
$\Delta^{\mathrm{WW}}_{\mathrm{SCALE}}$	7.2	6.6	11.0	25.5	13.3
$\Delta^{\mathrm{WW}}_{\mathrm{PDF}}$	2.8	3.6	1.9	2.9	2.0
$\Delta^{\mathrm{WW}}_{\sigma(gg\to WW)}$	2.5	1.4	5.2	4.4	10.9

Table 4.14: The relative impact of theoretical uncertainties on the number of WW background events in the signal and control regions, in percentage of the nominal values [87,88]. The uncertainties are grouped according to the systematic components described in the text.

The impact on the theory prediction of the shape of the WW m_{T} distribution in the ggF SR is considered for $\Delta^{\mathrm{WW}}_{\mathrm{ME+PS}}$ and $\Delta^{\mathrm{WW}}_{\mathrm{SCALE}}$. With the same approach as for the top quark background, the impact on the m_{T} shape is parametrised with first and second order polynomials [87, 88]. In addition, the EW NLO corrections on the $qq \to WW$ background contributions, described in Section 4.3.2, are considered as a shape uncertainty on the WW background in the ggF SR. Figure 4.25b shows the impact of the shape uncertainty variations on the WW background m_{T} distribution in the ggF SR, depicted with the binning strategy described in Section 4.7. The impact on the m_{T} shape is similar for the three considered systematic sources.
Given the different behaviour of the EW NLO correction factors with increasing m_{T}, an additional uncertainty of 3.2% is assigned to the WW background normalisation. This is derived from the relative difference in the number of WW background events between the ggF SR and CR after applying the EW NLO correction to the $qq \to WW$ background cross section [87, 88].

4.5.3 Theory Uncertainties on the Signal

The impact of theoretical uncertainties on the signal selection efficiency in each SR is evaluated for several mass points within the considered mass range of the high-mass scalar boson interpretations, separately for the ggF and VBF production mode [86, 87, 97]. Variations on systematic components related to PDF uncertainties, PS simulation, and QCD scales used in the hard scatter generation are studied on particle level in Powheg+Pythia generated events to estimate the impact on the signal acceptance in each signal region. The dependence on the signal mass is found to be small, thus the largest deviation for each uncertainty source in the different signal regions is taken as uncertainty for all signal masses. The evaluation of PDF uncertainties is done in a similar approach as for the top quark and WW background, by variation of fit parameters of the nominal CT10 PDF set calculation and comparison to the alternative MSTW2008 [53] and NNPDF3.0 PDF sets. Uncertainties on the hard scatter generation are estimated by variation of the QCD scales in the ME calculation. The impact from uncertainties on the PS simulation is estimated by variation of parameters in Pythia, in particular related to MPI and FSR. Table 4.15 summarises the resulting uncertainties on the signal selection efficiency in all signal regions for each systematic source [87, 97].

Uncertainty from Jet Migration

In addition to the uncertainty on the ggF signal selection efficiency in each SR due to the variation of the QCD scales, the impact of jet migration effects between the regions is considered as well [86, 87, 97]. The normalisation uncertainty from QCD scale variations in the three disjoint signal categories is estimated with the Stewart-Tackmann method [106], which exploits that uncertainties on cross sections of jet exclusive selections can be estimated from cross section uncertainties inclusive in jet multiplicity. The uncertainties are incorporated in nuisance parameter definitions according to the procedure described in

	ggF			VBF		
Source	SR_{ggF}	$SR_{VBF\ 1J}$	$SR_{VBF\ 2J}$	SR_{ggF}	$SR_{VBF\ 1J}$	$SR_{VBF\ 2J}$
Δ^{SIGNAL}_{PDF}	< 1.0	3.4	2.3	3.2	3.4	1.9
Δ^{SIGNAL}_{PS}	< 1.0	2.7	5.0	< 1.0	< 1.0	< 1.0
Δ^{SIGNAL}_{SCALE}	< 1.0	< 1.0	< 1.0	4.2	3.7	6.8

Table 4.15: The relative impact of theoretical uncertainties on the ggF and VBF selection rate in the signal regions, in percentage of the nominal values [87, 97]. The systematic components for PDF (Δ^{SIGNAL}_{PDF}), PS (Δ^{SIGNAL}_{PS}), and QCD scale (Δ^{SIGNAL}_{SCALE}) variations is shown.

Ref. [107], in order to adopt the Stewart-Tackmann method to the specific VBF categorisation used in the analysis. The impact on the signal normalisation according to these nuisance parameters is determined for signal masses between 300 and 3000 GeV and used to derive the uncertainties due to jet migration effects. They range from 7 to 9% in the ggF SR, 30 to 86% in the VBF 1J SR, and 25 to 38% in the VBF 2J SR, within the considered mass window [87, 97].

4.5.4 Summary

In the previous sections the impact of theoretical and experimental uncertainties on the number of predicted signal and background events in the signal and control regions was discussed. In the likelihood fit evaluation described in Section 4.6, the variation of a given systematic component is correlated between all processes it affects, which can lead to cancellation effects between the different background contributions. Furthermore, the variation is performed simultaneously in the signal and control regions, which can mitigate the impact of systematic uncertainties on the background contributions that are constrained by the respective data control regions.
The resulting systematic uncertainty impact is different for the fit results of the ggF and the VBF signal interpretation [87, 108]. For the ggF signal, the largest impact comes from

- Uncertainty on the top quark background related to the $p^{LEAD}_{T,L}$ correction, the PS simulation, the gluon radiation, and the single top background normalisation
- Uncertainty on the ggF signal related to jet migration
- Uncertainty on the WW background related to the EW NLO corrections, the hard scatter and PS modelling, and the choice of QCD scale values

The largest impact for the VBF signal fit comes from

- Uncertainty related to the JES and JER calibration and the b-jet identification
- Uncertainty on the top quark background related to the choice of PDF for the ME calculation and the $t\bar{t}$-tW interference subtraction

- Uncertainty on the W + jets background related to the jet flavour composition
- Uncertainty on the WW background related to the choice of QCD scale values

4.6 Statistical Evaluation

In the following, the statistical methodology used to obtain the results presented in Section 4.7 is introduced. A more detailed description of the statistical treatment is given in Refs. [95] and [109]. The observed events in recorded data and events from MC simulation prediction are evaluated in a binned likelihood fit. The distribution of the main discriminant m_{T} in the three signal regions defines the m_{T} intervals (bins) that are treated separately in the fit. The events in each control region are taken into account inclusively, without separation in bins of m_{T}.
The treatment of the background contributions uses extrapolation factors to determine how the fitted background rates extrapolate from the control to the signal regions, as well as across the different control regions [87,96]. As a simple example, the likelihood function $\mathcal{L}$ for a single SR m_{T} bin and one CR can be written as the product of two conditional Poisson probability functions:

$$\mathcal{L}(\mu, \mu_b) = P(N|\mu\, s + \mu_b\, b_{SR}) \times P(M|\mu_b\, b_{CR}). \tag{4.14}$$

N and M are the number of data events in the SR m_{T} bin and the CR, respectively. The expected number of events in the SR m_{T} bin for the background normalised by the control region and the signal is represented by b_{SR} and s, respectively. The signal strength parameter μ is the ratio of the measured $\sigma \times BR(H \to WW)$ to the value assumed for the signal interpretations in Section 4.4, which scales the number of expected signal events. The strength parameter μ_b simultaneously scales the expected number of background events in the CR (b_{CR}) and b_{SR}, which is used to parametrise the extrapolation of the event rates for this background across the regions in the fit. The background contributions treated in this way are the top quark background in the ggF, VBF 1J, and VBF 2J region and the WW background in the ggF and VBF 1J region, according to the control regions defined in Section 4.3.

For the full likelihood function, the simple example is expanded to all bins of the three SR m_{T} distributions [86, 87, 96]:

$$\mathcal{L}(\mu, \boldsymbol{\theta}) = \{\prod_{i}^{N_{\mathrm{SR}}} \prod_{j}^{N_{\mathrm{bins}}} P(N_{ij}|(\mu\, s_{ij} + \sum_{m}^{N_{\mathrm{bkg}}} b_{ijm}))\} \times \prod^{N_\theta} N(\tilde{\theta}|\theta). \tag{4.15}$$

The impact of the background normalisation as well as signal and background uncertainties on the likelihood fit is represented by probability functions $N(\tilde{\theta}|\theta)$ of nuisance parameters θ. The full set of nuisance parameters is denoted with $\boldsymbol{\theta}$. For the normalisation of a given background, the respective nuisance parameter reflects the background strength parameter and the auxiliary measurement $\tilde{\theta}$ the number of data events M in the CR, as demonstrated in Eq. 4.14. Nuisance parameters are taken into account for all systematic uncertainty sources described in Section 4.5, as well as the statistical uncertainties on the background prediction in all control regions and SR m_{T} bins.

In the absence of a signal excess in data, the modified frequentist CL_s method [110] is used to employ constraints on the production rate of a heavy scalar boson according to the signal interpretations considered [86, 87, 96]. The method defines a test statistic q_μ, described as

$$q_\mu = -2 \ln \left(\frac{\mathcal{L}(\mu, \hat{\boldsymbol{\theta}}_\mu)}{\mathcal{L}(\hat{\mu}, \hat{\boldsymbol{\theta}})} \right), \tag{4.16}$$

where $\hat{\mu}$ and $\hat{\boldsymbol{\theta}}$ are the values of μ and $\boldsymbol{\theta}$ for which $\mathcal{L}$ is unconditionally maximised. The values $\hat{\boldsymbol{\theta}}_\mu$ maximise $\mathcal{L}$ for a given value μ. Upper limits on μ at 95% confidence level (C.L.) are derived with sampling distributions of q_μ, which are approximated with asymptotic formulae described in Ref. [111]. The limits are interpreted as upper exclusion boundaries on $\sigma \times BR(H \rightarrow WW)$ to remove the dependence on model specific assumptions on the expected production rate of the signal. In addition to observed limits, which place boundaries on signal interpretations according to the observed data, expected limits are derived to estimate the sensitivity of the analysis to the signal models. For the calculation of expected limits, the data in the fit is set to the combined background prediction.

SR_{ggF} bin boundaries [GeV]														
0	100	120	140	160	180	200	220	240	260	280	300	320	340	360
380	400	450	500	550	600	650	700	800	900	1000	1200			

$SR_{VBF\ NJ}$ bin boundaries [GeV]										
0	100	150	200	250	300	350	400	500	600	1200

Table 4.16: The interval boundaries used for the input histograms to the likelihood fit for the ggF SR (top) and VBF 1J and VBF 2J SR (bottom). The last interval includes entries above the uppermost bin boundary.

4.7 Results

In this section the preliminary results of the high-mass $H \to W^+W^- \to \ell^+\nu\ell^-\bar{\nu}$ analysis are presented, as published for the ICHEP summer conference in 2016 [86]. Furthermore, the possible interpretation of these results in the context of model specific theories and the comparison to other analyses is discussed.
The main discriminant of the analysis is the m_{T} distribution, which is used as input variable to the binned likelihood fit described in Section 4.6. Signal and background contributions in the signal regions for each process, as well as the observed data, are evaluated in bins of m_{T} with varying width. The choice of the interval boundaries is motivated by the increasing width of the m_{T} distribution with higher masses of the heavy boson and preserves sufficient statistical precision of the estimated background contributions in each bin. Table 4.16 summarises the chosen bin boundaries for the ggF SR and the VBF 1J and VBF 2J SR. Contributions in the control regions are used in the likelihood fit to constrain the normalisation of the top quark and WW background and are included without the separation in m_{T} intervals.
The distribution of m_{T} in the signal regions, after the full evaluation of the likelihood fit, is shown in Figure 4.26. Table 4.17 summarises the number of background events after the fit to the observed events in data, in the signal and control regions. No significant excess above data is observed across the whole range of m_{T} in the three signal regions and predictions on the SM background are fully compatible with the observed yields in data. In the absence of a signal excess, upper limits on $\sigma \times BR(H \to WW)$ for the NWA and LWA interpretation are derived according to the statistical methods described in Section 4.6.

4.7.1 Limits on NWA Signal Interpretation

Limits on $\sigma \times BR(H \to WW)$ for the NWA signal interpretation are derived separately for the ggF and VBF production mode [86]. For the expected limit on the ggF (VBF) mode, the contributions of the VBF (ggF) signal are set to 0, which makes the fit agnostic to the respective other production channel. The evaluation of the observed limits for the ggF (VBF) production mode treats the contribution of the VBF (ggF) signal as an additional

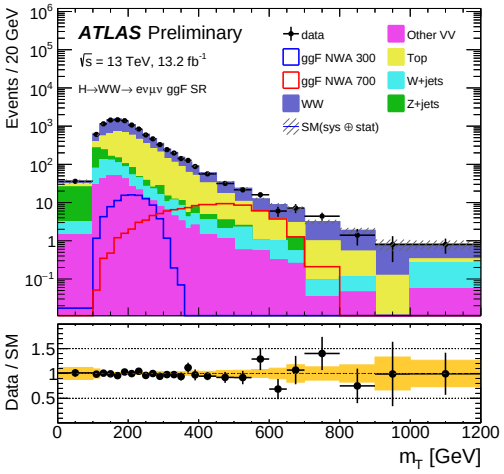

(a) ggF

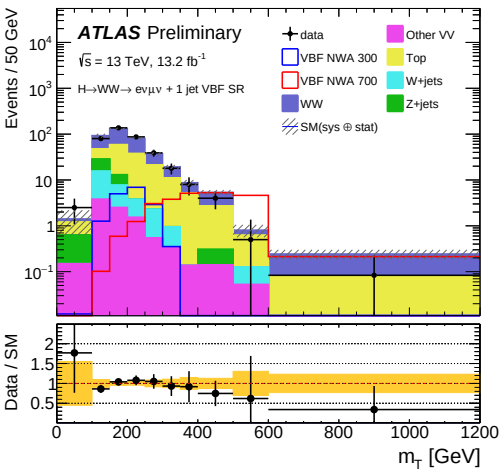

(b) VBF 1J

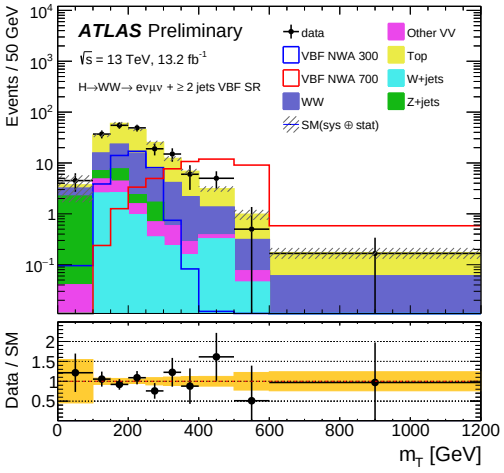

(c) VBF 2J

Figure 4.26: The distribution of m_{T} in the ggF (a), VBF 1J (b), and VBF 2J (c) SR according to the background contributions after the fit to data [86]. The last interval includes entries above the uppermost bin boundary. The shaded band in the top histogram and the yellow band in the bottom histogram depict the combined statistical and systematic uncertainties on the full background, after the evaluation of the likelihood fit. The negligible contribution of the SM Higgs boson from VBF production is omitted.

	SR_{ggF}	Top CR_{ggF}	WW CR_{ggF}
WW	5300 ± 400	430 ± 90	1430 ± 120
Top-quark	4200 ± 400	20560 ± 210	900 ± 100
Z/γ^*	557 ± 25	46 ± 12	10.7 ± 1.0
W+jets	450 ± 120	260 ± 80	105 ± 30
VV	323 ± 12	37 ± 4	88.5 ± 3.4
Backgrounds	10790 ± 110	21330 ± 180	2530 ± 40
Data	10718	21333	2589

(a) ggF regions

	SR_{VBF1J}	SR_{VBF2J}	Top CR_{VBF}	WW CR_{VBF1J}
WW	197 ± 31	53 ± 15	37 ± 4	117 ± 21
Top-quark	141 ± 26	124 ± 19	2650 ± 80	65 ± 14
Z/γ^*	20 ± 7	12 ± 4	40 ± 17	27 ± 5
W+jets	22 ± 6	7.5 ± 2.2	95 ± 25	24 ± 6
VV	9.5 ± 1.0	5.7 ± 0.8	5.2 ± 2.2	11.0 ± 1.5
Backgrounds	389 ± 22	202 ± 14	2830 ± 70	247 ± 16
Data	384	203	2825	253

(b) VBF regions

Table 4.17: The number of predicted background and observed data events after the full evaluation of the likelihood fit for the ggF (a) and VBF (b) signal and control regions [86]. The combined statistical and systematic uncertainties on the different background components, as well as on the combined background, after the fit to data, are shown. The negligible contribution of the SM Higgs boson from VBF production is omitted.

nuisance parameter in the fit using a flat prior, following the same treatment as for the background normalisation. This avoids making assumptions on the presence or absence of a signal from the production mode not being probed, which is normalised by the data in the fit regions with this approach. Figure 4.27 shows the 95% C.L. upper limit on $\sigma \times BR(H \to WW)$ dependent on m_H for the NWA signal interpretation for the ggF and VBF production mode, in the mass range from 300 to 3000 GeV [86]. The observed limit is well within the one sigma deviation of the expected limit. The observed variation to -1σ for masses between 400 and 800 GeV of the ggF limits can be identified with the slight statistical under fluctuation of data in m_{T} between 300 and 600 GeV in Figure 4.26a. The gradual tendency to the -1σ boundary of the observed VBF limit manifests clearly from the under fluctuation of data towards high values of m_{T} in Figure 4.26b, which is nonetheless well within the uncertainties. Observed and expected limits on the NWA ggF and VBF signal interpretation, for masses of 400, 1000, and 2800 GeV are shown in Table 4.18 [86, 108].

4.7.2 Limits on LWA Signal Interpretation

The results for the LWA signal are evaluated for widths of 5%, 10%, and 15% of the assumed heavy boson mass, where the 5% and 10% signal predictions are obtained with the reweighting procedure described in Section 4.4. Figure 4.28 shows the 95% C.L. upper

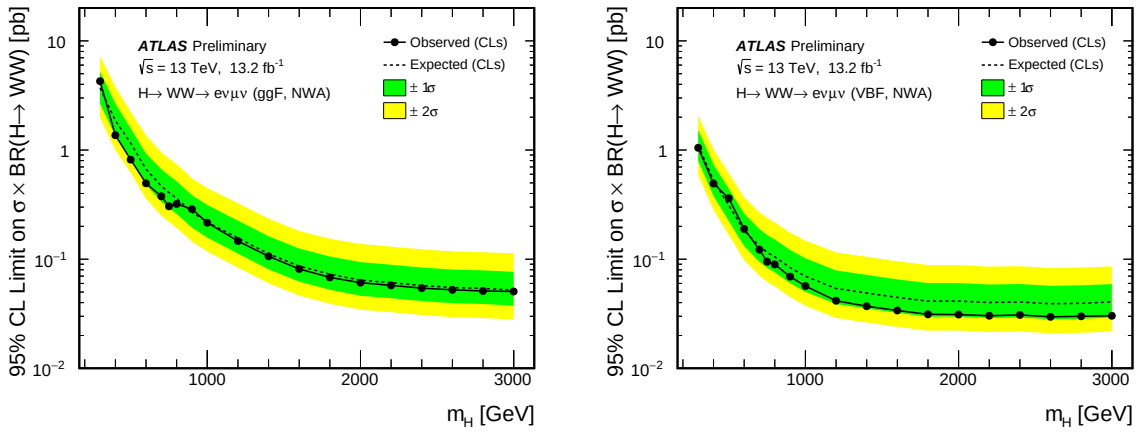

(a) ggF (b) VBF

Figure 4.27: The expected (dashed line) and observed (solid line) upper limits on $\sigma \times BR(H \to WW)$ at 95% C.L. for the NWA ggF (a) and VBF (b) signal interpretation [86]. The yellow (green) band indicates the ± 2 (± 1) σ uncertainty on the expected limits.

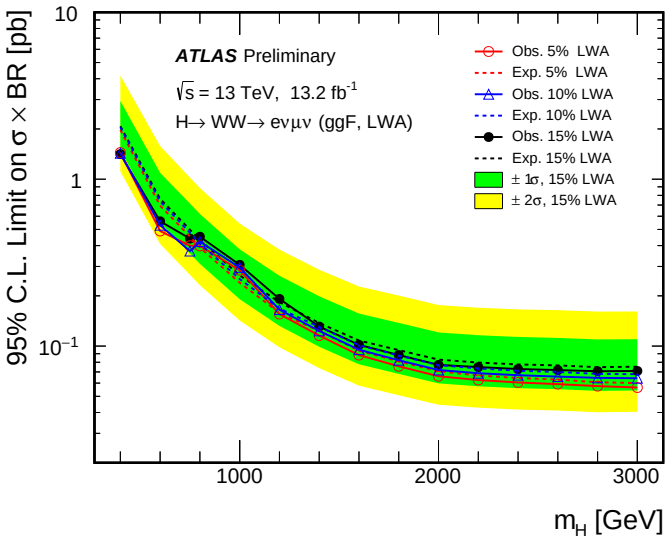

Figure 4.28: The expected (dashed line) and observed (solid line) upper limits on $\sigma \times BR(H \to WW)$ at 95% C.L. for the LWA ggF signal interpretation with line widths of 5% (red), 10% (blue), and 15% (black) of m_H [86]. The yellow (green) band indicates the ± 2 (± 1) σ uncertainty on the 15% $\times\, m_H$ expected limits.

	Limits on NWA ggF [pb]			Limits on NWA VBF [pb]		
	400 GeV	1000 GeV	2800 GeV	400 GeV	1000 GeV	2800 GeV
observed	1.37	0.22	0.051	0.49	0.057	0.030
expected	$1.86^{+0.81}_{-0.52}$	$0.22^{+0.095}_{-0.061}$	$0.054^{+0.025}_{-0.015}$	$0.53^{+0.21}_{-0.15}$	$0.070^{+0.032}_{-0.019}$	$0.039^{+0.018}_{-0.011}$

Table 4.18: The observed and expected upper limits on $\sigma \times BR(H \to WW)$ at 95% C.L. for the NWA ggF and VBF signal interpretation for masses of 400, 1000, and 2800 GeV [86, 108]. The $\pm 1\sigma$ uncertainty on the expected limit is indicated as well.

	Limits on LWA (5%/10%/15%) ggF [pb]		
	400 GeV	1000 GeV	2800 GeV
observed	1.4 / 1.4 / 1.4	0.29 / 0.30 / 0.31	0.058 / 0.065 / 0.071
expected	$2.0^{+0.83}_{-0.55}$ / $2.0^{+0.83}_{-0.57}$ / $2.1^{+0.87}_{-0.58}$	$0.24^{+0.10}_{-0.067}$ / $0.25^{+0.11}_{-0.071}$ / $0.27^{+0.12}_{-0.074}$	$0.061^{+0.028}_{-0.017}$ / $0.068^{+0.032}_{-0.019}$ / $0.075^{+0.035}_{-0.021}$

Table 4.19: The observed and expected upper limits on $\sigma \times BR(H \to WW)$ at 95% C.L. for the LWA ggF signal interpretation for masses of 400, 1000, and 2800 GeV and line widths of 5%, 10%, and 15% of m_H [86,108]. The $\pm 1\sigma$ uncertainty on the expected limit is indicated as well.

limit on $\sigma \times BR(H \to WW)$ dependent on m_H for the LWA signal interpretation for the ggF production mode, in the mass range from 400 to 3000 GeV [86]. Observed and expected limits on the LWA ggF signal interpretation, for masses of 400, 1000, and 2800 GeV are shown in Table 4.19 [86, 108]. The exclusion limits on the ggF production mode for the LWA interpretation are higher than the ones for the NWA interpretation and this difference increases with higher masses of the hypothesised heavy scalar boson. Furthermore, the difference between the assumed line widths increases with m_H. This reflects the decreased sensitivity of the analysis to the signal, due to the broader m_{T} distribution of LWA and the increasing impact of the line width reweighting with increasing values of m_H, as discussed in Section 4.4.

4.7.3 Discussion

The presented results place upper boundaries on the cross section of a heavy scalar boson decaying to two W bosons, produced in the ggF or VBF production mode. The limits are model independent and can be used as experimental constraints on theories that predict one or more additional bosonic resonances with the $\ell^-\bar{\nu}\ell^+\nu$ decay signature. As an example, the results on the NWA ggF signal interpretation in Section 4.7.1 were used in the context of Composite Higgs Models in the study presented in Ref. [112], among several other diboson and $t\bar{t}$ resonance searches at $\sqrt{s} = 13$ TeV by ATLAS and CMS.

In the following, the results on the NWA signal interpretation are compared to three other analyses that were performed in ATLAS and CMS with data at $\sqrt{s} = 13$ TeV. The analysis described in Ref. [113] performed the search for a charge neutral bosonic resonance produced in the VBF channel that decays to the $\ell^-\bar{\nu}\ell^+\nu$ final state with 3.2 fb^{-1} of ATLAS recorded data. Various scenarios with different properties of the boson are considered, some of which assume a spin of 0. The properties in particular also affect the width of the resonance. The inclusive decay of the boson to the $\ell^-\bar{\nu}\ell^+\nu$ final state has been studied, taking into account interference effects with the background coming from SM processes. Results are presented for a heavy boson mass between 200 and 500 GeV in the form of upper exclusion limits at 95% C.L. on the cross section, which includes the branching fraction to the final leptonic state ($\sigma(qq \to Rqq \to \ell^-\bar{\nu}\ell^+\nu qq)$). The exclusion limits on the NWA VBF signal interpretation (see Section 4.7.1) in the mass range between 300 and 500 GeV can be compared to these results, taking into account some considerations.
The impact of non-negligible widths of the heavy boson in the ggF production channel have been shown to be small in the context of the LWA signal interpretation (see Section 4.7.2), in particular in the lower mass range. This is expected to be similar for a heavy boson in the VBF channel. Furthermore, the consideration of a narrow line width in the NWA interpretation assumes that there is a negligible impact from interference effects with SM processes. The decay of the bosonic resonances assumed in Ref. [113] considers the decay to two W bosons as well as to two Z bosons with the $\ell^-\bar{\nu}\ell^+\nu$ final state. In that regard, the NWA analysis presented in this thesis explored a more restricted phase-space of a heavy boson produced in the VBF channel. In order to compare the exclusion limit results of both analyses, the limits in Section 4.7.1 have to be multiplied with $BR(W^+W^- \to \ell^-\bar{\nu}\ell^+\nu) \approx 10\%$. The analysis presented in Ref. [113] excludes a scalar bosonic resonance with a cross section $\sigma(qq \to Rqq \to \ell^-\bar{\nu}\ell^+\nu qq)$ down to 220 fb for a heavy boson mass of 500 GeV. The result for the NWA VBF signal presented in Section 4.7.1 at this mass point is 360 fb multiplied with $BR(W^+W^- \to \ell^-\bar{\nu}\ell^+\nu)$, leading to an exclusion limit that is smaller by a factor of ~ 6. Consequently, the NWA VBF signal analysis places more stringent boundaries on the diboson decay signature of a scalar heavy bosonic resonance produced in the VBF channel, even after considering the discussed differences between the two analyses. Furthermore, while only masses down to 300 GeV were considered by the NWA VBF signal analysis, a much larger range up to 3000 GeV was explored.

The semi-leptonic decay ($\ell\nu qq$) of the two W bosons from a heavy scalar boson was also explored in ATLAS by the analysis in Ref. [114] with 13.2 fb^{-1} of data. The $\ell\nu qq$ analysis places upper exclusion limits at 95% C.L. on $\sigma \times BR(H \to WW)$ for a high-mass Higgs boson according to the NWA ggF signal interpretation in a heavy boson mass range between 500 and 3000 GeV. This allows for a direct comparison with the results presented in Section 4.7.1. At low masses of the hypothesised heavy boson, the $\ell^-\bar{\nu}\ell^+\nu$ and the $\ell\nu qq$ analysis show similar results in terms of the excluded cross sections, with the $\ell^-\bar{\nu}\ell^+\nu$ analysis probing an extended range down to 300 GeV. With increasing mass of the high-mass Higgs, the sensitivity of the $\ell\nu qq$ channel increases significantly more compared to

the $\ell^-\bar{\nu}\ell^+\nu$ final state. This is driven by the much larger branching fraction of the semi-leptonic WW decay, but also by the experimental techniques that can be exploited in this decay channel. In particular, the signature of only one charged lepton and its associated neutrino allows for the full reconstruction of the invariant mass of the high-mass Higgs boson, by employing the constraint on the invariant mass of the $\ell\nu$ pair to be equal to the W boson mass [114]. Still, the two analyses provide complementary results, especially in the low range of the hypothesised heavy boson mass.

Preliminary results for the high-mass Higgs boson search in the $H \to W^+W^- \to \ell^+\nu\ell^-\bar{\nu}$ channel are also reported by the CMS experiment for 2.3 fb^{-1} of Run-II data, recorded in 2015 [115]. The analysis considers various line widths of the heavy Higgs boson in the context of the EWS model, in the mass range from 200 to 1000 GeV. Results are presented in the form of exclusion limits on the combined ggF and VBF production cross section multiplied with the branching ratio to the leptonic final state ($\sigma \times BR(H \to W^+W^- \to \ell^+\nu\ell^-\bar{\nu})$). In order to make a rough comparison between the CMS analysis and the results presented in this thesis, the results on the NWA VBF signal in Section 4.7.1 can be compared with the CMS results for the lowest considered signal width. Taking into account the branching ratio $BR(W^+W^- \to \ell^-\bar{\nu}\ell^+\nu) \approx 10\%$, the NWA VBF analysis employs more stringent limits on a high-mass Higgs boson in the $H \to W^+W^- \to \ell^+\nu\ell^-\bar{\nu}$ channel and also explores a larger mass range up to 3000 GeV.

Chapter 5

Conclusions and Outlook

In this thesis, the search for a high-mass Higgs boson in the $H \to W^+W^- \to \ell^+\nu\ell^-\bar{\nu}$ channel with the first data of 13.2 fb^{-1} integrated luminosity, recorded by the ATLAS experiment at a proton-proton centre-of-mass energy of 13 TeV, was presented. In the context of an extension of the Standard Model Higgs sector, the presence of a resonance corresponding to a charge neutral scalar particle is probed in the spectrum of the transverse mass reconstructed from the two charged leptons and the missing transverse momentum due to the two neutrinos. Three regions of interest are defined to target the characteristic kinematic properties of the two dominant production modes of the Higgs boson, the gluon-gluon fusion and the vectorboson fusion. Control regions are used to constrain the normalisation of the dominant background contributions coming from top quark processes and the non-resonant decay of W boson pairs in a binned likelihood fit. No significant excess above the combined background from Standard Model processes has been observed. In the absence of a signal excess, the CL$_s$ method is used to place upper exclusion limits on the Higgs production cross section times the branching ratio to two W bosons. Two signal interpretations are studied, with different line widths of the resonance but no assumption on the production rate of the hypothesised heavy boson. The narrow width approximation assumes a negligible width, much smaller than the experimental resolution of the detector. The large width approximation takes into account broad line widths of 5%, 10%, and 15% of the assumed pole mass of the boson. Heavy boson masses between 300 (400) and 3000 (3000) GeV are probed for the signal interpretation with negligible (large) width. With the narrow width approximation, a cross section down to 1.37 (0.051) pb and 0.49 (0.030) pb can be excluded at 95% confidence level for a high-mass Higgs boson with mass 400 (2800) GeV in the gluon-gluon fusion and vectorboson fusion production mode, respectively. For a large width heavy boson with mass 400 (2800) GeV in the gluon-gluon fusion production channel, cross sections down to 1.4 (0.058), 1.4 (0.065), and 1.4 (0.071) pb are excluded at 95% confidence level for a line width of 5%, 10%, and 15% of the heavy boson mass, respectively.

The main contributions to the analysis include a significant share in the construction of an analysis framework for Run-II and then the implementation of the high-mass analysis

within this framework, as well as the preparation of simulated and recorded data for the final evaluation in the likelihood fit. A strong focus was also put on the evaluation of the impact of experimental uncertainties on the different phase-space regions covered by the analysis. Furthermore, the impact of jet multiplicity with regards to the signal categorisation was studied in detail, leading to the analysis strategy that was used for the preliminary results published at the ICHEP summer conference in 2016 [86].

With the excellent performance of the LHC, a large amount of 13 TeV proton-proton collision data is expected over the course of the Run-II data taking period. By the end of 2016, the integrated luminosity of data appropriate for physics analysis already increased to approximately 36 fb^{-1}, which significantly improves the sensitivity of the high-mass $H \to W^+W^- \to \ell^+\nu\ell^-\bar{\nu}$ analysis, in particular in the statistically limited VBF regions. In progression of the analysis, a number of updates and studies will help to improve and extend the search for a high-mass boson in the fully leptonic decay channel of two W bosons.
An extensive understanding of the dominant top quark and WW background processes at 13 TeV proton-proton collisions is crucial for probing the spectrum of the transverse mass for a signal excess. The modelling of the top quark processes with the nominal MC generator was shown to cause discrepancies between the prediction and the observed data. Alternative generators are taken into consideration for the future, which provide extended higher order QCD calculations. For the description of the $qq \to WW$ background processes, EW NLO calculations provided by the authors of Ref. [94] are used for an additional source of systematic uncertainty. The impact of QCD next-to-next-to-leading order (NNLO) calculations for this background is shown to be significant and with different sign to the impact from EW NLO corrections [89]. The correct description of the WW background requires the inclusion of both sources of higher order effects. In addition to the nominal predictions on the background processes, the modelling and choice of alternative generator samples for the estimation of theoretical uncertainties is an important handle for improvement to the analysis.
For the search of a high-mass Higgs boson with the first 13 TeV proton-proton collision data, model independent interpretations on negligible and large widths were chosen. The inclusion of additional model dependent signal interpretations greatly increases the reach of the analysis. General extensions to the Standard Model Higgs sector, in form of the electroweak singlet [5] and the two Higgs doublet model [6], as well as interpretations in the context of heavy vector triplets [116] and a Randall-Sundrum graviton [117] are considered for future analysis. The impact of interference effects with the Standard Model Higgs boson and the non-resonant WW background on interpretations with non-negligible line widths are shown to be significant [8, 98, 99] and have to be studied in the context of models with considerable signal widths. Finally, the inclusion of the final state where the two charged leptons are both electrons or muons is expected to give a significant increase in sensitivity.

The presented exclusion limits represent the latest, most sensitive 13 TeV data result for the search for a high-mass Higgs boson in the $H \to W^+W^- \to \ell^+\nu\ell^-\bar{\nu}$ channel, with an

extended range from 1500 to 3000 GeV of the considered heavy boson mass compared to the analysis with 8 TeV data. With the increasing amount of ATLAS data the WW channel will continue to play an important role in heavy boson searches, with the fully leptonic decay being the cleanest decay mode of this diboson channel. In terms of exploring new domains of particle physics, the start of Run-II and the years to follow mark one of the most exciting episodes in the operational lifetime of the LHC and its collision experiments. If new physics is hiding in the current kinematical reach of the accelerator, it will most likely reveal itself in the years to come.

Appendix A

Input for the Likelihood Fit

In order to provide the likelihood fit (see Section 4.6) with input data, histograms are filled with the events passing the full selection defined in Section 4.2.2, separately for all signal and background processes as well as the observed data. The m_{T} distribution with interval boundaries specified in Table 4.16 is used in the three signal regions. The histogram bins are remapped to equal width in an arbitrary scale between zero and one, as required by the code which performs the likelihood fit evaluation. Figure A.1 shows the m_{T} distributions of the three signal regions according to the respective interval boundaries, before and after the remapping to equal width. Contributions in the control regions are included without the separation in m_{T} intervals.

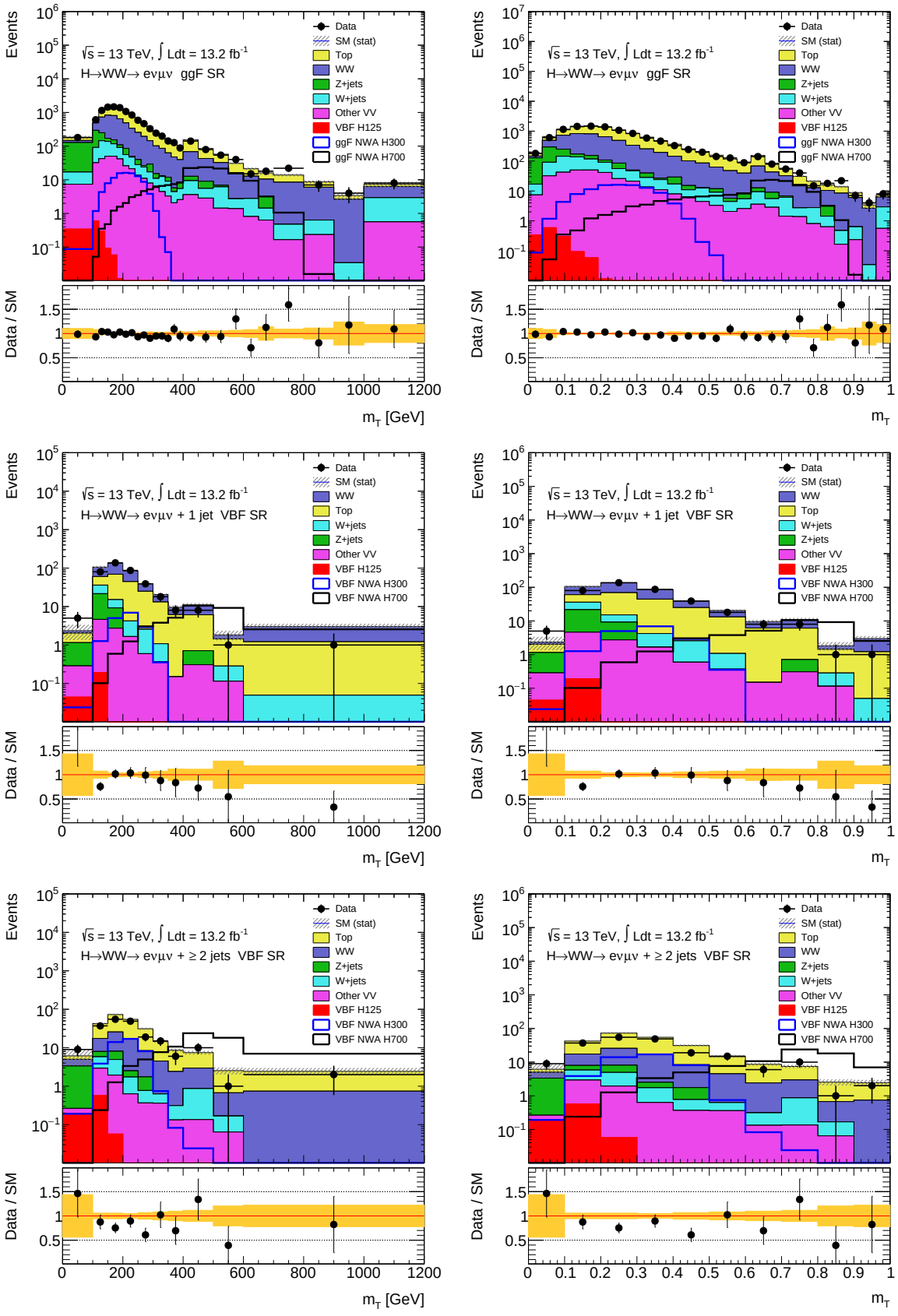

Figure A.1: The distribution of m_{T} in the ggF (top), VBF 1J (middle), and VBF 2J (bottom) SR according to the varied interval boundaries (left) and the remapped intervals (right) for the input to the likelihood fit. The last interval includes entries above the uppermost bin boundary. The hatched band in the top panel and the shaded band in the bottom panel depict the statistical uncertainty on the full background.

Appendix B

Monte Carlo Samples

ID	Name	σ_{MC}/nb	k-factor	$\epsilon_{\mathrm{FILTER}}$
341007	PowhegPythia8EvtGen_CT10_AZNLOCTEQ6L1_ggH300NWA_WWlvlv	$1.07 \cdot 10^{-4}$	1.00	0.581
341008	PowhegPythia8EvtGen_CT10_AZNLOCTEQ6L1_ggH400NWA_WWlvlv	$1.07 \cdot 10^{-4}$	1.00	0.593
341009	PowhegPythia8EvtGen_CT10_AZNLOCTEQ6L1_ggH500NWA_WWlvlv	$1.07 \cdot 10^{-4}$	1.00	0.599
341010	PowhegPythia8EvtGen_CT10_AZNLOCTEQ6L1_ggH600NWA_WWlvlv	$1.07 \cdot 10^{-4}$	1.00	0.606
341011	PowhegPythia8EvtGen_CT10_AZNLOCTEQ6L1_ggH700NWA_WWlvlv	$1.07 \cdot 10^{-4}$	1.00	0.608
343465	PowhegPythia8EvtGen_CT10_AZNLOCTEQ6L1_ggH750NWA_WWlvlv	$1.07 \cdot 10^{-4}$	1.00	0.610
341012	PowhegPythia8EvtGen_CT10_AZNLOCTEQ6L1_ggH800NWA_WWlvlv	$1.07 \cdot 10^{-4}$	1.00	0.611
341013	PowhegPythia8EvtGen_CT10_AZNLOCTEQ6L1_ggH900NWA_WWlvlv	$1.07 \cdot 10^{-4}$	1.00	0.612
341014	PowhegPythia8EvtGen_CT10_AZNLOCTEQ6L1_ggH1000NWA_WWlvlv	$1.07 \cdot 10^{-4}$	1.00	0.615
343373	PowhegPythia8EvtGen_CT10_AZNLOCTEQ6L1_ggH1200NWA_WWlvlv	$1.07 \cdot 10^{-4}$	1.00	0.617
341015	PowhegPythia8EvtGen_CT10_AZNLOCTEQ6L1_ggH1400NWA_WWlvlv	$1.07 \cdot 10^{-4}$	1.00	0.618
343374	PowhegPythia8EvtGen_CT10_AZNLOCTEQ6L1_ggH1600NWA_WWlvlv	$1.07 \cdot 10^{-4}$	1.00	0.622
341016	PowhegPythia8EvtGen_CT10_AZNLOCTEQ6L1_ggH1800NWA_WWlvlv	$1.07 \cdot 10^{-4}$	1.00	0.624
343375	PowhegPythia8EvtGen_CT10_AZNLOCTEQ6L1_ggH2000NWA_WWlvlv	$1.07 \cdot 10^{-4}$	1.00	0.626
341017	PowhegPythia8EvtGen_CT10_AZNLOCTEQ6L1_ggH2200NWA_WWlvlv	$1.07 \cdot 10^{-4}$	1.00	0.625
343376	PowhegPythia8EvtGen_CT10_AZNLOCTEQ6L1_ggH2400NWA_WWlvlv	$1.07 \cdot 10^{-4}$	1.00	0.628
341018	PowhegPythia8EvtGen_CT10_AZNLOCTEQ6L1_ggH2600NWA_WWlvlv	$1.07 \cdot 10^{-4}$	1.00	0.632
343377	PowhegPythia8EvtGen_CT10_AZNLOCTEQ6L1_ggH2800NWA_WWlvlv	$1.07 \cdot 10^{-4}$	1.00	0.629
341019	PowhegPythia8EvtGen_CT10_AZNLOCTEQ6L1_ggH3000NWA_WWlvlv	$1.07 \cdot 10^{-4}$	1.00	0.630
341022	PowhegPythia8EvtGen_CT10_AZNLOCTEQ6L1_VBF300NWA_WWlvlv	$1.07 \cdot 10^{-4}$	1.00	0.588
341023	PowhegPythia8EvtGen_CT10_AZNLOCTEQ6L1_VBF400NWA_WWlvlv	$1.07 \cdot 10^{-4}$	1.00	0.598
341024	PowhegPythia8EvtGen_CT10_AZNLOCTEQ6L1_VBF500NWA_WWlvlv	$1.07 \cdot 10^{-4}$	1.00	0.604
341025	PowhegPythia8EvtGen_CT10_AZNLOCTEQ6L1_VBF600NWA_WWlvlv	$1.07 \cdot 10^{-4}$	1.00	0.604
341026	PowhegPythia8EvtGen_CT10_AZNLOCTEQ6L1_VBF700NWA_WWlvlv	$1.07 \cdot 10^{-4}$	1.00	0.608
343466	PowhegPythia8EvtGen_CT10_AZNLOCTEQ6L1_VBF750NWA_WWlvlv	$1.07 \cdot 10^{-4}$	1.00	0.606
341027	PowhegPythia8EvtGen_CT10_AZNLOCTEQ6L1_VBF800NWA_WWlvlv	$1.07 \cdot 10^{-4}$	1.00	0.614
341028	PowhegPythia8EvtGen_CT10_AZNLOCTEQ6L1_VBF900NWA_WWlvlv	$1.07 \cdot 10^{-4}$	1.00	0.615
341029	PowhegPythia8EvtGen_CT10_AZNLOCTEQ6L1_VBF1000NWA_WWlvlv	$1.07 \cdot 10^{-4}$	1.00	0.616
343368	PowhegPythia8EvtGen_CT10_AZNLOCTEQ6L1_VBF1200NWA_WWlvlv	$1.07 \cdot 10^{-4}$	1.00	0.615
341030	PowhegPythia8EvtGen_CT10_AZNLOCTEQ6L1_VBF1400NWA_WWlvlv	$1.07 \cdot 10^{-4}$	1.00	0.614
343369	PowhegPythia8EvtGen_CT10_AZNLOCTEQ6L1_VBF1600NWA_WWlvlv	$1.07 \cdot 10^{-4}$	1.00	0.617
341031	PowhegPythia8EvtGen_CT10_AZNLOCTEQ6L1_VBF1800NWA_WWlvlv	$1.07 \cdot 10^{-4}$	1.00	0.619
343370	PowhegPythia8EvtGen_CT10_AZNLOCTEQ6L1_VBF2000NWA_WWlvlv	$1.07 \cdot 10^{-4}$	1.00	0.616
341032	PowhegPythia8EvtGen_CT10_AZNLOCTEQ6L1_VBF2200NWA_WWlvlv	$1.07 \cdot 10^{-4}$	1.00	0.619
343371	PowhegPythia8EvtGen_CT10_AZNLOCTEQ6L1_VBF2400NWA_WWlvlv	$1.07 \cdot 10^{-4}$	1.00	0.615
341033	PowhegPythia8EvtGen_CT10_AZNLOCTEQ6L1_VBF2600NWA_WWlvlv	$1.07 \cdot 10^{-4}$	1.00	0.619
343372	PowhegPythia8EvtGen_CT10_AZNLOCTEQ6L1_VBF2800NWA_WWlvlv	$1.07 \cdot 10^{-4}$	1.00	0.619
341034	PowhegPythia8EvtGen_CT10_AZNLOCTEQ6L1_VBF3000NWA_WWlvlv	$1.07 \cdot 10^{-4}$	1.00	0.622

Table B.1: Nominal MC simulated datasets.

ID	Name	σ_{MC}/nb	k-factor	$\epsilon_{\mathrm{FILTER}}$
343485	aMcAtNloPythia8EvtGen_A14NNPDF23LO_H15lpluslminus400w15	$1.07 \cdot 10^{-4}$	1.00	1.00
343486	aMcAtNloPythia8EvtGen_A14NNPDF23LO_H15lpluslminus600w15	$1.07 \cdot 10^{-4}$	1.00	1.00
343487	aMcAtNloPythia8EvtGen_A14NNPDF23LO_H15lpluslminus750w15	$1.07 \cdot 10^{-4}$	1.00	1.00
343488	aMcAtNloPythia8EvtGen_A14NNPDF23LO_H15lpluslminus800w15	$1.07 \cdot 10^{-4}$	1.00	1.00
343489	aMcAtNloPythia8EvtGen_A14NNPDF23LO_H15lpluslminus1000w15	$1.07 \cdot 10^{-4}$	1.00	1.00
343490	aMcAtNloPythia8EvtGen_A14NNPDF23LO_H15lpluslminus1200w15	$1.07 \cdot 10^{-4}$	1.00	1.00
343491	aMcAtNloPythia8EvtGen_A14NNPDF23LO_H15lpluslminus1400w15	$1.07 \cdot 10^{-4}$	1.00	1.00
343492	aMcAtNloPythia8EvtGen_A14NNPDF23LO_H15lpluslminus1600w15	$1.07 \cdot 10^{-4}$	1.00	1.00
343493	aMcAtNloPythia8EvtGen_A14NNPDF23LO_H15lpluslminus1800w15	$1.07 \cdot 10^{-4}$	1.00	1.00
343494	aMcAtNloPythia8EvtGen_A14NNPDF23LO_H15lpluslminus2000w15	$1.07 \cdot 10^{-4}$	1.00	1.00
343495	aMcAtNloPythia8EvtGen_A14NNPDF23LO_H15lpluslminus2200w15	$1.07 \cdot 10^{-4}$	1.00	1.00
343496	aMcAtNloPythia8EvtGen_A14NNPDF23LO_H15lpluslminus2400w15	$1.07 \cdot 10^{-4}$	1.00	1.00
343497	aMcAtNloPythia8EvtGen_A14NNPDF23LO_H15lpluslminus2600w15	$1.07 \cdot 10^{-4}$	1.00	1.00
343498	aMcAtNloPythia8EvtGen_A14NNPDF23LO_H15lpluslminus2800w15	$1.07 \cdot 10^{-4}$	1.00	1.00
343499	aMcAtNloPythia8EvtGen_A14NNPDF23LO_H15lpluslminus3000w15	$1.07 \cdot 10^{-4}$	1.00	1.00
341080	PowhegPythia8EvtGen_CT10_AZNLOCTEQ6L1_VBFH125_WWlvlv	$8.58 \cdot 10^{-05}$	1.00	0.510
361063	Sherpa_CT10_llll	$1.26 \cdot 10^{-02}$	0.910	1.00
361064	Sherpa_CT10_lllvSFMinus	$1.85 \cdot 10^{-03}$	0.910	1.00
361065	Sherpa_CT10_lllvOFMinus	$3.62 \cdot 10^{-03}$	0.910	1.00
361066	Sherpa_CT10_lllvSFPlus	$2.57 \cdot 10^{-03}$	0.910	1.00
361067	Sherpa_CT10_lllvOFPlus	$5.02 \cdot 10^{-03}$	0.910	1.00
361068	Sherpa_CT10_llvv	$1.40 \cdot 10^{-02}$	0.910	1.00
361070	Sherpa_CT10_llvvjj_ss_EW6	$4.34 \cdot 10^{-05}$	0.910	1.00
361071	Sherpa_CT10_lllvjj_EW6	$4.20 \cdot 10^{-05}$	0.910	1.00
361072	Sherpa_CT10_llljj_EW6	$3.15 \cdot 10^{-05}$	0.910	1.00
361073	Sherpa_CT10_gllll	$2.09 \cdot 10^{-05}$	1.55	1.00
361077	Sherpa_CT10_ggllvv	$8.55 \cdot 10^{-04}$	1.55	1.00
361091	Sherpa_CT10_WplvWmqq_SHv21_improved	$2.49 \cdot 10^{-02}$	0.910	1.00
361092	Sherpa_CT10_WpqqWmlv_SHv21_improved	$2.49 \cdot 10^{-02}$	0.910	1.00
361093	Sherpa_CT10_WlvZqq_SHv21_improved	$1.15 \cdot 10^{-02}$	0.910	1.00
361094	Sherpa_CT10_WqqZll_SHv21_improved	$3.42 \cdot 10^{-03}$	0.910	1.00
361095	Sherpa_CT10_WqqZvv_SHv21_improved	$6.78 \cdot 10^{-03}$	0.910	1.00
361096	Sherpa_CT10_ZqqZll_SHv21_improved	$1.65 \cdot 10^{-02}$	0.910	0.143
361097	Sherpa_CT10_ZqqZvv_SHv21_improved	$1.64 \cdot 10^{-02}$	0.910	0.282
410015	PowhegPythiaEvtGen_P2012_Wt_dilepton_top	$3.58 \cdot 10^{-03}$	1.05	1.00
410016	PowhegPythiaEvtGen_P2012_Wt_dilepton_antitop	$3.58 \cdot 10^{-03}$	1.05	1.00
410009	PowhegPythiaEvtGen_P2012_ttbar_hdamp172p5_dil	$6.96 \cdot 10^{-01}$	1.20	0.105
361500	MadGraphPythia8EvtGen_A14NNPDF23LO_Zee_Np0	1.40	1.23	1.00
361501	MadGraphPythia8EvtGen_A14NNPDF23LO_Zee_Np1	$2.12 \cdot 10^{-01}$	1.23	1.00
361502	MadGraphPythia8EvtGen_A14NNPDF23LO_Zee_Np2	$6.73 \cdot 10^{-02}$	1.23	1.00
361503	MadGraphPythia8EvtGen_A14NNPDF23LO_Zee_Np3	$1.87 \cdot 10^{-02}$	1.23	1.00
361504	MadGraphPythia8EvtGen_A14NNPDF23LO_Zee_Np4	$7.29 \cdot 10^{-03}$	1.23	1.00
363123	MGPy8EG_N30NLO_Zmumu_Ht0_70_CVetoBVeto	1.71	1.14	0.832
363124	MGPy8EG_N30NLO_Zmumu_Ht0_70_CFilterBVeto	1.72	1.14	0.108
363125	MGPy8EG_N30NLO_Zmumu_Ht0_70_BFilter	1.72	1.14	0.0592
363126	MGPy8EG_N30NLO_Zmumu_Ht70_140_CVetoBVeto	$8.45 \cdot 10^{-02}$	1.14	0.718
363127	MGPy8EG_N30NLO_Zmumu_Ht70_140_CFilterBVeto	$8.45 \cdot 10^{-02}$	1.14	0.174
363128	MGPy8EG_N30NLO_Zmumu_Ht70_140_BFilter	$8.48 \cdot 10^{-02}$	1.14	0.108
363129	MGPy8EG_N30NLO_Zmumu_Ht140_280_CVetoBVeto	$3.57 \cdot 10^{-02}$	1.14	0.676
363130	MGPy8EG_N30NLO_Zmumu_Ht140_280_CFilterBVeto	$3.59 \cdot 10^{-02}$	1.14	0.200
363131	MGPy8EG_N30NLO_Zmumu_Ht140_280_BFilter	$3.58 \cdot 10^{-02}$	1.14	0.127
363132	MGPy8EG_N30NLO_Zmumu_Ht280_500_CVetoBVeto	$8.17 \cdot 10^{-03}$	1.14	0.627
363133	MGPy8EG_N30NLO_Zmumu_Ht280_500_CFilterBVeto	$8.21 \cdot 10^{-03}$	1.14	0.226
363134	MGPy8EG_N30NLO_Zmumu_Ht280_500_BFilter	$8.17 \cdot 10^{-03}$	1.14	0.143
363135	MGPy8EG_N30NLO_Zmumu_Ht500_700_CVetoBVeto	$1.25 \cdot 10^{-03}$	1.14	0.596
363136	MGPy8EG_N30NLO_Zmumu_Ht500_700_CFilterBVeto	$1.26 \cdot 10^{-03}$	1.14	0.256
363137	MGPy8EG_N30NLO_Zmumu_Ht500_700_BFilter	$1.28 \cdot 10^{-03}$	1.14	0.152
363138	MGPy8EG_N30NLO_Zmumu_Ht700_1000_CVetoBVeto	$4.36 \cdot 10^{-04}$	1.14	0.571
363139	MGPy8EG_N30NLO_Zmumu_Ht700_1000_CFilterBVeto	$4.46 \cdot 10^{-04}$	1.14	0.260
363140	MGPy8EG_N30NLO_Zmumu_Ht700_1000_BFilter	$4.46 \cdot 10^{-04}$	1.14	0.160
363141	MGPy8EG_N30NLO_Zmumu_Ht1000_2000_CVetoBVeto	$1.49 \cdot 10^{-04}$	1.14	0.549
363142	MGPy8EG_N30NLO_Zmumu_Ht1000_2000_CFilterBVeto	$1.46 \cdot 10^{-04}$	1.14	0.272
363143	MGPy8EG_N30NLO_Zmumu_Ht1000_2000_BFilter	$1.47 \cdot 10^{-04}$	1.14	0.173
363144	MGPy8EG_N30NLO_Zmumu_Ht2000_E_CMS_CVetoBVeto	$5.54 \cdot 10^{-06}$	1.14	0.563
363145	MGPy8EG_N30NLO_Zmumu_Ht2000_E_CMS_CFilterBVeto	$5.55 \cdot 10^{-06}$	1.14	0.293
363146	MGPy8EG_N30NLO_Zmumu_Ht2000_E_CMS_BFilter	$5.64 \cdot 10^{-06}$	1.14	0.163

Table B.2: Nominal MC simulated datasets.

ID	Name	σ_{MC}/nb	k-factor	$\epsilon_{\mathrm{FILTER}}$
361510	MadGraphPythia8EvtGen_A14NNPDF23LO_Ztautau_Np0	1.40	1.23	1.00
361511	MadGraphPythia8EvtGen_A14NNPDF23LO_Ztautau_Np1	$2.11 \cdot 10^{-01}$	1.23	1.00
361512	MadGraphPythia8EvtGen_A14NNPDF23LO_Ztautau_Np2	$6.72 \cdot 10^{-02}$	1.23	1.00
361513	MadGraphPythia8EvtGen_A14NNPDF23LO_Ztautau_Np3	$1.86 \cdot 10^{-02}$	1.23	1.00
361514	MadGraphPythia8EvtGen_A14NNPDF23LO_Ztautau_Np4	$7.28 \cdot 10^{-03}$	1.23	1.00
361628	MadGraphPythia8EvtGen_A14NNPDF23LO_Zee_lowMll_Np0	2.68	1.23	1.00
361629	MadGraphPythia8EvtGen_A14NNPDF23LO_Zee_lowMll_Np1	$4.50 \cdot 10^{-02}$	1.23	1.00
361630	MadGraphPythia8EvtGen_A14NNPDF23LO_Zee_lowMll_Np2	$2.93 \cdot 10^{-02}$	1.23	1.00
361631	MadGraphPythia8EvtGen_A14NNPDF23LO_Zee_lowMll_Np3	$6.12 \cdot 10^{-03}$	1.23	1.00
361632	MadGraphPythia8EvtGen_A14NNPDF23LO_Zee_lowMll_Np4	$2.21 \cdot 10^{-03}$	1.23	1.00
363725	MGPy8EG_N30NLO_Zmumu_lowMll_Ht0_70_CVetoBVeto	2.81	1.14	0.888
363726	MGPy8EG_N30NLO_Zmumu_lowMll_Ht0_70_CFilterBVeto	2.82	1.14	0.0846
363727	MGPy8EG_N30NLO_Zmumu_lowMll_Ht0_70_BFilter	2.82	1.14	0.0273
363728	MGPy8EG_N30NLO_Zmumu_lowMll_Ht70_140_CVetoBVeto	$2.59 \cdot 10^{-02}$	1.14	0.667
363729	MGPy8EG_N30NLO_Zmumu_lowMll_Ht70_140_CFilterBVeto	$2.59 \cdot 10^{-02}$	1.14	0.252
363730	MGPy8EG_N30NLO_Zmumu_lowMll_Ht70_140_BFilter	$2.59 \cdot 10^{-02}$	1.14	0.0807
363731	MGPy8EG_N30NLO_Zmumu_lowMll_Ht140_280_CVetoBVeto	$9.26 \cdot 10^{-03}$	1.14	0.635
363732	MGPy8EG_N30NLO_Zmumu_lowMll_Ht140_280_CFilterBVeto	$9.28 \cdot 10^{-03}$	1.14	0.267
363733	MGPy8EG_N30NLO_Zmumu_lowMll_Ht140_280_BFilter	$9.32 \cdot 10^{-03}$	1.14	0.100
363734	MGPy8EG_N30NLO_Zmumu_lowMll_Ht280_500_CVetoBVeto	$1.83 \cdot 10^{-03}$	1.14	0.596
363735	MGPy8EG_N30NLO_Zmumu_lowMll_Ht280_500_CFilterBVeto	$1.84 \cdot 10^{-03}$	1.14	0.279
363736	MGPy8EG_N30NLO_Zmumu_lowMll_Ht280_500_BFilter	$1.84 \cdot 10^{-03}$	1.14	0.123
363737	MGPy8EG_N30NLO_Zmumu_lowMll_Ht500_700_CVetoBVeto	$2.43 \cdot 10^{-04}$	1.14	0.574
363738	MGPy8EG_N30NLO_Zmumu_lowMll_Ht500_700_CFilterBVeto	$2.44 \cdot 10^{-04}$	1.14	0.293
363739	MGPy8EG_N30NLO_Zmumu_lowMll_Ht500_700_BFilter	$2.44 \cdot 10^{-04}$	1.14	0.139
363740	MGPy8EG_N30NLO_Zmumu_lowMll_Ht700_1000_CVetoBVeto	$7.51 \cdot 10^{-05}$	1.14	0.551
363741	MGPy8EG_N30NLO_Zmumu_lowMll_Ht700_1000_CFilterBVeto	$7.41 \cdot 10^{-05}$	1.14	0.295
363742	MGPy8EG_N30NLO_Zmumu_lowMll_Ht700_1000_BFilter	$7.41 \cdot 10^{-05}$	1.14	0.149
363743	MGPy8EG_N30NLO_Zmumu_lowMll_Ht1000_2000_CVetoBVeto	$2.02 \cdot 10^{-05}$	1.14	0.543
363744	MGPy8EG_N30NLO_Zmumu_lowMll_Ht1000_2000_CFilterBVeto	$2.00 \cdot 10^{-05}$	1.14	0.298
363745	MGPy8EG_N30NLO_Zmumu_lowMll_Ht1000_2000_BFilter	$2.01 \cdot 10^{-05}$	1.14	0.157
363746	MGPy8EG_N30NLO_Zmumu_lowMll_Ht2000_E_CMS_CVetoBVeto	$3.56 \cdot 10^{-07}$	1.14	0.510
363747	MGPy8EG_N30NLO_Zmumu_lowMll_Ht2000_E_CMS_CFilterBVeto	$3.61 \cdot 10^{-07}$	1.14	0.304
363748	MGPy8EG_N30NLO_Zmumu_lowMll_Ht2000_E_CMS_BFilter	$3.81 \cdot 10^{-07}$	1.14	0.172
361638	MadGraphPythia8EvtGen_A14NNPDF23LO_Ztautau_lowMll_Np0	2.41	1.23	1.00
361639	MadGraphPythia8EvtGen_A14NNPDF23LO_Ztautau_lowMll_Np1	$4.60 \cdot 10^{-02}$	1.23	1.00
361640	MadGraphPythia8EvtGen_A14NNPDF23LO_Ztautau_lowMll_Np2	$2.89 \cdot 10^{-02}$	1.23	1.00
361641	MadGraphPythia8EvtGen_A14NNPDF23LO_Ztautau_lowMll_Np3	$6.05 \cdot 10^{-03}$	1.23	1.00
361642	MadGraphPythia8EvtGen_A14NNPDF23LO_Ztautau_lowMll_Np4	$2.21 \cdot 10^{-03}$	1.23	1.00
301535	Sherpa_CT10_eegammaPt10_35	$5.27 \cdot 10^{-02}$	1.00	1.00
301536	Sherpa_CT10_mumugammaPt10_35	$5.27 \cdot 10^{-02}$	1.00	1.00
304776	Sherpa_CT10_tautaugammaPt10_35	$5.27 \cdot 10^{-02}$	1.00	1.00
301887	Sherpa_CT10_enugammaPt10_35	$2.01 \cdot 10^{-01}$	1.00	1.00
301888	Sherpa_CT10_munugammaPt10_35	$2.01 \cdot 10^{-01}$	1.00	1.00
301889	Sherpa_CT10_taunugammaPt10_35	$2.01 \cdot 10^{-01}$	1.00	1.00
301890	Sherpa_CT10_enugammaPt35_70	$1.54 \cdot 10^{-02}$	1.00	1.00
301891	Sherpa_CT10_enugammaPt70_140	$1.53 \cdot 10^{-03}$	1.00	1.00
301892	Sherpa_CT10_enugammaPt140	$2.42 \cdot 10^{-04}$	1.00	1.00
301893	Sherpa_CT10_munugammaPt35_70	$1.53 \cdot 10^{-02}$	1.00	1.00
301894	Sherpa_CT10_munugammaPt70_140	$1.52 \cdot 10^{-03}$	1.00	1.00
301895	Sherpa_CT10_munugammaPt140	$2.42 \cdot 10^{-04}$	1.00	1.00
301896	Sherpa_CT10_taunugammaPt35_70	$1.53 \cdot 10^{-02}$	1.00	1.00
301897	Sherpa_CT10_taunugammaPt70_140	$1.53 \cdot 10^{-03}$	1.00	1.00
301898	Sherpa_CT10_taunugammaPt140	$2.43 \cdot 10^{-04}$	1.00	1.00
301899	Sherpa_CT10_eegammaPt35_70	$5.24 \cdot 10^{-03}$	1.00	1.00
301900	Sherpa_CT10_eegammaPt70_140	$3.85 \cdot 10^{-04}$	1.00	1.00
301901	Sherpa_CT10_eegammaPt140	$4.72 \cdot 10^{-05}$	1.00	1.00
301902	Sherpa_CT10_mumugammaPt35_70	$5.25 \cdot 10^{-03}$	1.00	1.00
301903	Sherpa_CT10_mumugammaPt70_140	$3.86 \cdot 10^{-04}$	1.00	1.00
301904	Sherpa_CT10_mumugammaPt140	$4.72 \cdot 10^{-05}$	1.00	1.00
301905	Sherpa_CT10_tautaugammaPt35_70	$5.25 \cdot 10^{-03}$	1.00	1.00
301906	Sherpa_CT10_tautaugammaPt70_140	$3.85 \cdot 10^{-04}$	1.00	1.00
301907	Sherpa_CT10_tautaugammaPt140	$4.70 \cdot 10^{-05}$	1.00	1.00

Table B.3: Nominal MC simulated datasets.

ID	Name	σ_{MC}/nb	k-factor	$\epsilon_{\mathrm{FILTER}}$
363072	Sherpa_CT10_llvv_fac4	$1.40 \cdot 10^{-2}$	0.910	1.00
363073	Sherpa_CT10_llvv_fac025	$1.41 \cdot 10^{-2}$	0.910	1.00
363074	Sherpa_CT10_llvv_renorm4	$1.35 \cdot 10^{-2}$	0.910	1.00
363075	Sherpa_CT10_llvv_renorm025	$1.44 \cdot 10^{-2}$	0.910	1.00
363076	Sherpa_CT10_llvv_qsf4	$1.39 \cdot 10^{-2}$	0.910	1.00
363077	Sherpa_CT10_llvv_qsf025	$1.44 \cdot 10^{-2}$	0.910	1.00
363084	Sherpa_CT10_ggllvv_fac4	$8.75 \cdot 10^{-4}$	1.55	1.00
363085	Sherpa_CT10_ggllvv_fac025	$8.20 \cdot 10^{-4}$	1.55	1.00
363086	Sherpa_CT10_ggllvv_renorm4	$6.55 \cdot 10^{-4}$	1.55	1.00
363087	Sherpa_CT10_ggllvv_renorm025	$1.16 \cdot 10^{-3}$	1.55	1.00
363088	Sherpa_CT10_ggllvv_qsf4	$6.90 \cdot 10^{-4}$	1.55	1.00
363089	Sherpa_CT10_ggllvv_qsf025	$1.13 \cdot 10^{-3}$	1.55	1.00
363299	Sherpa_CT10_llvv_ckkw15	$1.42 \cdot 10^{-2}$	0.910	1.00
363300	Sherpa_CT10_llvv_ckkw30	$1.38 \cdot 10^{-2}$	0.910	1.00
361591	PhHppEG_AU2CT10_WlnuWlnu	$1.06 \cdot 10^{-2}$	1.00	1.00
410001	PowhegPythiaEvtGen_P2012radHi_ttbar_hdamp345_down_nonallhad	$7.84 \cdot 10^{-1}$	1.06	0.543
410002	PowhegPythiaEvtGen_P2012radLo_ttbar_hdamp172_up_nonallhad	$6.11 \cdot 10^{-1}$	1.36	0.543
410003	aMcAtNloHerwigppEvtGen_ttbar_nonallhad	$6.95 \cdot 10^{-1}$	1.20	0.543
410004	PowhegHerwigppEvtGen_UEEE5_ttbar_hdamp172p5_nonallhad	$6.96 \cdot 10^{-1}$	1.19	0.544
410145	PowhegHerwigppEvtGen_UEEE5_Wt_dilepton_top	$4.00 \cdot 10^{-3}$	0.968	1.00
410146	PowhegHerwigppEvtGen_UEEE5_Wt_dilepton_antitop	$4.00 \cdot 10^{-3}$	0.968	1.00
410064	PowhegPythiaEvtGen_P2012_Wt_DS_dilepton_top	$3.41 \cdot 10^{-3}$	1.05	1.00
410065	PowhegPythiaEvtGen_P2012_Wt_DS_dilepton_antitop	$3.41 \cdot 10^{-3}$	1.05	1.00
410103	PowhegPythiaEvtGen_P2012radHi_Wt_dilepton_top	$3.68 \cdot 10^{-3}$	1.03	1.00
410104	PowhegPythiaEvtGen_P2012radLo_Wt_dilepton_top	$3.52 \cdot 10^{-3}$	1.07	1.00
410105	PowhegPythiaEvtGen_P2012radHi_Wt_dilepton_antitop	$3.68 \cdot 10^{-3}$	1.03	1.00
410106	PowhegPythiaEvtGen_P2012radLo_Wt_dilepton_antitop	$3.52 \cdot 10^{-3}$	1.07	1.00

Table B.4: MC simulated datasets used for the systematic uncertainty evaluation.

Bibliography

[1] The ATLAS and CMS collaborations. Measurements of the Higgs boson production and decay rates and constraints on its couplings from a combined ATLAS and CMS analysis of the LHC pp collision data at $\sqrt{s} = 7$ and 8 TeV. *JHEP*, 08:045, 2016.

[2] The ATLAS and CMS collaborations. Combined Measurement of the Higgs Boson Mass in *pp* Collisions at $\sqrt{s} = 7$ and 8 TeV with the ATLAS and CMS Experiments. *Phys. Rev. Lett.*, 114:191803, 2015.

[3] The ATLAS collaboration. Study of the spin and parity of the Higgs boson in diboson decays with the ATLAS detector. *Eur. Phys. J.*, C75(10):476, 2015. [Erratum: Eur. Phys. J.C76,no.3,152(2016)].

[4] The CMS collaboration. Constraints on the spin-parity and anomalous HVV couplings of the Higgs boson in proton collisions at 7 and 8 TeV. *Phys. Rev.*, D92(1):012004, 2015.

[5] A. Hill and J. J. van der Bij. STRONGLY INTERACTING SINGLET - DOUBLET HIGGS MODEL. *Phys. Rev.*, D36:3463–3473, 1987.

[6] G. C. Branco, P. M. Ferreira, L. Lavoura, M. N. Rebelo, Marc Sher, and Joao P. Silva. Theory and phenomenology of two-Higgs-doublet models. *Phys. Rept.*, 516:1–102, 2012.

[7] The ATLAS collaboration. Constraints on new phenomena via Higgs boson couplings and invisible decays with the ATLAS detector. *JHEP*, 11:206, 2015.

[8] The ATLAS collaboration. Search for a high-mass Higgs boson decaying to a W boson pair in *pp* collisions at $\sqrt{s} = 8$ TeV with the ATLAS detector. *JHEP*, 01:032, 2016.

[9] The CMS collaboration. Search for a Higgs boson in the mass range from 145 to 1000 GeV decaying to a pair of W or Z bosons. *JHEP*, 10:144, 2015.

[10] Griffiths, David. *Introduction to Elementary Particles*. WILEY-VCH, 2nd edition, 2008.

[11] Bleck-Neuhaus, Joern. *Elementare Teilchen - Moderne Physik Von Den Atomen Bis Zum Standard-Modell*. Springer DE, 2010.

[12] The ATLAS collaboration. Observation of a new particle in the search for the Standard Model Higgs boson with the ATLAS detector at the LHC. *Phys. Lett.*, B716:1–29, 2012.

[13] The CMS collaboration. Observation of a new boson at a mass of 125 GeV with the CMS experiment at the LHC. *Phys. Lett.*, B716:30–61, 2012.

[14] MissMJ, via Wikimedia Commons. Standard Model of Elementary Particles. https://commons.wikimedia.org/wiki/File:Standard_Model_of_Elementary_Particles.svg. [Online; accessed 04-November-2016].

[15] Halzen, Francis and Martin, Alan D. *QUARK & LEPTONS: An Introductory Course in Modern Particle Physics*. John Wiley & Sons, 1984.

[16] Chris Quigg. Unanswered Questions in the Electroweak Theory. *Ann. Rev. Nucl. Part. Sci.*, 59:505–555, 2009.

[17] B. Povh, K. Rith, C. Scholz, F. Zetsche, and W. Rodejohann. *Teilchen und Kerne: Eine Einfuehrung in die physikalischen Konzepte*. Springer DE, 2014.

[18] Abdelhak Djouadi. The Anatomy of electro-weak symmetry breaking. I: The Higgs boson in the standard model. *Phys. Rept.*, 457:1–216, 2008.

[19] Gerard 't Hooft. Renormalizable Lagrangians for Massive Yang-Mills Fields. *Nucl. Phys.*, B35:167–188, 1971.

[20] Gerard 't Hooft and M. J. G. Veltman. Regularization and Renormalization of Gauge Fields. *Nucl. Phys.*, B44:189–213, 1972.

[21] F. Englert and R. Brout. Broken Symmetry and the Mass of Gauge Vector Mesons. *Phys. Rev. Lett.*, 13:321–323, 1964.

[22] Peter W. Higgs. Broken Symmetries and the Masses of Gauge Bosons. *Phys. Rev. Lett.*, 13:508–509, 1964.

[23] Peter Schmueser. *Feynman-Graphen und Eichtheorien fuer Experimentalphysiker*. Springer Berlin Heidelberg, 1988.

[24] David J. Summers. Mini - jets as a perturbative probe of color charge. In *QCD and high energy hadronic interactions. Proceedings, 32nd Rencontres de Moriond, Les Arcs, France, March 22-29, 1997*, pages 223–228, 1997.

[25] Lyndon Evans and Philip Bryant. LHC Machine. *Journal of Instrumentation*, 3(08):S08001, 2008.

[26] C Lefevre. LHC: the guide (English version). Guide du LHC (version anglaise). Feb 2009.

[27] The ATLAS collaboration. The ATLAS Experiment at the CERN Large Hadron Collider. *JINST*, 3:S08003, 2008.

[28] Joao Pequenao. Computer generated image of the whole ATLAS detector. Mar 2008.

[29] F. Pastore on behalf of the ATLAS collaboration. ATLAS Run-2 status and performance. *Nucl. Part. Phys. Proc.*, 270-272:3–7, 2016.

[30] Joao Pequenao. Computer generated image of the ATLAS inner detector. Mar 2008.

[31] M Capeans, G Darbo, K Einsweiller, M Elsing, T Flick, M Garcia-Sciveres, C Gemme, H Pernegger, O Rohne, and R Vuillermet. ATLAS Insertable B-Layer Technical Design Report. Technical Report CERN-LHCC-2010-013. ATLAS-TDR-19, Sep 2010.

[32] Giulia Ripellino on behalf of the ATLAS collaboration. The alignment of the ATLAS Inner Detector in Run 2. Technical Report ATL-INDET-PROC-2016-003, CERN, Geneva, Sep 2016.

[33] Joao Pequenao. Computer Generated image of the ATLAS calorimeter. Mar 2008.

[34] Joao Pequenao. Computer generated image of the ATLAS Muons subsystem. Mar 2008.

[35] Yu Nakahama on behalf of the ATLAS Collaboration. The ATLAS Trigger System: Ready for Run-2. *J. Phys. Conf. Ser.*, 664(8):082037, 2015.

[36] T. Cornelissen, M. Elsing, S. Fleischmann, W. Liebig, and E. Moyse. Concepts, Design and Implementation of the ATLAS New Tracking (NEWT). 2007.

[37] The ATLAS collaboration. Performance of the ATLAS Inner Detector Track and Vertex Reconstruction in the High Pile-Up LHC Environment. (ATLAS-CONF-2012-042), 2012.

[38] The ATLAS collaboration. *Expected performance of the ATLAS experiment: detector, trigger and physics*. CERN, Geneva, 2009.

[39] The ATLAS collaboration. Muon reconstruction performance of the ATLAS detector in proton-proton collision data at $\sqrt{s}$ =13 TeV. *Eur. Phys. J.*, C76(5):292, 2016.

[40] The ATLAS collaboration. Performance of primary vertex reconstruction in proton-proton collisions at $\sqrt{s}$ =7 TeV in the ATLAS experiment. (ATLAS-CONF-2010-069), 2010.

[41] Andy Buckley et al. General-purpose event generators for LHC physics. *Phys. Rept.*, 504:145–233, 2011.

[42] The ATLAS collaboration. Electron efficiency measurements with the ATLAS detector using the 2015 LHC proton-proton collision data. (ATLAS-CONF-2016-024), 2016.

[43] The ATLAS collaboration. Electron and photon energy calibration with the ATLAS detector using data collected in 2015 at $\sqrt{s} = 13$ TeV. (ATL-PHYS-PUB-2016-015), Aug 2016.

[44] W. Lampl, S. Laplace, D. Lelas, P. Loch, H. Ma, S. Menke, S. Rajagopalan, D. Rousseau, S. Snyder, and G. Unal. Calorimeter clustering algorithms: Description and performance. (ATL-LARG-PUB-2008-002), 2008.

[45] Matteo Cacciari, Gavin P. Salam, and Gregory Soyez. The anti-k_t jet clustering algorithm. *Journal of High Energy Physics*, 2008(04):063, 2008.

[46] The ATLAS collaboration. Jet energy scale and its systematic uncertainty in proton-proton collisions at sqrt(s)=7 TeV with ATLAS 2011 data. (ATLAS-CONF-2013-004), 2013.

[47] The ATLAS collaboration. Jet Calibration and Systematic Uncertainties for Jets Reconstructed in the ATLAS Detector at $\sqrt{s} = 13$ TeV. (ATL-PHYS-PUB-2015-015), Jul 2015.

[48] Matteo Cacciari, Gavin P. Salam, Gregory Soyez. The catchment area of jets. *Journal of High Energy Physics*, 2008(04):005, 2008.

[49] The ATLAS collaboration. Optimisation of the ATLAS b-tagging performance for the 2016 LHC Run. (ATL-PHYS-PUB-2016-012), Jun 2016.

[50] The ATLAS collaboration. Performance of missing transverse momentum reconstruction for the ATLAS detector in the first proton-proton collisions at at $\sqrt{s}$= 13 TeV. (ATL-PHYS-PUB-2015-027), Jul 2015.

[51] The ATLAS collaboration. Expected performance of missing transverse momentum reconstruction for the ATLAS detector at $\sqrt{s} = 13$ TeV. (ATL-PHYS-PUB-2015-023), Jul 2015.

[52] The ATLAS collaboration. The ATLAS Simulation Infrastructure. *Eur. Phys. J.*, C70:823–874, 2010.

[53] A. D. Martin, W. J. Stirling, R. S. Thorne, and G. Watt. Parton distributions for the LHC. *Eur. Phys. J.*, C63:189–285, 2009.

[54] S. Agostinelli et al. GEANT4: A Simulation toolkit. *Nucl. Instrum. Meth.*, A506:250–303, 2003.

[55] The ATLAS collaboration. *ATLAS Computing: technical design report.* Technical Design Report ATLAS. CERN, Geneva, 2005.

[56] I Bird, P Buncic, F Carminati, M Cattaneo, P Clarke, I Fisk, M Girone, J Harvey, B Kersevan, P Mato, R Mount, and B Panzer-Steindel. Update of the Computing Models of the WLCG and the LHC Experiments. Technical Report CERN-LHCC-2014-014. LCG-TDR-002, Apr 2014.

[57] Stefano Frixione and Paolo Nason and Carlo Oleari. Matching NLO QCD computations with parton shower simulations: the POWHEG method. *Journal of High Energy Physics*, 2007(11):070, 2007.

[58] J. Alwall, R. Frederix, S. Frixione, V. Hirschi, F. Maltoni, O. Mattelaer, H. S. Shao, T. Stelzer, P. Torrielli, and M. Zaro. The automated computation of tree-level and next-to-leading order differential cross sections, and their matching to parton shower simulations. *JHEP*, 07:079, 2014.

[59] Johan Alwall, Michel Herquet, Fabio Maltoni, Olivier Mattelaer, and Tim Stelzer. MadGraph 5 : Going Beyond. *JHEP*, 06:128, 2011.

[60] Stefano Frixione and Bryan R. Webber. Matching NLO QCD computations and parton shower simulations. *JHEP*, 06:029, 2002.

[61] T. Gleisberg, S. Hoeche, F. Krauss, M. Schoenherr, S. Schumann, F. Siegert, J. Winter. Event generation with SHERPA 1.1. *Journal of High Energy Physics*, 2009(02):007, 2009.

[62] Torbjoern Sjoestrand, Stephen Mrenna, and Peter Z. Skands. A Brief Introduction to PYTHIA 8.1. *Comput. Phys. Commun.*, 178:852–867, 2008.

[63] Torbjoern Sjoestrand, Stephen Mrenna, Peter Skands. PYTHIA 6.4 physics and manual. *Journal of High Energy Physics*, 2006(05):026, 2006.

[64] M. Bahr et al. Herwig++ Physics and Manual. *Eur. Phys. J.*, C58:639–707, 2008.

[65] Hung-Liang Lai, Marco Guzzi, Joey Huston, Zhao Li, Pavel M. Nadolsky, Jon Pumplin, and C.-P. Yuan. New parton distributions for collider physics. *Phys. Rev.*, D82:074024, 2010.

[66] Stefano Carrazza, Stefano Forte, and Juan Rojo. Parton Distributions and Event Generators. In *Proceedings, 43rd International Symposium on Multiparticle Dynamics (ISMD 13)*, pages 89–96, 2013.

[67] The ATLAS collaboration. Simulation of top quark production for the ATLAS experiment at sqrt(s) = 13 TeV. (ATL-PHYS-PUB-2016-004), Jan 2016.

[68] Peter Zeiler Skands. Tuning Monte Carlo Generators: The Perugia Tunes. *Phys. Rev.*, D82:074018, 2010.

[69] Jonathan Pumplin, Daniel Robert Stump, Joey Huston, Hung-Liang Lai, Pavel Nadolsky, and Wu-Ki Tung. New Generation of Parton Distributions with Uncertainties from Global QCD Analysis. *Journal of High Energy Physics*, 2002(07):012, 2002.

[70] D. J. Lange. The EvtGen particle decay simulation package. *Nucl. Instrum. Meth.*, A462:152–155, 2001.

[71] The ATLAS collaboration. Multi-Boson Simulation for 13 TeV ATLAS Analyses. (ATL-PHYS-PUB-2016-002), Jan 2016.

[72] The ATLAS collaboration. Monte Carlo Generators for the Production of a W or Z/γ^* Boson in Association with Jets at ATLAS in Run 2. (ATL-PHYS-PUB-2016-003), Jan 2016.

[73] The ATLAS collaboration. Luminosity Results for Run-2. https://twiki.cern.ch/twiki/bin/view/AtlasPublic/LuminosityPublicResultsRun2, 2016. [Online; accessed 23-October-2016].

[74] Heather Gray, Simone Pagan Griso. Tracking CP pre-pre-recommendations. https://indico.cern.ch/event/368819/contributions/873665/attachments/733483/1006379/trkCP_Pre-pre-recommendations.pdf, 2015. [Online, internal; accessed 23-October-2016].

[75] The ATLAS collaboration. Electron identification measurements in ATLAS using $\sqrt{s}$ = 13 TeV data with 50 ns bunch spacing. (ATL-PHYS-PUB-2015-041), Sep 2015.

[76] The ATLAS collaboration. Tagging and suppression of pileup jets. (ATLAS-CONF-2014-018), 2014.

[77] Matthew Klein, Francesco Rubbo, Francesca Ungaro. JVT Calibrations. https://indico.cern.ch/event/478075/contributions/1156283/attachments/1225639/1797670/ungaro_160209_JVT.pdf, 2016. [Online, internal; accessed 22-October-2016].

[78] The ATLAS collaboration. Selection of jets produced in 13 TeV proton-proton collisions with the ATLAS detector. (ATLAS-CONF-2015-029), 2015.

[79] Yoshikazu Nagai. b-tagging in ATLAS. https://indico.in2p3.fr/event/6838/session/3/material/slides/0?contribId=1, 2013. [Online; accessed 25-September-2016].

[80] The ATLAS collaboration. Calibration of b-tagging using dileptonic top pair events in a combinatorial likelihood approach with the ATLAS experiment. (ATLAS-CONF-2014-004), 2014.

[81] The ATLAS collaboration. Calibration of the performance of b-tagging for c and light-flavour jets in the 2012 ATLAS data. (ATLAS-CONF-2014-046), 2014.

[82] D Adams, C Anastopoulos, A Andreazza, M Aoki, L Asquith, M Begel, F Bernlochner, U Blumenschein, A Bocci, S Cheatham, W Davey, P-A Delsart, P-O DeViveiros, A Dewhurst, D Duschinger, F Filthaut, P Francavilla, F Garberson, S Head, A Henrichs, A Hoecker, M Kagan, B Kersevan, TJ Khoo, B Lenzi, D Lopez Mateos, B Malaescu, Z Marshall, T Martin, C Meyer, A Morley, W Murray, M zur Nedden, R Nicolaidou, S Pagan Griso, G Pasztor, P Petroff, C Pizio, R Polifka, X Poveda, R Reece, F Ruehr, F Salvatore, R Sandstroem, T Scanlon, D Scheirich, S Schramm, A Schwartzman, K Suruliz, M Sutton, E Thompson, M Tripiana, A Tuna, S Viel, M Vincter, I Vivarelli, M Wielers, A Wildauer, and Z Zinonos. Recommendations of the Physics Objects and Analysis Harmonisation Study Groups 2014. (ATL-PHYS-INT-2014-018), Jul 2014. Internal.

[83] Steve Farrell. Overlap Removal Tools. https://indico.cern.ch/event/539619/contributions/2191033/attachments/1284239/1909241/Farrell_ort_asg.pdf, 2016. [Online, internal; accessed 16-October-2016].

[84] The ATLAS collaboration. 2015 start-up trigger menu and initial performance assessment of the ATLAS trigger using Run-2 data. Technical Report ATL-DAQ-PUB-2016-001, CERN, Geneva, Mar 2016.

[85] William Buttinger. Using Event Weights to account for differences in Instantaneous Luminosity and Trigger Prescale in Monte Carlo and Data. (ATL-COM-SOFT-2015-119), May 2015. Internal.

[86] The ATLAS collaboration. Search for a high-mass Higgs boson decaying to a pair of W bosons in pp collisions at $\sqrt{s}$=13 TeV with the ATLAS detector. (ATLAS-CONF-2016-074), 2016.

[87] Dominik Duda, Pamela Ferrari, Kunlin Han, Karsten Koeneke, João Barreiro Guimarães da Costa, Lianliang Ma, Thomas Maier, Ilya Tsukerman, Weimin Song, Xueyao Zhang, Zhiqing Zhang, Yongke Zhao, and Yingchun Zhu. Search for a high mass Higgs boson decaying to a W boson pair in pp collisions at $\sqrt{s}$=13 TeV with the ATLAS detector. (ATL-COM-PHYS-2016-477), May 2016. Internal.

[88] Private communication with Yongke Zhao, Shandong University/Laboratoire de l'Accélérateur Linéaire.

[89] The ATLAS collaboration. Constraints on the off-shell Higgs boson signal strength in the high-mass ZZ and WW final states with the ATLAS detector. *Eur. Phys. J.*, C75(7):335, 2015.

[90] Kirill Melnikov and Matthew Dowling. Production of two Z-bosons in gluon fusion in the heavy top quark approximation. *Phys. Lett.*, B744:43–47, 2015.

[91] Fabrizio Caola, Kirill Melnikov, Raoul Rntsch, and Lorenzo Tancredi. QCD corrections to W^+W^- production through gluon fusion. *Phys. Lett.*, B754:275–280, 2016.

[92] Marco Bonvini, Fabrizio Caola, Stefano Forte, Kirill Melnikov, and Giovanni Ridolfi. Signal-background interference effects for $gg \to H \to W^+W^-$ beyond leading order. *Phys. Rev.*, D88(3):034032, 2013.

[93] Chong Sheng Li, Hai Tao Li, Ding Yu Shao, and Jian Wang. Soft gluon resummation in the signal-background interference process of $gg(\to h^*) \to ZZ$. *JHEP*, 08:065, 2015.

[94] Benedikt Biedermann, Marina Billoni, Ansgar Denner, Stefan Dittmaier, Lars Hofer, Barbara Jaeger, and Lukas Salfelder. Next-to-leading-order electroweak corrections to $pp \to W^+W^- \to 4$ leptons at the LHC. *JHEP*, 06:065, 2016.

[95] The ATLAS collaboration. Observation and measurement of Higgs boson decays to WW* with the ATLAS detector. *Phys. Rev.*, D92(1):012006, 2015.

[96] Kathrin Becker, Claudia Bertella, Carsten Daniel Burgard, Nguyen Phuong Dang, Olivier Arnaez, Addolorata Farilla, Pamela Ferrari, Ralf Gugel, Ruchi Gupta, Paihsien Jennifer Hsu, Robert Kehoe, Karsten Koeneke, Takashi Kubota, Aaron Liblong, Pere Rados, Per Edvin Sidebo, Weimin Song, Jonas Strandberg, Heberth Torres, Jacobus Van Nieuwkoop, Natalie Wieseotte, Li Zhou, Christian Schmitt, Valerio Dao, Michela Biglietti, Javier Llorente Merino, Karri Folan Di Petrillo, João Barreiro Guimarães da Costa, Alexander Naip Tuna, Michael Strauss, and Yesenia Hernandez Jimenez. Analysis of $H \to WW^* \to \ell\nu\ell\nu$ VBF and WH production modes with data collected with the ATLAS detector at $\sqrt{s} = 13$ TeV in 2015 and 2016. (ATL-COM-PHYS-2016-015), Jan 2016. Internal.

[97] Private communication with Dominik Duda, Institute SAF Nikhef and University of Amsterdam/Nikhef.

[98] Nikolas Kauer and Claire O'Brien. Heavy Higgs signal-background interference in $gg \to VV$ in the Standard Model plus real singlet. *Eur. Phys. J.*, C75:374, 2015.

[99] Alessandro Ballestrero and Ezio Maina. Interference Effects in Higgs production through Vector Boson Fusion in the Standard Model and its Singlet Extension. *JHEP*, 01:045, 2016.

[100] The ATLAS collaboration. Search for a high-mass Higgs boson decaying to a pair of W bosons in pp collisions at sqrt(s)=13 TeV with the ATLAS detector. (ATLAS-CONF-2016-021), 2016.

[101] Nicolas Greiner, Stefan Hoeche, Gionata Luisoni, Marek Schoenherr, Jan-Christopher Winter, and Valery Yundin. Phenomenological analysis of Higgs boson production through gluon fusion in association with jets. *JHEP*, 01:169, 2016.

[102] The ATLAS collaboration. Improved luminosity determination in pp collisions at sqrt(s) = 7 TeV using the ATLAS detector at the LHC. *Eur. Phys. J.*, C73(8):2518, 2013.

[103] The ATLAS collaboration. Luminosity Determination in pp Collisions at sqrt(s) = 8 TeV using the ATLAS Detector at the LHC. *to be published in Eur. Phys. J. C.*

[104] L. A. Harland-Lang, A. D. Martin, P. Motylinski, and R. S. Thorne. Parton distributions in the LHC era: MMHT 2014 PDFs. *Eur. Phys. J.*, C75(5):204, 2015.

[105] Richard D. Ball et al. Parton distributions for the LHC Run II. *JHEP*, 04:040, 2015.

[106] Iain W. Stewart and Frank J. Tackmann. Theory Uncertainties for Higgs and Other Searches Using Jet Bins. *Phys. Rev.*, D85:034011, 2012.

[107] The ATLAS and CMS collaborations. Procedure for the LHC Higgs boson search combination in summer 2011. (ATL-PHYS-PUB-2011-011), Aug 2011.

[108] Private communication with Lianliang Ma, Shandong University.

[109] The ATLAS collaboration. Combined search for the Standard Model Higgs boson in pp collisions at $\sqrt{s} = 7$ TeV with the ATLAS detector. *Phys. Rev.*, D86:032003, 2012.

[110] A L Read. Presentation of search results: the CL_s technique. *Journal of Physics G: Nuclear and Particle Physics*, 28(10):2693, 2002.

[111] Glen Cowan, Kyle Cranmer, Eilam Gross, and Ofer Vitells. Asymptotic formulae for likelihood-based tests of new physics. *Eur. Phys. J.*, C71:1554, 2011. [Erratum: Eur. Phys. J.C73,2501(2013)].

[112] Alexander Belyaev, Giacomo Cacciapaglia, Haiying Cai, Gabriele Ferretti, Thomas Flacke, Alberto Parolini, and Hugo Serodio. Di-boson signatures as Standard Candles for Partial Compositeness. 2016. arXiv:1610.06591.

[113] The ATLAS collaboration. Search for heavy neutral resonances in vector boson fusion in pp collisions at sqrt(s)=13 TeV with the ATLAS detector at the Large Hadron Collider. (ATLAS-CONF-2016-053), 2016.

[114] The ATLAS collaboration. Search for diboson resonance production in the $\ell\nu qq$ final state using pp collisions at $\sqrt{s} = 13$ TeV with the ATLAS detector at the LHC. (ATLAS-CONF-2016-062), 2016.

[115] The CMS collaboration. Search for high mass Higgs to WW with fully leptonic decays using 2015 data. (CMS-PAS-HIG-16-023), 2016.

[116] Duccio Pappadopulo, Andrea Thamm, Riccardo Torre, and Andrea Wulzer. Heavy Vector Triplets: Bridging Theory and Data. *JHEP*, 09:060, 2014.

[117] Kaustubh Agashe, Hooman Davoudiasl, Gilad Perez, and Amarjit Soni. Warped Gravitons at the LHC and Beyond. *Phys. Rev.*, D76:036006, 2007.

Danksagung

Ich bedanke mich bei

- Prof. Dr. Dorothee Schaile für die Möglichkeit ein Promotionsstudium der Physik durchzuführen und diese Dissertation im Gebiet der Teilchenphysik zu erstellen. Des Weiteren bedanke ich mich für die vielen Tipps und Ratschläge über die Jahre und für das Erstellen des Erstgutachtens.

- Prof. Dr. Wolfgang Dünnweber für das Erstellen des Zweitgutachtens.

- Dr. habil. Johannes Elmsheuser und Dr. Günter Duckeck für die Betreuung während meiner Zeit als Doktorand und für das Korrekturlesen meiner Arbeit.

- den aktuellen und einigen ehemaligen Mitgliedern der Higgs Gruppe des Lehrstuhls für die wertvollen Ratschläge, Erfahrungen und Tipps, die Sie jederzeit bereit waren zu teilen: Dr. Bonnie Chow, Dr. Günter Duckeck, Dr. habil. Johannes Elmsheuser, Friedrich Hönig, Dr. Christian Meineck, Dr. habil. Michiel Sanders und Dr. Jonas Will.

- Frau Grimm-Zeidler, für die Organisation des Lehrstuhls und die stets freundliche Beantwortung von administrativen Fragen.

- Nikolai Hartmann, der mich tapfer als Bürokollegen ertragen hat und immer für anregende Diskussionen zur Verfügung stand.

- Michael Adersberger, Jochen Heinrich und Ferdinand Krieter, die immer für eine Partie Dart zu haben waren um meine Gedanken neu zu sortieren.

- Michael Bender, David Handl, Michael Holzbock und Balthasar Schachtner, die insbesondere im letzten halben Jahr regelmäßige Besuche in ihren Büros befürchten mussten aber immer für Diskussionen bereit waren, sei es über Physik oder andere mehr oder weniger arbeitsrelevante Themen.

- Prof. Dr. Otmar Biebel für die sehr aufschlussreichen und hilfreichen Diskussionen über alle möglichen Themengebiete der Physik und darüber hinaus.

- dem Rest des Lehrstuhls und ehemaligen Mitgliedern für die sehr angenehme Arbeitsatmosphäre. Die Nichterwähnung von individuellen Namen ist nicht als ein Fehlen eines prägenden Eindrucks zu verstehen, sondern vielmehr als Unvermögen des Autors in Worte zu fassen, wie jeder Einzelne zum erfolgreichen Abschluss dieser Doktorarbeit beigetragen hat.

- Alexander Arth, Kai Balle, Dominika Boneberg, Fabrizio Finozzi, Marco Häuser, Ralph Müller, Florian Satzger und Björn Sörgel, die mich als Kommilitonen und Freunde durch das Studium begleitet haben.

- meinen Eltern, die mich immer unterstützt und mir die Grundlage gegeben haben ein Studium der Physik durchzuführen und erfolgreich mit einer Doktorarbeit abzuschließen.